PROBING THE LUMINOSITY FUNCTION OF GALAXIES AT THE EPOCH OF REIONIZATION

by

Haojing Yan

A Dissertation Presented in Partial Fulfillment
of the Requirements for the Degree
Doctor of Philosophy

ARIZONA STATE UNIVERSITY

May 2003

PROBING THE LUMINOSITY FUNCTION OF GALAXIES

AT THE EPOCH OF REIONIZATION

by

Haojing Yan

has been approved

May 2003

APPROVED:

, Chair

Supervisory Committee

ACCEPTED:

Department Chair

Dean, Graduate College

ABSTRACT

With the discoveries of a few objects at redshifts (z) higher than 6, the observational boundary of the Universe has been pushed to the epoch when it was was less than 1 Gyr old. There are now growing evidences that the reionization, an important event in the evolutionary history of the Universe, ended at around redshift of 6. To obtain a comprehensive picture of the reionization, the luminosity function (LF) of galaxies at this redshift needs to be accessed. In order to achieve this goal, a large sample of galaxies at round redshift of 6 should first be acquired.

This dissertation presents a study that aims at systematically constraining the luminosity function of galaxies at z=6. The study began with an educated guess about this LF by extropolating from the result at lower redshift, z=3. Based on this first guess, estimates were made to predict the number densities of galaxies at z=6 at different brightness levels. Using this prediction, a wide-field survey was designed to constrain the bright-end of the LF. This survey, covering an area of one square-degree, was carried out at the NOAO 4m telescopes with an innovated set of intermediate-band filters. This bright-end survey was also augmented by a set of publically available data obtained at the 8m Subaru telescope. To constrain the faint-end of the LF, a survey was conducted by using a set of deep parallel data obtained with the Advanced Camera for Surveys (ACS) that was recently installed to the Hubble Space Telescope (HST).

A few dozens of candidates of galaxies at z=6 were found in these surveys, and they will be used for future studies. Stringent limits to the LF were obtained by statistically using the candidates. These constraints agree well with the earlier prediction, indicating that it is close to the real LF. Furthermore, the result from the faint-end survey suggests that the faint-end slope of the LF could be steeper than what was assumed. As an application, the predicted LF was used to calculate the contribution of galaxies to the reionizing background. It was found that dwarf galaxies could be the major souces that were responsible for the reionization.

To Chunmei, my dear wife.

To my parents and my sister.

ACKNOWLEDGEMENTS

First and foremost, my appreciation goes to my thesis adviser, Rogier Windhorst. Thanks to you, Rogier, for your mentoring, guidance and encouragement, for your intuitive ideas that led me through this dissertation, and for using every possible chance to introduce my works to others. Thank you for giving me some many opportunities to lead proposals and observations. Thanks to you for all your help throughout these years.

My heartfelt gratitude to David Burstein. Dave, I learned from you the right way of doing photometry when you visited Xinglong in 1993. Thank you for letting me be aware of the opportunity of graduate study at ASU, and for your enthusiastic and timely help without which I wouldn't be able to get here. And thanks to you for your support during my first two years of study at ASU.

Many thanks to Stephen Odewahn and William Keel for the helpful discussions during the course of this thesis work. Steve, I should especially thank you for your kind help in the two observing runs at the CTIO and KPNO 4m's.

I thank Wei-Hsin Sun for generously letting me use the clone BATC filter set; thanks to Shun-Tang Tseng and Tzong-Liang Cheng for doing observations with me at the Mt. Bigelow.

Thanks to Seth Cohen, Rolf Jansen, Luis Echevarria, Violet Taylor, Nimish Hathi, and other members of Rogier's gang; it has been my great pleasure to work together with your guys. Seth, thank you for your many valuable comments and contributions to the papers and proposals that I led; thank you for being so patient when I bugged you to go over the drafts again and again. Luis, you're the greatest officemate that I have ever known; thank you so much for tolerating me using the entire office for most of the time during the past two years.

Thanks to Yong Li, Wen Xu and Hu Zhan for always being there whenever I need your help; you guys made my first year here much easier than I expected. I thank Xiaohui Fan for his years-long friendship, and especially for his advices during the last year of my graduate study.

I wish to thank all my friends back in China. It's not possible to say it all in this acknowledgment.

Licai, thank you for what you've done in my hardest time, which I made through because of your help. Zhong-Yuan, Wu Hong, Yao-Hua, thank you for all those nights and days that we spent together in the Schmidt dome. Qian-Ming, thank you for making our lives much easier on top of the mountain. My wholehearted thanks to Prof. Xiao-Yang Xia, Zhao-Ji Jiang, Zu-Gan Deng, Hong-Jun Su, Zhen-Long Zou; I remember all the help that you have given me. I also thank Prof. Jian-Sheng Chen for giving me the opportunity to work in his group. The four years and nine months of experience is an invaluable treasure that I'll carry in my heart wherever I go.

TABLE OF CONTENTS

CHAPTER Page

PART II: BRIGHT-END CONSTRAINTS — NOAO 4m Survey

CHAPTER Page

CHAPTER Page

PART V: CONCLUSION

LIST OF TABLES

LIST OF FIGURES

Figure Page

PART I

BACKGROUND AND METHODOLOGY

CHAPTER 1

Introduction

The theme of this thesis work is searching for galaxies at the highest redshift that is currently accessible and constraining the luminosity function of galaxies at this epoch. This chapter introduces the background related to this topic. It is not the intention of this introduction to comprehensively review the rich, sometimes murky, history of the search for high redshift (hereafter high-z) galaxies, which has been the topic of a few excellent articles over the years. This is a history full of both successful and unsuccessful stories, and it well deserves an independent, full-length historical paper. The most recent review on this subject (mostly successful stories) was given by Stern & Spinrad (1999), where the history prior to August 1999 (about the time when this thesis work was started) has been summarized along with the diverse search techniques. A slightly older, but still valuable review was given by Pritchet (1994), where the reader can find a number of interesting ideas about high-z galaxy search in those years.

The organization of this chapter is the following. A few historical notes regarding the searching techniques is given in §1.1 and the most recent progress made in this field is summarized in §1.2. In §1.3 the goal of this thesis is put in the context of understanding one of the greatest cosmological questions, the reionization of the Universe. Some relevant basics about the luminosity function of galaxies are briefly discussed in §1.4. Finally, §1.5 summarizes the goals of this thesis work, and outlines the approach that it takes.

1.1 Searching for High-z Galaxies: Evolution of the Searching Techniques

Ever since Edwin Hubble found the first observational evidence of the expansion of the Universe (Hubble 1929), searching for objects at higher and higher redshifts has been at the frontier of the observational cosmology. The motivation of such pursues is clear: we want to trace the history of the Universe back to its earlier and earlier stages. At first, the main goal of identifying galaxies at higher redshifts was simply to put more data points to the so-called "Hubble diagram" to further test the expansion of the Universe at larger scales. When such an expansion was further confirmed and there were fewer skeptics, searching for high redshift objects, quasars or *normal* galaxies [1], was very quickly recognized as a major means to trace the evolution history of the Universe. Not before long, the fundamental goal of such searches was not only to push the observable boundary of the Universe to larger distances, but also to answer the fundamental question when and how the Universe formed its first generation of nuclear-reaction fueled objects, i.e., primeval galaxies.

Before the mid-1950's, higher and higher redshifts (within $z < 0.2$) were simply obtained by taking spectra of the brightest members of fainter and fainter (and thus presumably more and more distant) galaxy clusters (e.g., Humason, Mayall & Sandage 1956). Later on and until the late 1980's, hunting redshift champions was largely rely on spectroscopic identification of steep-spectrum radio galaxies (e.g., Minkowski 1960, Spinrad 1982, Lilly 1988), and this method was still in use as late as 1999 (Lacy et al. 1994; van Breugel et al. 1999). Interestingly, the search of high redshift galaxies rarely used optical-color-based pre-selection until the early 1990's, although such a method was available and was proved feasible as early as 1958 (Baum 1958; the first ever attempt of obtaining redshift estimate through photometry). This situation was very different from the search of high-z quasars, where optical-color-based pre-selection has been routinely used ever since Sandage & Luyten (1967) pointed out that the color of quasars were significantly different from field objects (mainly stars). Such a dramatic difference in searching strategies may be due to the fact that galaxies at different redshifts (generally $z < 2$ before the late 1980's) do not have color contrasts as large as those of quasars vs. field objects, and in the "old time" when photometry was largely done on photographic plates it was not easy to obtain photometry of sufficient accuracy to discriminate

[1] In this thesis the terms "normal galaxies" and "galaxies" are used to mean "non-active galaxies", and are always used in a relative sense as compared to "quasars". Quasars are the most luminous *active galactic nuclei* (AGN), and therefore they are part of their host galaxies. This thesis does not make such a pedagogic distinction.

galaxies of highest redshifts against their counterparts at lower redshifts. The work of Baum (1958) was based on photoelectric observation, which was much more accurate than photographic imaging, but could only be done on a one-by-one basis and thus was not efficient enough as a pre-selection method. Unless a strong feature presents in the spectral energy distribution (SED) of high-z galaxies, photometric pre-selection is not likely to be efficient.

It was widely recognized in the late 1970's that one such strong feature, Lyα emission line at rest-frame 1216Å, could present in high-z galaxies provided that they were in an active star-forming process (e.g. Hogan & Rees 1979). Throughout the 1980's and the early 1990's, searching for redshifted Lyα emission was the most popular method in the high-z galaxy hunt. Among all the variants, narrow-band imaging was the most intensively used approach. For this purpose, a narrow-band filter was made such that its central wavelength was at the Lyα line of a desired redshift, and images were taken through this narrow-band filter as well as a broad-band filter, which served as the continuum filter. Candidates of Lyα emitters could be pre-selected based on their large narrow-band vs. continuum-band color.

Starting the mid-1980's, it was realized that it was possible to search for high-z galaxy companions to high-z quasars ($z > 2$–3), as quasars are supposed to be good mass-tracers. Indeed, a few such high-z galaxy candidates were pre-selected around high-z quasars by narrow-band imaging with CCD cameras and were later spectroscopically confirmed (e.g., Djorgovski 1985, Hu & Cowie 1987, Steidel, Dickinson & Sargent 1991, Hu et al. 1991). Narrow-band filters were used in these cases for pre-selection because they were capable of picking up the Lyα emission line, which, as a good indicator of active star-forming activities, was believed to present in the galaxies at $z > 2$. Narrow-band imaging was also used to search for companions around high-z radio galaxies with HST/WFPC2, and was quite successful (e.g., Pascarelle et al. 1996).

However, high-z galaxies pre-selected as physical companions to known quasars or radio galaxies cannot be taken as the representatives of high-z galaxies in general, as their star-formation processes were obviously affected by their massive neighbors. Moreover, some of such companions do not have their own stellar components and their Lyα emission is simply the result of the photoionization caused by the nearby quasars. To obtain an unbiased view of star-formation, a large sample of *field* galaxies at high-z is needed. Unfortunately, narrow-band imaging and other type of surveys (e.g., slitless spectroscopy) on "blank" sky aiming at pre-selecting galaxies with strong Lyα emission line was not successful for a long period of time (see Pritchet (1994) for a detailed review). The reasons for such failures are somehow mysterious; it is possible that one of the reasons was the technology limit that prohibited the surveys to reach sufficient depth and sky coverage.

The field was revolutionized by a new pre-selection method, which is now usually referred to as the "Lyman-break method" or the "drop-out selection". This method was first developed by Steidel & Hamilton (1992) who initially aimed at detecting the $z = 3.39$ Lyman limit absorption system that manifests itself in the spectrum of a $z = 4.106$ quasar (Hazard et al. 1986, Sargent, Steidel & Boksenberg 1989). The Lyman limit systems (LLS) saw in the quasar spectra were long speculated to be originated in the galaxies that lie in the sight-lines to those quasars, and Steidel & Hamilton (1992) suggested that the LLS, if really in the form of galaxies, should be discernible through the strong continuum discontinuity that could be detected by specifically designed broad-band imaging. At $z \simeq 3$, this continuum discontinuity (or so-called "Lyman-break") occurs at the Lyman limit (rest-frame 912Å). The photons emitted by the galaxy at wavelengths bluer than the Lyman limit are capable of ionizing neutral hydrogen and thus are quickly absorbed by even a slight amount of intervening neutral hydrogen along the sight-line. As a result, a strong break in the continuum should be visible across rest-frame 912Å. If such a galaxy is imaged in a blue filter and a red filter that are bluer and redder than the Lyman limit, respectively, it should be visible in the red image but invisible, or "drop-out", in the blue image. Using this method, Steidel & Hamilton (1992) successfully identified the $z = 3.39$ LLS that they sought for, and argued that this method had more advantages over narrow-band imaging as it utilized broad-band imaging and therefore was much easier to reach deeper survey limit.

In the meantime, Steidel et al. clearly realized that such a method was not limited to the search of the LLS, because any galaxies at sufficient redshifts should have this strong signature in their spectral energy distribution (SED). By using this method to "blank" fields (i.e., containing no known quasar), Steidel et al. (1996a, 1996b) successfully pre-selected a large number of field galaxies at $z \simeq 3$, most of which were spectroscopically confirmed by using the 10m Keck telescope. This method was full-fledged from then on, and has been gradually push to $z \simeq 4$ (e.g., Steidel et al. 1999) and $z \simeq 5$ (e.g., Weymann et al. 1998). It should be pointed out that at $z \simeq 4$ and beyond the Lyman-break signature no longer occurs at rest-frame 912Å but moves to 1216Å.[2] This is because at such high redshifts a sight-line goes through more intervening neutral hydrogen clumps, and the Lyα and Lyβ absorption forests due to such thick neutral hydrogen clouds are so severe that they effectively quench the UV continuum emission blueward of rest-frame 1216Å (see Madau 1995).

On the other hand, the efforts of discovering high-z galaxies through detecting their Lyα emission line did not stop. With the new 8–10m class telescopes (especially the two Keck telescopes) that came into operation in the 1990's and the new generation of large-format, red-sensitive CCD cameras, such efforts finally resulted in positive detections, which will be discussed below.

1.2 Recent Progress of High-z Searches

Understandably, the term "high-redshift" has been changing in meaning over the years. Nowadays it usually refers to $z > 5$, although some people still take it as $z > 1$. From now on the term means $z > 5$ in this thesis, and only the progress in this regime will be reviewed[3]. Furthermore, this section only discusses the results that have been spectroscopically confirmed.

The *magical* (or psychological) redshift barrier, $z = 5$, was broken in 1998 when Dey et al. (1998) announced their discovery of a $z = 5.34$ galaxy. For decades this was the first time that the

[2]While this rest-frame 1216Å signature is also called the "Lyα discontinuity", this thesis does not make this distinction.

[3]Searches of galaxy companions around known quasars are not discussed here.

redshift record was broken by a galaxy rather than a quasar. Ironically, this high-z champion was serendipitously discovered during the spectroscopic identification of a B-band drop-out candidate at $z = 4$. The same slitlet that targeted on this $z = 4$ candidate was fortunate enough to also include another faint object only 1.2" away and a strong emission line from this object was detected at 7717Å. Based on the asymmetric profile of this line and the fact that this faint object is a R-band drop-out but visible in the I-band, the emission line was identified as Lyα and thus gave a redshift of 5.34.

The record was quickly broken months later by a $z = 5.60$ galaxy discovered by Weymann et al. (1998) in the Hubble Deep Field North (HDF-N; Williams et al. 1996). This galaxy was first pre-selected as a F606W-band (approximately V-band) drop-out (Lanzetta, Yahil & Fernandez-Soto 1996), and the deep imaging with NICMOS Camera 3 (NIC3) in the F110W and F160W (approximately J and H bands) showed that its colors at longer wavelength were consistent with the interpretation of its being at $z > 5$ (Weymann et al. 1998). A total of 2.5 hours of spectroscopic observation at the Keck telescope identified a weak but robust Lyα emission line at 8029Å, and hence confirmed its high-z nature.

The redshift race was going at a dizzy speed in the years that followed. Spinrad et al. (1998) reported another $z = 5.34$ galaxy – actually a galaxy pair – that had been spectroscopically confirmed, which was also in the HDF-N and was pre-selected as a V-band drop-out (Fernandez-Soto et al. 1999; Lanzetta et al. 1996). [4] This is the first $z > 5$ galaxy whose redshift was not determined by an emission line (no detectable emission line in its spectrum) but by its continuum break. In the meantime, van Breugel et al. (1999) identified a $z = 5.19$ radio galaxy, which was selected based on its ultrasteep radio spectral index. This is the brightest known high-z radio galaxy.

Very quickly, a galaxy at an even higher redshift, $z = 5.74$, was found by Hu et al. (1999) in their narrow-band imaging survey done with the Low Resolution Imaging Spectrograph (LRIS) at

[4] This candidate was selected by these authors based on its photometric redshift (z_{phot}); however its z_{phot} largely relied on the Lyman-break signature because the IR data were not deep enough to give actual photometric information. Therefore it is more appropriate to take this candidate as pre-selected by drop-out technique.

the Keck, and a subsequent 5-hour spectroscopic Keck observation confirmed the redshift. This new record holder is similar in its continuum shape, line properties, and observed equivalent width to the $z = 5.60$ galaxy of Weymann et al. (1996), but is ~ 20 times more luminous in the line and in its red continuum.

Interestingly, it was soon realized that the "serendipitous" detection of Lyα emission line as the case in Dey et al. (1998) could be carried out in a "systematic" way (Manning et al. 2000) if the searching sensitivity is approaching a few $10^{-17} erg \cdot cm^{-2} \cdot s^{-1}$, given the likely high surface density at this level. Indeed, two more $z > 5$ galaxies [5] were found in this way in the flanking fields to the HDF-N (Dawson et al. 2001) during the course of a systematic spectroscopic identification campaign of $z \simeq 3$–4 Lyman-break galaxies at the Keck LRIS. While these authors believed that the one identified with $z = 5.767$ might need further investigation, they were positive that the one with $z = 5.631$ was certain. Serendipity again showed its magical power one year later, when a similar approach (but with a different instrument) resulted in yet another $z > 5$ galaxy, identified as having $z = 5.190$ (Dawson et al. 2002).

All these galaxies are very faint. To collect a sizable sample at $z > 5$, it is likely that working at the very limit of the largest facilities currently available will be inevitable, as the above discoveries indicate. If one wants to push to even higher redshifts, where the galaxies are presumably even fainter and their number density is less, the situation will be worse.

A new search technique based on gravitational lensing has been proposed to try to by-pass this problem. The idea was to search for high-z objects around galaxy clusters, and hope that the clusters, which act as strong gravitational lenses, can amplify the brightness of the high-z objects behind them — if they do present — such that these intrinsically faint objects can be easily detected. The serendipitous discovery of a pair of $z = 4.92$ galaxy images (Franx et al. 1997; the highest redshift ever recorded at that time) lensed by the foreground $z = 0.33$ cluster CL 1358+62 greatly encouraged

[5] Throughout that paper it is stated that five more $z \geq 5$ galaxies were found; however, the number should actually be two instead of five based on what they said in the paper. The author suspect that what they really meant was "five more $z \geq 4$ galaxies", as the number of such galaxies in their Table 2 is indeed five.

Table 1.1: The Status of High-z ($z > 5$) Galaxy Search as of December 2002

Date[a]	z	Technique	Search Area[b]	mag[c]	Line Strength[d]	Ref[†]
1998 Feb	5.34	Serendipity	—	26.1	3.5; 600Å	(1)
1998 Jul	5.60	Lyman-break	0.73	26.6–27.1	1.0; —	(2)(10)
1998 Aug	5.34	Lyman-break	5.7	25.6	—; —	(3)(10)
1999 Mar	5.19	Radio	—	—	—	(4)
1999 Mar	5.74	Narrow-band	30	25.5	1.7; 175Å	(5)
2001 Feb	5.63	"Systematic" Serendipity	2.2	—	—; 300Å	(6)
2001 Aug	5.58	Lensing/Spectroscopic	—	25.9	5.6; —	(7)
2001 Nov	5.19	Serendipity	—	25.6	3.0; 740Å	(8)
2002 Jan	6.56	Lensing/Narrow-band	—	25.4	2.7; 190Å	(9)

a. The dates were taken as the manuscipt received dates.
b. In arcmin^2.
c. Continuum magnitudes (in AB system) to the red side of the Lyman-break.
d. The first value is observed the line flux in $10^{-17}\, erg \cdot cm^{-2} \cdot s^{-1}$, and the second value is the equivalent width in observer's frame.

†. (1) Dey et al. 1998; (2) Weymann et al. 1998; (3) Spinrad et al. 1998; (4) van Breugel et al. 1999; (5) Hu, McMahon & Cowie 1999; (6) Dawson et al. 2001; (7) Ellis et al. 2001; (8) Dawson et al. 2002; (9) Hu et al. 2002; (10) Lanzetta, Yahil & Fernandez-Soto 1996.

the application of this approach. Ellis et al. (2001) have begun a systematic spectroscopic survey, where they used long-slit (the Keck LRIS) to scan the regions around a few clusters to search for such amplified Lyα lines. So far this survey found one galaxy at $z = 5.6$, whose intrinsic brightness was amplified by more than 30 times. A similar search around lensing clusters, but using narrow-band imaging (also using LRIS at Keck), was conducted by Hu et al. (2002) and resulted in a galaxy with the highest redshift so far: $z = 6.56$. This discovery raised some concerns, which will be discussed in §1.4 below.

The progress mentioned above, which gives the status as of December 2002, is summarized in Table 1.1. It is interesting to note that only two of these discoveries were based on the Lyman-break selection, while the vast majority (seven out of nine) were made by searching for Lyα emission line, either directly (spectroscopic "scanning") or indirectly (narrow-band imaging). The fruitless efforts along this line of search less than a decade ago thus seem mysterious, as the depth reached by those earlier studies (if we believe such claims) was comparable to the depth of the current surveys.

Finally, it is worthwhile to also briefly mention the progress made in the hunt of high-z quasars, as some of those results will be used later.

As of December 2002, thirteen $z \geq 5$ quasars have been published with spectroscopically confirmed redshifts. Amazingly, similar to the high-z galaxy search, most of these discoveries were made within two years after a long halt. The first such quasar at $z = 5.00$ (Fan et al. 1999) was discovered in the Sloan Digital Sky Survey (SDSS; York et al. 2000), almost one year after the discovery of the first $z > 5$ galaxy. Several months later, the SDSS pushed the record forward slightly with a $z = 5.03$ quasar found by Fan et al. (2000a). A significantly larger record, $z = 5.50$, was soon set by Stern et al. (2000) using a completely different data set, which were meant to be used to search for high-z galaxies. This record was very quickly broken by a $z = 5.80$ [6] quasar of Fan et al. (2000b). One year later, the SDSS group again set a new record, $z = 6.28$ (Fan et al. 2001). Besides these record holders, some other $z > 5$ quasars were also published from 2000 to 2001. These include Zheng et al. (2000; z=5.27) and Anderson et al. (2001; z=5.00, 5.09, 5.11, and 5.41) using the SDSS data, and Sharp et al. (2001; z=5.17) using the Isaac Newton Telescope (INT) Wide Angle Survey (WAS; McMahon et al. 2000) data.

Two aspects regarding these findings should be noted. First, all these $z > 5$ quasars were preselected based on optical-color selection techniques that are very similar to the drop-out method used for high-z galaxy searches. Although their detailed color selection criteria have some subtle differences, they are in principle the same. This is because the cosmic intervening neutral hydrogen along the sight-lines is fair to either quasars or galaxies at redshifts past 5 — the photons emitted at the bluer side of rest-frame 1216Å from any of such objects are largely absorbed before they reach us. As a consequence, the quasar selection criteria are mostly determined by this effect rather than by the intrinsic SED of quasars, as is the case at lower redshifts. Therefore, the drop-out selection used to search for high-z galaxies can also result in high-z quasars if they are PRESENT in the

[6] Djorgovski et al. (2001) revised its redshift to 5.73, which the SDSS group seemed to agree on (See the note of Fan et al. 2001 on this object).

field of searching, as the $z = 5.50$ quasar of Stern et al. (2000) indicates. Second, all but one of these $z > 5$ quasars are very luminous (M_{AB}(1450Å)~ -25 mag). This is not surprising, because the survey limits of the SDSS and the WAS are designed to reach the depth sufficient to find only the brightest quasars at high-z. The only exception, the $z = 5.50$ quasar of Stern et al. (2000), has M_{AB}(1450Å)~ -23.0 mag and is at the conventional dividing line of quasars and AGN. Their imaging data reached at least three magnitudes deeper, but surveyed only ~ 70 arcmin^2 in area. This raises an interesting question: is the number density of high-z quasars increasing so rapidly toward the faint end? This question will again be discussed later in this thesis.

1.3 Reionization of the Universe Ended at $z \simeq 6$

In the standard big-bang model, the Universe cooled as it expanded. When its temperature reached below several thousand degrees, the primeval plasma began to recombine and the matter in the Universe became predominantly neutral again. This process is called the *recombination of the Universe*, and it occurred at a redshift of $z \sim 10^3$ (e.g., Peebles 1968). After the recombination, the Universe remained in the "dark ages" until galaxies formed as gravitationally bound, star-forming systems. The strong Lyman continuum photons from the first generation of stars and/or quasars ionized the neutral hydrogen gas around galaxies and formed isolated, giant H II regions surrounding galaxies. As the time progressed, these H II regions grew and started to overlap each other. This cosmic process of ionizing neutral hydrogen is called the *reionization of the Universe*, which ended by the time when virtually all the giant H II "bubbles" in the Universe overlapped (see for example Gnedin 2000). Qualitatively, this is a picture not difficult to grasp. However, quantitatively when and how the reionization began are among the most fundamental cosmological questions that remain unanswered (for extensive reviews, see Barkana & Loeb 2001 and Loeb & Barkana 2001).

The precise epoch of reionization has been long sought for through the so-called "Gunn-Peterson effect". Right after Schmidt (1965) identified the radio source 3C 9 as a quasar at $z = 2.012$, a stunning redshift at that time, Gunn & Peterson (1965) [7] quickly noticed that the optical depth to the Lyα photons because of the resonance scattering due to neutral hydrogen atoms was not as large as one would expect if this quasar was embedded in a smooth, largely neutral intergalactic medium (IGM). If the Universe were stationary, only the photons emitted within an extremely narrow window centering on 1216Å would suffer from the Lyα resonance scattering; however, in an expanding Universe, the photons emitted at shorter wavelengths can redshift into the scattering layer and thus this resonance scattering depression of continuum should be seen over a much wider range of wavelength to the bluer side of rest-frame 1216Å. Based on their measurement of the flux depression using the original discovering plates of Schmidt (1965), Gunn & Peterson (1965) estimated that the optical depth to the Lyα photons due to resonance scattering as $p = 1/2$. Although this was only a very rough estimate (and the actual value is much less), the neutral hydrogen density inferred from this value was clearly much lower than expected. Therefore, they concluded that

> *"We are thus led to the conclusion that either the present cosmological ideas about the density are grossly incorrect, and that space is very nearly empty, or that the matter exists in some other form. Oort has shown that only about 1 per cent of the* $q_0 = \frac{1}{2}$ *density is accounted for by galaxies, and it has been generally assumed that the remainder exists as an intergalactic gas which is presumably mostly or entirely hydrogen. It is possible that this interpretation is still valid but that essentially all of the hydrogen is ionized; this conclusion can be defended if we are allowed to make the intergalactic electron temperature high enough."*

This was the first evidence that the Universe was still largely ionized at considerably high redshift. Reversing the argument of Gunn & Peterson (1965), one concludes that a strong continuum

[7] Scheuer (1965) reached the same conclusion independently at the same time; however he gave only rather qualitative argument (in the "Letter to the Editor" column of *Nature*, and less than one page long), while Gunn & Peterson (1965) present much more elaborated analysis. Also, Shklovskij (1964) seemed to have similar idea before all the others; however I do not have access to the Russian journal (Astron. Tsirk; or Astronomical Circular) where he published his paper.

suppression across Lyα , which is referred to as the “Gunn-Peterson trough” (GP trough), should present in the spectrum of an object at the epoch before the reionization ended (see Haiman & Loeb 1999 for detail). Note that this absorption is due to a smoothly distributed neutral hydrogen substrate, and is different from the line absorptions, such as the “Lyα forest”, that are caused by the residual neutral hydrogen in clumpy forms that survived into the post-reionization age.

The GP trough has been searched for in the spectra of quasars at higher and higher redshifts [8] ever since it was realized that this trough can be used as an important means to precisely determine the reionization epoch. However, the GP trough was not detected in early attempts (e.g., Giallongo et al. 1993, and references therein). What all such efforts have shown is a gradual thickening of Lyα forest with increasing redshift, even when the redshift boundary was pushed to $z \sim 5$ and beyond (Songaila et al. 1999; Djorgovski et al. 2001).

The first unambiguous detection of a complete GP trough was discovered by Becker et al. (2001) in the high resolution spectrum of the $z = 6.28$ SDSS quasar, whose existence had been suggested based on the discovery (low resolution) spectrum of this quasar (Fan et al. 2001). Given the fact that such a trough was not seen in the spectra of other quasars with redshifts as high as $z = 5.99$, Becker et al. (2001) tentatively suggested that we had seen the *end* of the reionization in the spectrum of this $z = 6.28$ quasar. In a more elaborated investigation where they provided a detailed analysis on the spectra of $z > 5.8$ SDSS quasars, Fan et al. (2002) further argued that the epoch of reionization could not be at a redshift much higher than 6. This is also consistent with the most recent numerical simulations of cosmological reionization (e.g., Cen & McDonald 2002), where it is suggested that the IGM is likely neutral at $z > 6.5$.

On the other hand, the discovery of a $z = 6.56$ Lyα emitter by Hu et al. (2002; see §1.2), which was made shortly after this detection of GP trough, raised a different opinion. It has been pointed

[8]The GP trough should exist in the spectra of any objects located beyond the reionization; see, for example, Miralda-Escude (1998). Such a search was very rarely done in the spectra of galaxies for the sole reason that the high-z galaxies, unlike the luminous quasars, are not bright enough for us to obtain spectra of sufficient S/N to really measure this trough.

out that the GP trough has a *red* damping wing, which can "eat out" a large portion of the Lyα emission line or even completely quench the line (Miralda-Escude 1998; Miralda-Escude & Rees 1998). Hu et al. (2002) therefore argued that the presence of even a single object at this redshift may suggest we have not yet reached the redshift of reionization.

Nevertheless, the detectability of Lyα emission line *prior* to the reionization was investigated by Haiman (2002), who pointed out that such a line, if broad enough, could still be observable, and thus the Lyα emitter of Hu et al. (2002) might actually lie *beyond* the epoch of the reionization. Very recently, Cen (2002) proposed a scenario that the Universe was actually reionized twice, which could also explain the seemingly-paradoxical detection of this $z = 6.56$ Lyα emitter. Furthermore, if the distribution of neutral hydrogen at the epoch of reionization was patchy rather than homogeneous, there is no conflict at all because the reionization then would not be uniform and the reionization process along one sight-lines could still not yet finish while it could be done already along the other sight-lines (cf. Miralda-Escude & Rees 1998).

To summarize, currently the general consensus is that the reionization of the Universe ended at around $z \simeq 6$, and this redshift marks a milestone in the evolution history of the Universe. Thus the assessment of $z \simeq 6$ galaxy number counts at different brightness levels will have a very direct cosmological impact, since it will quantify the number density of UV-emitting objects that are the physical cause of the reionization.

1.4 Luminosity Function of Galaxies

For a given type of objects, their number count distribution as a function of their luminosity is what we call "luminosity function" (hereafter LF), which is one of the most important elements that we can observationally gather to understand the statistical properties of this type of objects as a whole. For galaxies, studying their LF and its evolutionary trends over time directly leads to the understanding of galaxy formation and evolution, which, ultimately, will lead to a quantitative understanding of the structure formation and evolution history of the Universe. Although conceptually simple, deriving a reliable LF is not an easy matter in practice. There are some excellent reviews on this subject (e.g., Takeuchi, Yoshikawa & Ishii 2000), and this section will only discuss a few most relevant basics.

The LF of galaxies is usually expressed by the Schechter function, named after Paul Schechter who proposed this simple analytic form and demonstrated how well it fitted the observational data (Schechter 1976). Letting $\Phi(L)dL$ be number of galaxies per unit volume in the luminosity interval from L to $L + dL$, the Schechter function can be written as

$$\Phi(L)dL = \Phi^* \left(\frac{L}{L^*}\right)^{\alpha} exp(-\frac{L}{L^*})d\left(\frac{L}{L^*}\right),$$

where Φ^*, L^* and α are free parameters to be determined from the data. Φ^* fixes the normalization, Ł* is the "characteristic luminosity", and α is the so-called "faint-end slope". The relation between $\Phi(L)$ and L is better visualized on the $log(\Phi)$ vs. $log(L)$ plane, where it can be clearly seen that the LF shows a rapid change in slope at L^*, and α is the slope of the curve at $L \ll L^*$. According to Schechter (1976), this form was based on a simple formalism that was developed by Press & Schechter (1974) to describe how the structures in the Universe are built up by the process of hierarchical clustering according to the Cold Dark Matter (CDM) scenario:

> *The proposed representation derives from a self-similar stochastic model for the origin of galaxies ... but differs in that we allow ourselves the latitude of adjusting the "faint-end sloe parameter"* α *to fit the available data. The thrust of this work is not therefore to argue the merits of the stochastic model, but only the merits of the expression as a good approximation to the luminosity function.*

However, it was not shown how one could reach the form of Schechter function from the Press-Schechter formalism that specifies the number of dark matter halos within unit mass interval as a function of their masses. To the best of my knowledge, no such a "derivation" exists in the literature. At a first glance it seems that adopting a reasonable mass-to-light ratio can simply make the conversion happen; however, this actually is not as straightforward as such. Therefore, it might not be desirable to interpret the physics under the Schechter function, and the best attitude should be treating it as an excellent empirical law (as Schechter himself indicated).

In practice, it is more convenient to express the Schechter function in the magnitude domain:

$$\Phi(M) = 0.921 \cdot \Phi^* \cdot 10^{0.4(\alpha+1)(M^*-M)} \cdot exp\left[-10^{0.4(M^*-M)}\right],$$

where M is absolute magnitude, and M^* is the absolute magnitude corresponded to L^*. The above form is also valid if we use apparent magnitudes instead, because $(M^* - M) = (m^* - m)$[9]. Therefore, the most frequently used Schechter function form in this thesis is

$$\Phi(m) = 0.921 \cdot \Phi^* \cdot 10^{0.4(\alpha+1)(m^*-m)} \cdot exp\left[-10^{0.4(m^*-m)}\right].$$

If the LF of galaxies at different redshifts is measured, valuable information can be obtained by studying its evolutionary trends. However, such a study requires redshift information, which is difficult to obtain for a large collection of galaxies. While the LF of galaxies in the local Universe has been quite reasonably determined (although there are still some inconsistencies among different surveys), very little is known at higher redshifts, especially at $z \geq 1$. The only exception is the LF at $z \simeq 3$, which has been well measured based on a large sample of galaxies selected at this redshift regime by the Lyman-break technique and identified spectroscopically at the Keck telescope (Steidel et al. 1999). This measurement provides a starting point for the work that will be presented in Chapter 2.

1.5 The Goals and the Approach

The major goals of this thesis can be summarized as the following:

1. *Searching for galaxies at the important cosmological epoch of $z \simeq 6$.* Clearly, if we are to understand the global status of the Universe in its early stage, we first need to collect a sizable

[9]Strictly speaking, this is valid only if all the galaxies under question are at the same redshift. Since we are going to study a (relatively) narrow redshift range, the small difference caused by slightly different distances is ignored here.

sample of objects at the highest accessible redshift, currently at $z \simeq 6$. Therefore, the exploration in this little known territory justifies itself in every aspect. No matter what the outcome will be, the result of such a study will certainly have its impact on our understanding of the early history of the Universe, provided that the search is carefully designed and its characteristics, such as possible selection bias, are well understood.

2. *Constraining the luminosity function of galaxies at $z \simeq 6$.* Constructing the LF requires a significant sample of galaxies with spectroscopic redshifts. However, it was clear to the author at the very beginning that the spectroscopic identification of a statistically sufficient number of objects was far beyond the scope of this thesis, and possibly even beyond the reach of any existing facilities. Thus the goal is to constrain the LF rather than to actually construct it. Such a result will not only serve as a guide to the high-z search activities in the next few years, but will also have a long-term impact to a number of cosmological questions.

3. *Revealing the major sources that were responsible for the reionization of the Universe.* The hydrogen in the Universe is known to be fully ionized at $z \simeq 5$, and the sources of such an ionizing background have not yet been identified. The latest progress at $z \simeq 6$ regime has suggested that we might have finally reached the epoch when the hydrogen was not fully ionized, i.e., the epoch of reionization. An immediate question thus is: what are the sources that provided the reionizing background at $z \simeq 6$? This is the question that this thesis will try to address.

This thesis work started from an *educated guess*, or a prediction, of the LF of galaxies at $z \simeq 6$. After verifying that such a prediction is at least consistent with limited observations at hand, new observations were carried out. The results of these observations were then used to further constrain the LF. Finally, as a directly application, the LF was used to answer the question about the sources of reionizing background.

CHAPTER 2

The LF of Galaxies at $z \simeq 6$: An Educated Guess

The various techniques of searching for high-z galaxies have been outlined in the previous chapter. Given the constraint of the observing facilities to which we have access, a pre-selection based on optical surveys is the most realistic.

Despite the tremendous amount of efforts in the past, the number of known $z \simeq 6$ galaxies is still small. By the time when this thesis work was started in late 1999, there were only two spectroscopically confirmed galaxies at $z > 5.5$ (Weyman et al. 1998; Hu et al. 1999). While such a small number partially reflects the limit of technology, more importantly it suggests a genuine galaxy number density decrease as we look further and further back. Thus an optimized survey strategy needs to be developed: we need to know how large an area should be surveyed, how deep the survey should reach, and how many objects we can expect. [1]

2.1 An Outline of the Prediction

For the sake of simplicity, here the redshift range of interest is chosen as $5.5 \leq z \leq 6.5$ ($z \simeq 6$ for short).

There are a few theoretical predictions on the surface density of galaxies at high redshifts, either based on N-body simulations (e.g. Weinberg et al. 1999, 2002) or based on semi-analytic formalisms (e.g. Robinson & Silk 2000). However, those predictions are more qualitative than quantitative at this point, because they either are limited by finite volume and finite resolution, or have to rely on several parameters which remain very uncertain in the absence of significant amounts of actual data.

[1] The study presented in this chapter has resulted in a pubished paper (Yan et al. 2002).

Thus one may prefer not to base survey plans directly on such predictions at the moment.

Here we present a simple, observational approach. We may *assume* a reasonable LF for galaxies at $z \simeq 6$ by *extrapolating* the known results at $z \simeq 3$, which is the highest redshift where the LF of galaxies has been quantified over a wide enough brightness range (Steidel et al. 1999). We will use existing data at $z \gtrsim 5$ to constrain the normalization of this *extrapolated* luminosity function. Once the $z \simeq 6$ LF is estimated in this way, the surface density can be calculated in a straightforward manner, *i.e.*, by numerically integrating the LF over the volume occupied by unit sky-coverage in the redshift bin of interest.

2.2 Detailed Procedures

2.2.1 The Extrapolated Luminosity Function

The starting point is the $z \simeq 3$ LF from Steidel et al. (1999), who merged the ground-based and the HDF-N Lyman-break galaxy samples. Since the $z \simeq 3$ sample used in Steidel et al. (1999) was selected based on the Lyman-break signature in the SED of galaxies, our approach makes the implicit assumption that galaxies at higher redshifts also manifest themselves by the Lyman-break feature. Because the line-of-sight intervening H I absorption is more severe at higher redshifts and the effective break moves from the 912Å Lyman limit to the Lyα line at 1216Å (e.g. Madau 1995), one can expect that the Lyman-break signature is even stronger, therefore our assumption is likely valid. However, there might exist a different type of galaxy whose UV-photons are completely absorbed by dust, like the ultraluminous infrared galaxies that are known to exist at lower redshifts. There is no Lyman-break for such galaxies, since they have essentially zero flux from the UV to the optical range. Our predictions neglect these objects, because they are also absent from the Lyman-break samples at $z \simeq 3$. Since we deal with the emitted UV, such objects will not affect our conclusions.

The details of the LF extrapolation from $z \simeq 3$ to $z \simeq 6$ depend on the adopted cosmological model. Different cosmological parameters will change the apparent magnitude of an object with a given intrinsic brightness, and will also affect the physical volume corresponding to a given sky coverage. We consider three cosmological models, namely, a flat universe without cosmological constant ($\Omega_M = 1$ and $\Omega_\Lambda = 0$), a flat, low mass universe with $\Omega_M = 0.3$ and $\Omega_\Lambda = 0.7$, and an open universe without cosmological constant ($\Omega_\Lambda = 0.2$ and $\Omega_\Lambda = 0$). For simplicity, we denote the three models by their Ω_M and Ω_Λ values as the (1, 0), (0.3, 0.7), and (0.2, 0) models, respectively. Throughout this thesis we use a Hubble constant of $H_0 = 65\, km\ s^{-1}\ Mpc^{-1}$. All the quoted magnitudes are AB magnitudes and, unless noted otherwise, refer to the continuum at the rest-frame $1400 - 1500$Å range.

The LF of $z \simeq 3$ galaxies of Steidel et al. (1999; in their section 4.3) is a Schechter function (see §1.3 above). The L^* galaxies at this redshift have $\mathcal{R}$-band apparent magnitude of $m^* = 24.48$ mag. At $z = 3.04$ (the median redshift for Steidel et al.'s sample), this m^* value corresponds to $M^* = -20.37$, -21.23 and -21.31 mag in the (1, 0), (0.3, 0.7) and (0.2, 0) models, respectively. The $\mathcal{R}$-band has central wavelength of $\lambda_0 = 6930$Å, or ~ 1700Å in the rest-frame at $z \simeq 3$. Since the SED of a young non-dusty galaxy in f_ν is essentially flat from $1400 - 1700$Å, these magnitudes apply to the $1400 - 1500$Å range as well. As a first approximation, we also assume that there is no significant luminosity evolution for galaxies from $z \sim 3$ to $5.5 \leq z \leq 6.5$, such that L^* galaxies at $5.5 \leq z \leq 6.5$ still have the above mentioned absolute magnitudes. Possible evolution effects will be discussed later. We noticed that Steidel et al. (1999) made a similar assumption in comparing the ground-based + the HDF-N sample at $z \simeq 4$ to its counterpart at $z \simeq 3$, concluding that the observed $z \simeq 4$ galaxy distribution was completely consistent with such an assumption at the bright end, and within a factor of two at the faint-end. In fact, they suggested that the faint end mismatch was due to the genuine structure in the small HDF-N field, rather than a true luminosity function discrepancy. As for the faint-end slope α, we also adopted the value obtained at $z \simeq 3$ for now, which is $\alpha = -1.6$.

Next we choose a normalization to fix the luminosity function, which amounts to allowing density evolution. Observationally, this can be done by adjusting Φ^* such that the calculated surface density, either differential or cumulative, matches the available observations. This is difficult in our case, since there is no precise observed value to be used. There are only four published $z > 5.5$ galaxies with spectroscopic information.[2] These are the z=5.60 galaxy in the HDF-N (Weymann et al. 1998), the z=5.74 galaxy in the Hawaii Survey Field SSA22 (Hu et al. 1999), and the z=5.767 and z=5.631 galaxies in the HDF-N flanking fields (Dawson et al. 2001). Statistically, these results are inadequate for the purpose of normalization, because their selections are not readily quantifiable. Nevertheless, we can still make a rough estimate of the cumulative surface densities of $z \geq 5.5$ galaxies in the well-studied HDF-N and use this value as our normalization. We consider two cases: a cumulative surface density of 1.37 per arcmin^2 and of 0.11 per arcmin^2, both to a limit $m_{AB} = 27.0$ mag. The former case (high normalization) is equivalent to *one* $z \geq 5.5$ galaxy per NIC-3 field (c.f. Thompson et al. 1999) and the later one (low normalization) is equivalent to *one* such galaxy per WFPC2 HDF coverage. Note that $m_{AB} = 27.0$ mag is *not* the magnitude of this z=5.60 galaxy, but an estimate of the selection limit in the HDF-N for a galaxy at $z \geq 5.5$ as observed at $9100 - 9800$Å.

2.2.2 The Predicted Surface Densities

Cumulative surface densities can now be calculated by numerically integrating the luminosity function over the volume occupied by unit sky coverage in the range $5.5 \leq z \leq 6.5$. Figure 2.1 shows these results, where the cumulative surface density is presented as the total number of galaxies per deg^2, whose brightness is brighter than a specified apparent AB magnitude. The predictions for the (1, 0), (0.3, 0.7) and (0.2, 0) models are plotted in solid, long-dashed and short-dashed lines, respectively. Thick lines are used for the high normalization case, while thin lines are used for the low normalization one. The absolute magnitude scales are labeled on top of the figure, from bottom to the top for the (1, 0), (0.3, 0.7) and (0.2, 0) models, respectively. The M^* values for these models are labeled in the legend in the parenthesis together with the corresponding apparent magnitudes, and are also indicated along the absolute magnitude scales at the top by upward arrows. Numerical

[2] The $z = 6.56$ Lyα emitter of Hu et al. (2002) is ignored for now, first because it was not available at the time when this part was written, and second because it is gravitationally lensed and its brightness is therefore not representative.

results are presented in Table 2.1, where the number density is listed as number of galaxies per arcmin^2 for straightforward use in planning future observations.

2.3 Consistency Check from Limited Observations

The LF at $z \simeq 6$ predicted above through *extrapolation* seems to be very crude at best. As a minimal consistency check, we compare our predictions to the limited (direct and indirect) observations in hand for galaxies at $z \simeq 6$.

2.3.1 The Faint End ($m_{AB} > 25$ mag)

A lower limit at this brightness level can be obtained from the $z = 5.74$ galaxy of Hu et al. (1999), assuming that its single strong emission line identification is reliable. The galaxy's Z-band magnitude (free of the emission line), which is similar to the SDSS z'-band magnitude, is 25.5 mag. Since their survey area is about $390'' \times 280''$, a simple lower limit estimation is $log(N)$ =2.07 deg^{-2} to $m = 25.5$ mag. This lower limit is indicated on Figure 2.1 as an upward arrow, and fits with our high normalization case but not with the low one.

Unfortunately, the two $z > 5.5$ galaxies of Dawson et al. (2001) cannot be used as a direct constraint to the luminosity function, since no continuum magnitude was given for either of the two. However, because their I_{AB} magnitudes are all fainter than 25, their result is at least not in conflict with our estimates above.

2.3.2 Indirect Result at the Bright End ($m_{AB} \sim 23$ mag)

Finding any $z \simeq 6$ galaxies at these bright levels would require a SDSS-like all-sky survey, but extending at least one magnitude deeper, which is a daunting, if not impossible, task with any existing facilities. However, we can get some information in this regime by using quasar host galaxies as the tracers of the entire galaxy population. To the extent that quasar hosts can be taken as representatives of galaxies, it is possible to obtain a reasonable, although indirect, bright-end lower limit if the hosts luminosity of the known $z \simeq 6$ quasars can be obtained. It has been long

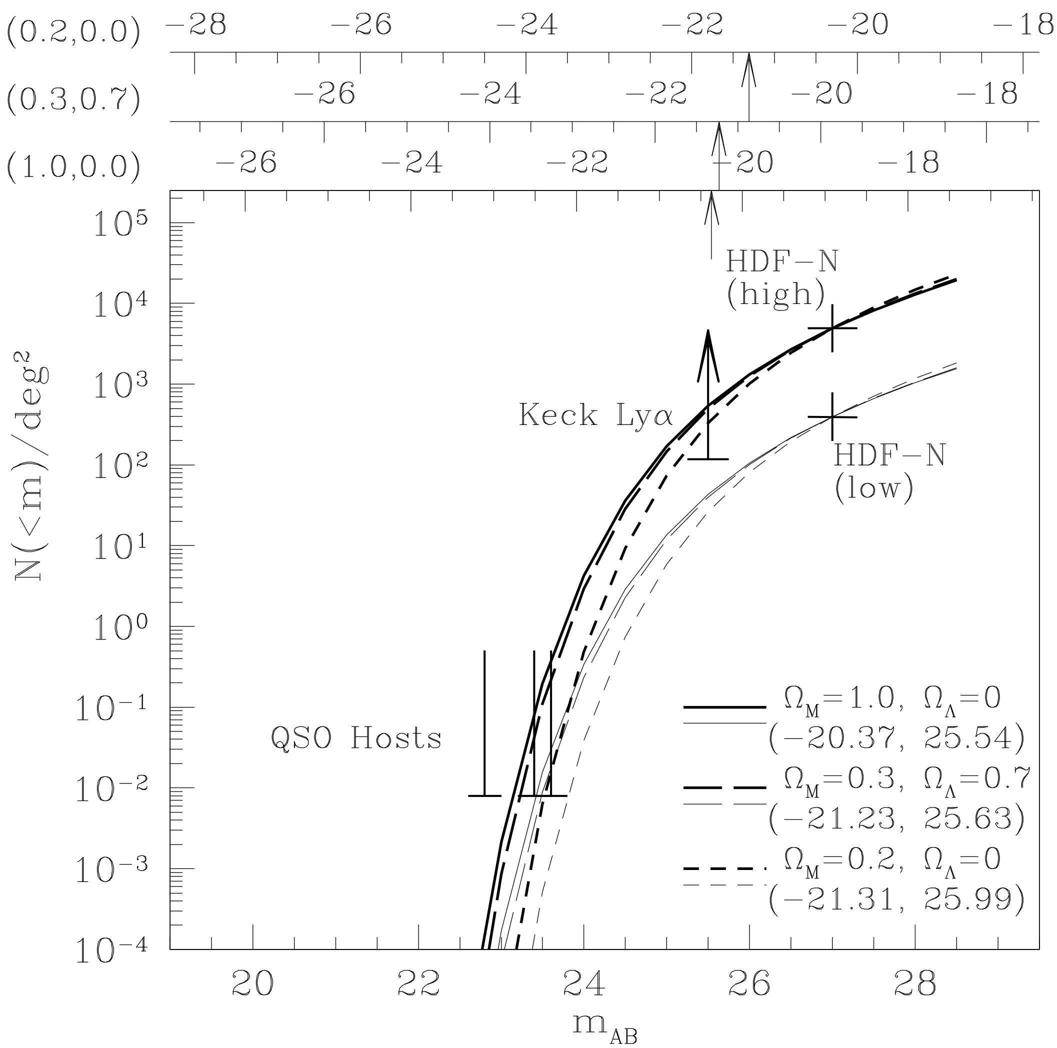

Figure 2.1: The cumulative surface density predictions of $z \simeq 6$ galaxies in the $5.5 \leq z \leq 6.5$ redshift bin, presented as the total number of galaxies per deg^2 whose brightness is brighter than a specified apparent magnitude (defined around 9100 − 9800Å in the AB system). The results for the (1, 0), (0.3, 0.7) and (0.2, 0) models are plotted in solid lines, long-dashed lines and short-dashed lines, respectively. The high and low normalization cases are plotted in thick and thin lines, respectively. The "+" labels mark the positions where the HDF-based normalizations are placed. The corresponding absolute magnitude scales are labeled on top of the figure, from bottom to the top for the (1, 0), (0.3, 0.7) and (0.2, 0) models. The M^* values in these three models are given in the legend together with the corresponding apparent magnitude scales, and are also marked with the upward arrows on the scales. The lower limit derived from Hu et al. (1999) is labeled by the thick upward arrow. The indirect bright-end upper-limit inferred from the hosts of the SDSS $5.5 \leq z \leq 6.5$ quasars is indicated by "⊥" from the left to right for (1, 0), (0.3, 0.7) and (0.2, 0) models, respectively.

Table 2.1: Number Density Prediction for Galaxies at $5.5 \leq z \leq 6.5$

		$(1.0,\ 0.0)^a$		$(0.3,\ 0.7)^a$		$(0.2,\ 0.0)^a$
m	M	Σ	M	Σ	M	Σ
22.00	−23.91	2.19e-14	−24.86	2.33e-15	−25.30	3.02e-20
22.50	−23.41	6.83e-10	−24.36	1.65e-10	−24.80	1.38e-13
23.00	−22.91	5.98e-07	−23.86	2.42e-07	−24.30	2.66e-09
23.50	−22.41	5.44e-05	−23.36	3.06e-05	−23.80	1.76e-06
24.00	−21.91	1.17e-03	−22.86	8.12e-04	−23.30	1.34e-04
24.50	−21.41	1.00e-02	−22.36	7.95e-03	−22.80	2.57e-03
25.00	−20.91	4.71e-02	−21.86	4.08e-02	−22.30	2.04e-02
25.50	−20.41	1.50e-01	−21.36	1.38e-01	−21.80	9.15e-02
26.00	−19.91	3.67e-01	−20.86	3.51e-01	−21.30	2.82e-01
26.50	−19.41	7.53e-01	−20.36	7.40e-01	−20.80	6.77e-01
27.00	−18.91	1.37e+00	−19.86	1.37e+00	−20.30	1.37e+00
27.50	−18.41	2.29e+00	−19.36	2.32e+00	−19.80	2.47e+00
28.00	−17.91	3.59e+00	−18.86	3.67e+00	−19.30	4.09e+00
28.50	−17.41	5.40e+00	−18.36	5.56e+00	−18.80	6.39e+00

		$(1.0,\ 0.0)^b$		$(0.3,\ 0.7)^b$		$(0.2,\ 0.0)^b$
m	M	Σ	M	Σ	M	Σ
22.00	−23.91	1.76e-15	−24.86	1.87e-16	−25.30	2.43e-21
22.50	−23.41	5.49e-11	−24.36	1.32e-11	−24.80	1.07e-14
23.00	−22.91	4.80e-08	−23.86	1.94e-08	−24.30	2.13e-10
23.50	−22.41	4.36e-06	−23.36	2.46e-06	−23.80	1.41e-07
24.00	−21.91	9.39e-05	−22.86	6.52e-05	−23.30	1.07e-05
24.50	−21.41	8.03e-04	−22.36	6.38e-04	−22.80	2.06e-04
25.00	−20.91	3.78e-03	−21.86	3.28e-03	−22.30	1.64e-03
25.50	−20.41	1.20e-02	−21.36	1.11e-02	−21.80	7.35e-03
26.00	−19.91	2.95e-02	−20.86	2.82e-02	−21.30	2.26e-02
26.50	−19.41	6.05e-02	−20.36	5.94e-02	−20.80	5.43e-02
27.00	−18.91	1.10e-01	−19.86	1.10e-01	−20.30	1.10e-01
27.50	−18.41	1.84e-01	−19.36	1.86e-01	−19.80	1.98e-01
28.00	−17.91	2.88e-01	−18.86	2.95e-01	−19.30	3.28e-01
28.50	−17.41	4.33e-01	−18.36	4.46e-01	−18.80	5.13e-01

a. High normalization case
b. Low normalization case

Predictions are given for $(\Omega_M, \Omega_\Lambda) = (1, 0)$, $(0.3, 0.7)$, and (0.2, 0) cosmologies. m is apparent magnitude and M is absolute magnitude in the corresponding cosmology model. Σ is cumulative number density in arcmin^{-2}, calculated for the entire $5.5 \leq z \leq 6.5$ bin.

suggested that there is a linear relation between the quasar luminosity and the *minimum* luminosity of its host galaxy (e.g. McLeod & Rieke 1995), which can be understood in the sense that a more luminous host galaxy is required to fuel a more luminous quasar. Thus there might be a similar relation between the luminosity of the quasar and that of its host at higher redshift. Such a relation would give a luminosity function constraint from the four $z > 5.5$ quasars known, all discovered by SDSS in ~ 1500 deg^2 of survey area (Fan et al. 2000b, 2001). We construct such a relation from Bahcall et al. (1996), who imaged twenty nearby ($z < 0.3$) luminous quasars with HST, and obtained their host luminosities. A simple fit to their data gives $M_{host} = 0.425 \times M_{qso} - 11.82$ ($rms = 0.38$ mag). Using this formula, we found that the host luminosities of the four $z > 5.5$ SDSS quasars were almost identical. Their average absolute magnitude at around rest-frame 1400Å is $M = -23.1$, -23.5 and -23.7 mag ($rms \sim 0.2$ mag) in the (1, 0), (0.3, 0.7) and (0.2, 0) universe, respectively, which correspond to apparent magnitudes of 22.8, 23.4 and 23.6 mag, respectively, at $z = 6$. The AGN unification scheme implies that if an AGN is detected, statistically there must be two or more galaxies which also harbor AGN activity, which cannot be detected because obscuring matter in the surrounding torus largely blocks our view. In other words, since there are four $z > 5.5$ quasars detected in ~ 1500 deg^2, the total number of $z > 5.5$ galaxies (including the four quasar hosts) is at least 12, implying a number density of $log(N) \geq 2.10$ deg^{-2} at the above mentioned brightness levels. As indicated above, this number should be taken as a lower limit, because there could be some galaxies as luminous as the quasar hosts, but lack a massive central black hole and thus cannot be traced by AGN. This indirect constraint is shown by the upward arrow in Figure 2.1.

There are two major uncertainties on this bright-end constraint. One is the effect of quasar luminosity evolution. The above linear relation between the hosts and the quasars is inferred from a local sample, yet we apply it to $z \simeq 6$. Typical quasar luminosities have been shown to evolve with redshift, as $(1 + z)^\beta$ with $\beta = 2.5$–4 for $z < 2.5$. This indicates that quasars may have once been brighter with respect to their hosts than we see today. In other words, the hosts of the $z \simeq 6$ quasars could be fainter than we estimated here, and therefore the limits shown in Figure 2.1 could be moved more to the right. However, since it is almost impossible to obtain a quantitative estimate about the amplitude of such a shift, we just leave the derived constraint as it is now. Another issue is whether quasar hosts are fair representatives of field galaxies, and therefore whether the above bright-end limit is meaningful. Bahcall et al. (1996) speculated that the quasar hosts might not fit a Schechter function and might be 2.2 mag more luminous than field galaxies. However, their suggestion was based on a volume-limited sample, which is clearly not the case for their luminous quasar sample. Furthermore, galaxy evolution clearly cannot be neglected in comparing results from $z \approx 0.2$ to $z \approx 6$. Net evolution of the hosts would move this constraint to higher luminosity, running counter to the effect of quasar luminosity evolution.

Even in the light of these caveats, we believe that the bright-end constraint indicated by the SDSS $z > 5.5$ quasars is useful. In fact, the (1, 0) model, either high or low normalization, and the low normalization case of the (0.2, 0) model, are clearly not consistent with this constraint. The high normalization case of both the (0.3, 0.7) and (0.2, 0) models, on the other hand, are perfectly consistent with this constraint. The low normalization case of the (0.3, 0.7) model is barely consistent with this constraint. Thus, the mere detection of four quasars at $z > 5.5$ implies a rather high normalization to the counts and luminosity function of galaxies at these redshifts.

2.4 Compared with Theoretical Models

We compare our estimates with the hierarchical N-body modeling results of Weinberg et al. (2002) in Figure 2.2. The thick solid line is our (0.3, 0.7) high normalization estimate. The thin lines of different types are the predictions of Weinberg et al. (2002), reproduced by reading off the numbers from their Figure 8 and following the converting procedures given by their paper. Only three of their models are reproduced here, namely, CCDM, LCDM and OCDM, which correspond

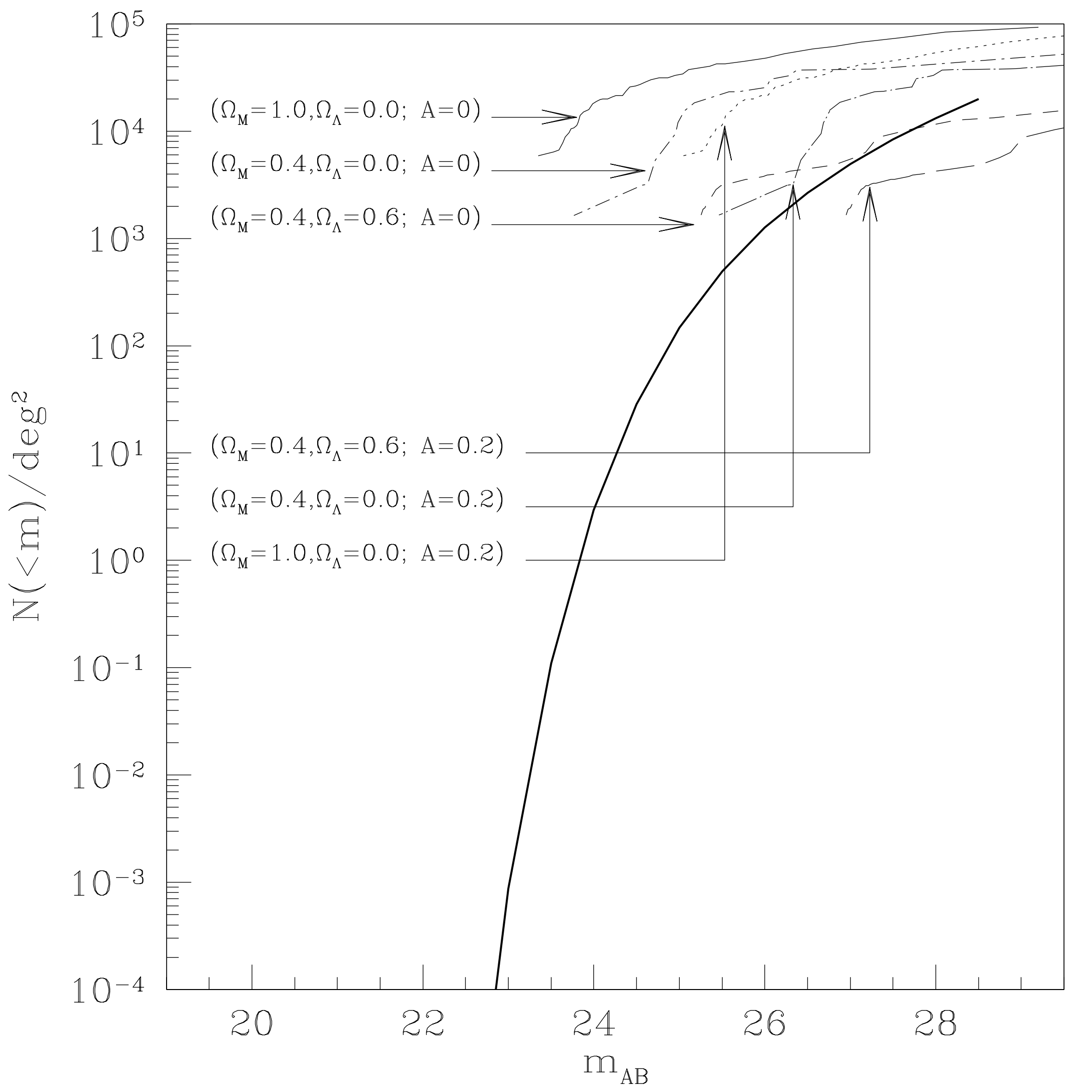

Figure 2.2: Comparing our estimates with the N-body simulation prediction of Weinberg et al. (2002). The high normalization case of our (0.3, 0.7) model is plotted as the thick solid line. The thin lines of different types are the predictions of Weinberg et al. (2002), reproduced by reading off the numbers from their Figure 8 and following the converting procedures given by their paper. Two flavors of these models are shown: one is without any dust extinction ($A = 0$ at around 1500 Å), and the other has a dust extinction of $A = 0.2\,mag$. Note how large the differences in the number count predictions are with only slight differences in the assumed dust extinction alone. Obviously only the (0.4, 0.6) model (LCDM) does not conflict with the HDF-N result.

to $(\Omega_M, \Omega_\Lambda) = (1, 0)$, $(0.4, 0.6)$ and $(0.4, 0)$, respectively. Their choices of Ω_M and Ω_Λ are slightly different from ours, but the effects of these on the global trends are only marginal. Two flavors of these models are shown: one is without any dust extinction ($A = 0$ at rest-frame 1500Å), and the other is with 20% dust extinction ($A = 0.2$ mag). Note that the count predictions can differ widely solely due to different assumptions about the internal extinction. Obviously only the (0.4, 0.6) model (LCDM) does not conflict with the HDF-N result as summarized in our Figure 2.2. Furthermore, nearly all those models predict unrealistically high surface density at $m_{AB} \leq 24.5$ mag, which is caused by the finite resolution in the simulations. Trading volume for finer resolution (Weinberg et al. 1999), their LCDM result would give a more realistic surface density at the bright end, but again would predict too high a value at the faint end.

It is also interesting to do a comparison among the theoretical predictions. For example, we can compare the result derived from Weinberg et al (2002) as shown in Figure 2 with the semi-analytic result of Robinson & Silk (2000) as shown in their Figure 3. A direct, quantitative comparison is not meaningful, since the result here is for $z = 6$ while the highest redshift given in Robinson & Silk's Figure 3 is $z = 5$, and their choices of Ω_M and Ω_Λ are slightly different. But we can still compare the global trends, which show obvious differences. In Robinson & Silk's semi-analytic formalism, the (1, 0) model gives the lowest galaxy counts, the (0.3, 0.7) lies in between, and the (0.2, 0) one gives the highest galaxy counts. They explained such trends as the result caused by the dominant effects of the different volume element dV/dz and the growth factor G in different cosmologies. A lower-density universe always has higher dV/dz and larger G, and the combination of these two factors dominates the competing effect of the larger luminosity distance which makes objects fainter in such a universe. On the other hand, Weinberg et al.'s (1, 0) model yields the highest counts, (0.4, 0.6) yields the lowest counts, and (0.4, 0) is in between. Notice that in our approach (1, 0) gives the highest counts, (0.3, 0.7) is in between, and (0.2, 0) gives the lowest counts. It is possible that the reasoning of Robinson & Silk (2000) might only be partially true, and that other effects which they did not consider might actually be important. For example, if the luminosity of L^* galaxies in a high-density universe is brighter than that can be produced from their current model, the number counts in different cosmologies might have a different behavior from that shown in their paper.

2.5 Discussion

2.5.1 The Effect of Luminosity Evolution

The most crucial assumption made in our prediction is that the luminosity evolution from $z \simeq 3$ to 6 is not significant, so that the value of L^* at around rest-frame 1400Å is still the same at $z \simeq 6$ as at $z \simeq 3$. However, there are several possibilities where this condition could break down. There are at least two major competing effects which are relevant. One possibility is that the merger/star-forming rate could be lower at $z \simeq 6$, and so would bring down the value of L^*. On the other hand, both dust extinction and metalicity could be lower at earlier epochs as well, which would make L^* brighter.

The time interval between $z = 3$ and $z = 6$ is about 1.28 Gyr in a $\Omega_M = 0.3$, $\Omega_\Lambda = 0.7$, and $H_0 = 65$ universe, and is likely only sufficient to allow one major merger (c.f. Makino & Hut 1997). Hence a higher merger rate alone would at most make L^* at $z \simeq 3$ twice as bright as at $z \simeq 6$. On the other hand, a higher merger rate would certainly make star formation rate higher, and this would further contribute to the luminosity. The later effect, however, has not yet been well quantified. As a very rough estimation, the higher star formation rate could contribute another factor of few in increasing L^* at $z \simeq 3$. Thus the overall effect of merger/star formation rate difference would make L^* at $z \simeq 3$ four to six times as bright as at $z \simeq 6$, or a difference of 1.5–2 mag.

The dust content and metalicity are likely to increase from $z \simeq 6$ to 3, and these would affect L^* in the opposite way. For example, one of the more reddened object in Steidel et al.'s sample, MS 1512-cB58, is quoted having $E(B-V) \simeq 0.3$ mag (Pettini et al. 2001). Assuming the extinction law of Calzetti et al. (2000), this number translates to $A_{1400\mathring{A}} \simeq 2.6$ mag. This means the galaxies at $z \simeq 6$ could get brighter by 2.6 mag at most, if dust extinction is largely absent at this redshift.

The metalicity of galaxies at large redshift is again very hard to quantify and seems to have a wide spread (e.g. Nagamine et al. 2001); but in any case, it is not likely that this effect would contribute more than 0.5 mag increase in brightness at $z \simeq 6$ at around rest-frame 1400 Å.

The above arguments, although crude, suggest that the two major luminosity evolutionary effects tend to cancel out each other, and the uncertainty brought by these effects in terms of L^* value is likely only to the order of $0.5 - 1.0$ mag. As the predicted counts at the brighter end ($m_{AB} \simeq 24$ mag) are very sensitive to the L^* value, surveys at this brightness level will be very useful in detecting the effect of possible luminosity evolution.

2.5.2 The Optimal Survey Strategy

To summarize, we present a simple empirical approach to predict the galaxy surface density at $z \simeq 6$, which *extrapolates* the known LF of $z \simeq 3$ galaxies to $z \simeq 6$. Our approach is based on only two observational results, namely, the observed luminosity function of $z \simeq 3$ Lyman-break galaxies and the number of $5.5 \leq z \leq 6.5$ galaxies in the HDF-N, and the assumption that there is no *strong* luminosity evolution for galaxies from $z \simeq 3$ to $z \simeq 6$. The biggest uncertainty in our estimates comes from the normalization, *i.e.*, the actual number density of $z \simeq 6$ galaxies in the HDF-N down to the limit of $m_{AB} = 27.0$ mag, for which we used one per WFPC-2 field and one per NIC-3 field as our low and high normalization, respectively. It seems that the low normalization case can be rejected, because it conflicts with the two observational constraints given in §2.3. The high normalization case, on the other hand, seems to be reasonable.

This simple prediction, while there is no other better alternative, can be used to plan future surveys, whose results can then be used to (iteratively if necessary) refine the predicted LF. As our prediction indicates, currently the most realistic way to find a significant number of $z \simeq 6$ galaxies with the available ground-based facilities is to do multi-color, medium-depth and wide-field surveys reaching continuum $m_{AB} \sim 24.0 - 24.5$ mag from 8400Å to the CCD Q.E. cut-off at around $1\mu m$, and covering a couple of square degrees. There are several wide-field CCD cameras available at telescopes of sufficient light-gathering power, e.g., the MOSAIC-I/II at the KPNO/CTIO 4m's, the CFH12K at the 3.6m CFHT and the Suprime-Cam at the 8m Subaru. Carefully designed surveys at a 4m class telescope could possibly discover a handful of $L > L^*$ $z \simeq 6$ galaxies within a few nights of observation. On the other hand, deep, pencil-beam surveys from the ground are not likely to be very successful even with 8-10m class telescopes. As Table 2.1 indicated, pencil-beam surveys with a few square arcmin field of view would have to reach at least $m_{AB} = 27$ mag in the difficult spectrum regime redder than 8400Å to discover a significant number of such objects. Since at least two bands of observation at similar depth are needed to select drop-out candidates, the telescope time required is very costly if not unrealistic. Accessing the faint end of the LF should better be done in the space where the sky background is orders of magnitude lower than that from the ground.

Therefore, this thesis work aims at constraining the LF of galaxies at $z \simeq 6$ by carrying out two surveys at two widely separated brightness levels: a wide-field one (~ 1 deg^2) to the depth of $m_{AB} \simeq 24$ mag using the KPNO/CTIO 4m's, and a pencil-beam one (~ 10 arcmin^2) to the depth of $m_{AB} \simeq 27$ mag using the Advanced Camera for Surveys (ACS) that has been on-board the Hubble Space Telescope (HST) since March 2002. For simplicity, from now on the former survey will be referred to as either the wide-field survey or the bright-end survey, and the latter survey will be referred to as either the deep survey or the faint-end survey.

PART II

BRIGHT-END CONSTRAINTS — NOAO 4m Survey

This part describes in details the wide-field survey that aimed at constraining the bright-end of the LF at $z \simeq 6$. Given our accessibility to available facilities, using the KPNO/CTIO 4m telescopes was the only choice. The $36' \times 36'$ arcmin^2 field-of-view (FOV) provided by the two MOSAIC cameras is suitable for a degree-sized survey. Each of the MOSAIC cameras consists of eight 2048×4096 SITe CCD chips that are thinned and anti-reflecting coated. At the f/3.1 focus of the 4m's, the $15\mu m$ pixel gives a spacial resolution of $0.26''$/pixel. The CCD chips are quite sensitive to the red light — their average Q.E. at 9000Å is slightly over 40% and at 9500Å is still about 25%.

CHAPTER 3

Survey Design

3.1 Search Method and Filter Selection

As outlined in Chapter 1, two selection methods are available in the optical regime, namely, the Lyman-break technique by using broad-band imaging that aims at the Lyman-break signature in the continuum, and the narrow-band imaging technique that aims at the Lyα emission line.

It was known to us that some other groups were doing or were planning to do wide-field broad-band surveys at 4m class and 8m class telescopes.[1] Although their purposes might not be specifically targeted at searching for $z \simeq 6$ galaxies, their spectral coverages and survey depths make their data suitable for such a search. For this reason, we chose to adopt an approach that is closer to the narrow-band imaging technique, and aimed largely at discovering strong Lyα emitters at $z \simeq 6$ that might be missed by broad-band surveys. An emission line of an observed equivalent width W can only contribute an additional W/D of the continuum flux level to the total flux enclosed by a filter of width D. In broad-band selections where D is normally of the order of 2000Å, a strong emission line of $W \simeq 200$Å would contribute an additional flux of only one-tenth of the continuum level and so would brighten the object by only 0.1 mag, which is almost negligible. In narrow-band imaging, where D is to the order of 100Å, on the other hand, the presence of such a line would brighten the object by 1.2 mag.

An intermediate-band filter set, known as the *BATC* filter set, was used in our bright-end survey. These filters, 15 in total, cover the entire $3000 - 10000$Å range, and are designed to avoid the brightest and most variable night-sky lines to yield dark background and fringe-free imaging. This set of filters are essentially the same as the ones used in the Beijing-Arizona-Taiwan-Connecticut

[1] One example is the NOAO Deep Wide-Field Survey (Jannuzi & Dey 1999).

Table 3.1: Parameters of the four reddest BATC filters

Filter	λ_{eff} (Å)	λ_b—λ_r (Å)	z-window for Lyα	z-window for LB
$m(802nm)$	8045.2	7962.7—8129.3	5.55—5.69	—
$n(848nm)$	8504.1	8441.0—8569.0	5.94—6.05	5.69–6.05
$o(919nm)$	9170.6	9075.7—9268.3	6.46—6.62	6.05–6.62
$p(974nm)$	9712.6	9612.9—9812.2	6.91—7.07	—

For a given filter, the redshift window of detecting Lyα line is different from that of detecting the Lyman-break. See text for detail.

(BATC) Survey (e.g, Fan et al. 1996; Shang et al. 1998; Zheng et al. 1999; Yan et al. 2000), but of a larger physical size (5.7-inch by 5.7-inch) that was specifically designed to be used at the NOAO MOSAIC I/II cameras. The reddest four of these filters, namely, $m(802nm)$, $n(848nm)$, $o(919nm)$ and $p(974nm)$, are ideal for the search of $5.5 \leq z \leq 7.0$ galaxies through detecting the redshifted Lyα emission line. While the average filter width of the entire filter set is about 300Å and thus falls in the intermediate-band category, the widths of these four reddest filters are around 150Å and are closer to narrow-band filters. We chose to use all these four filters, whose transmission curves are shown in Figure 3.1. Their parameters are listed in Table 3.1. Note that these parameters are slightly different from the parameters of the standard BATC system (Yan et al. 2000).

Figure 3.2 gives a visualization of how these intermediate-band filters can pick up a strong Lyα emission line in different redshift windows. The system response curves of these four passbands, obtained by convolving the filter transmissions and the CCD Q.E., are plotted as solid lines (the contributions from other components in the optics, such as the reflectivity of the primary mirror, are ignored because they are not a strong function of wavelength and thus do not affect the shape of the system response curve). For comparison, the response curves of the NOAO R and I bands are also plotted (dashed lines). The thick solid lines overplotted on the graphs are the model SED of a young galaxy at $z = 5.0$, 5.5 and 6.0, respectively, attenuated by the cosmic H I absorption (Madau 1995) at these redshifts. The rest-frame spectrum of this model galaxy was taken from Bruzual & Charlot (1993), and the Lyα emission line was manually added. Our intermediate-band survey and

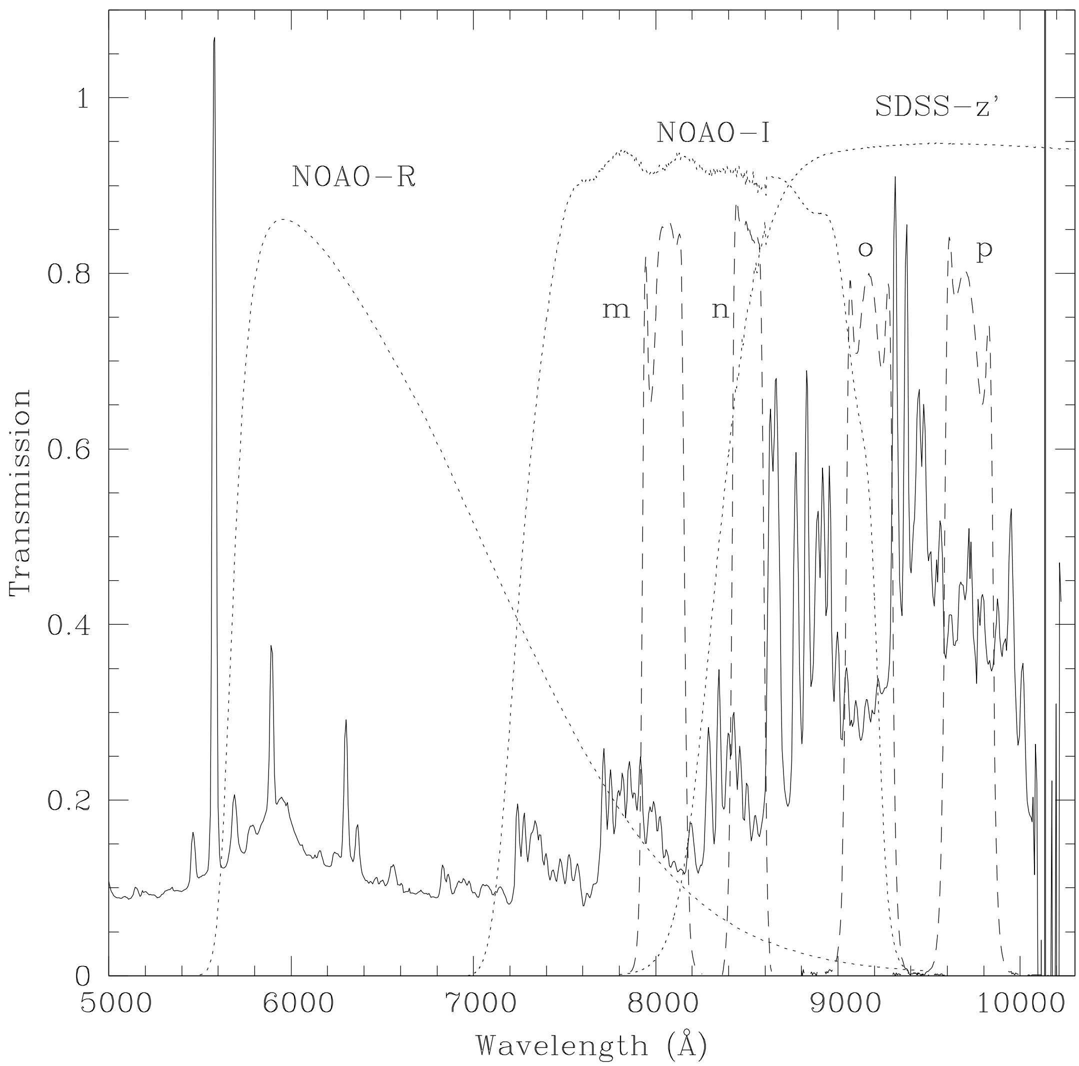

Figure 3.1: The transmissions of the four intermediate-band BATC filters used in the bright-end survey are plotted as dashed lines. The transmissions of the facility broad-band R, I and z' provided for MOSAIC are also shown as dotted lines for comparison. A typical Arizona night-sky spectrum is superimposed as solid line. Our filters avoid the strongest night lines, and extend beyond 9200Å where the broad-band NOAO-I filter has its cut-off. Besides the greatly reduced sky background in our passbands, our filters also have a great advantage that fringing caused by night-sky emission lines is heavily suppressed, eliminating the dominant noise source which limits the ablility of detecting objects at faint level.

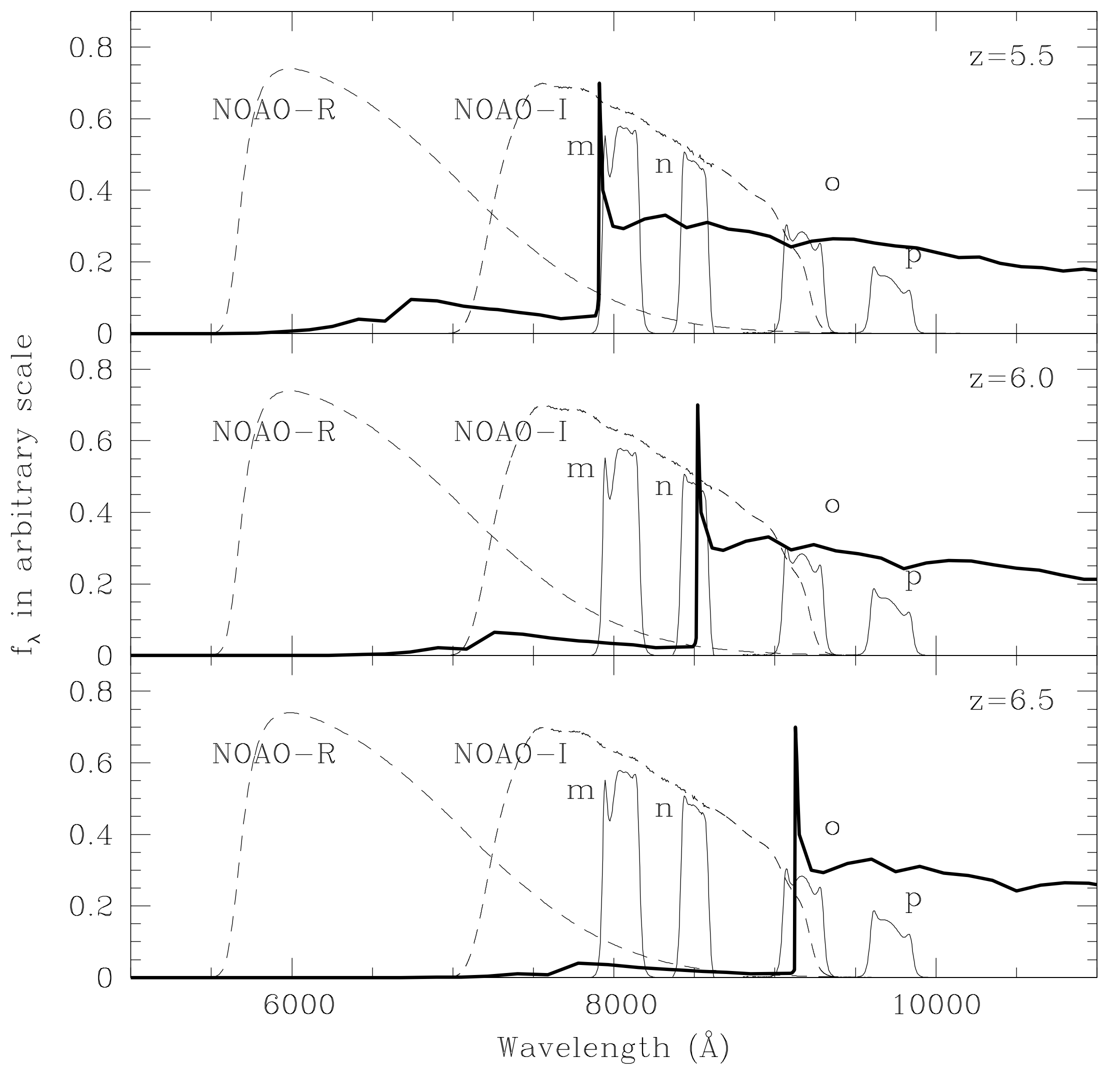

Figure 3.2: A visualization on how $5.5 \leq z \leq 6.5$ object selection can be done with the BATC filters. The case is demonstrated for three redshifts, $z = 5.5$, $z = 6.0$ and $z = 6.5$, from top to bottom, respectively. The system responses of these passbands, obtained by convolving the filter transmissions with the CCD Q.E. of the MOSAIC, are shown in thin solid line. For comparison, the responses of the facility R and I bands are also shown (in dashed line). The thick solid lines overplotted on the graphs are the model SED of a young galaxy (Bruzual & Charlot 1993) at the given redshifts, attenuated by intervening cosmic H I absorption (Madau 1995). The Lyα line was added to the SED. The $p(974nm)$ filter was also used to constrain the surface density of galaxies at $z \simeq 7$.

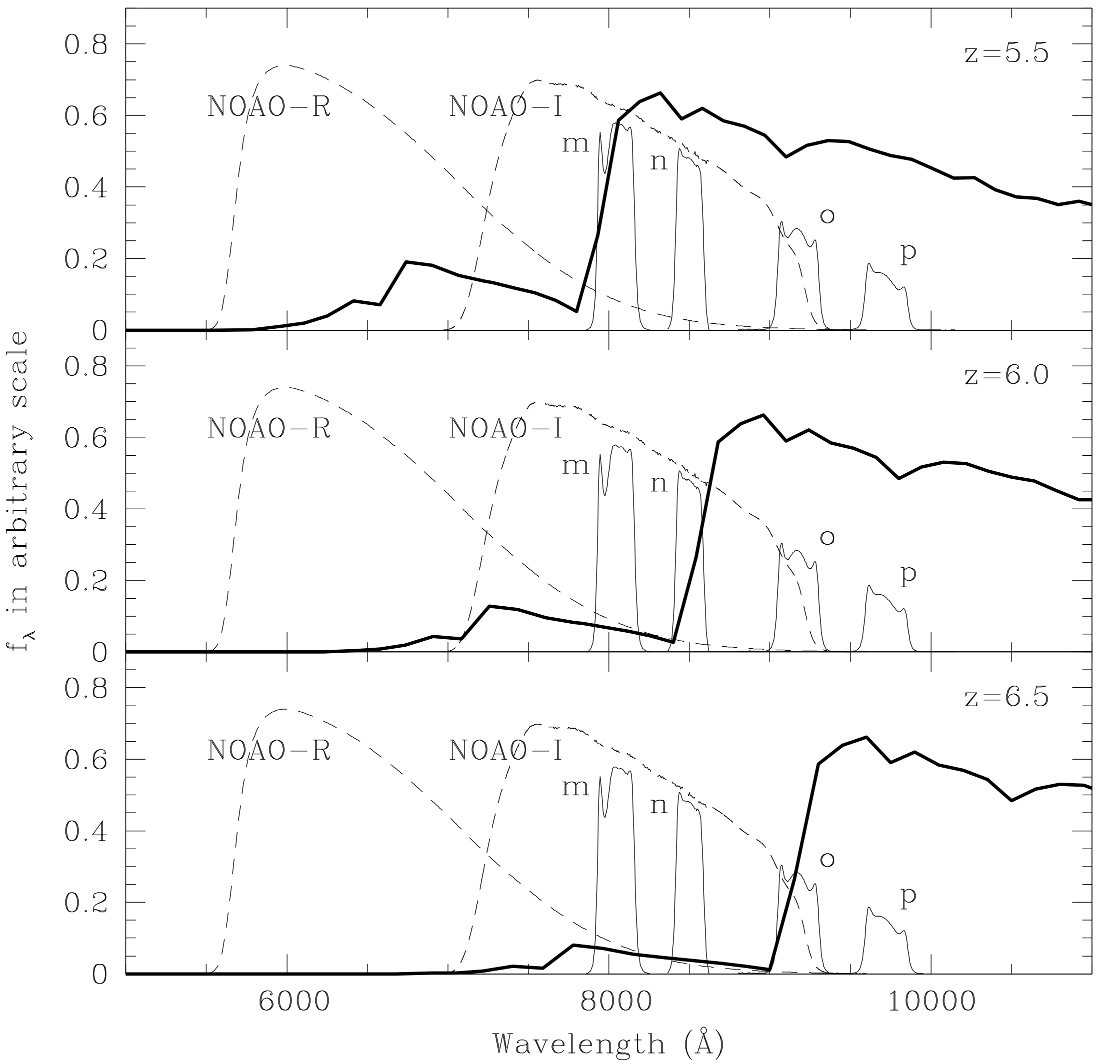

Figure 3.3: These BATC filters alone are also capable of detecting the Lyman-break signature at $z \simeq 6$. The legends are the same as in Figure 3.2, except that the SED of the model galaxy does not have the artificial Lyα line.

other on-going narrow-band surveys are complementary to each other, because our redshift windows are different from theirs (see Table 3.1). For example, the Large Area Lyman Alpha Survey (LALA Survey; Rhoads et al. 2000; Rhoads & Malhotra 2001; Rhoads et al. 2003) has one narrow window centered on $z = 5.7$. Thus using our results and those from other narrow-band surveys together can give a more comprehensive picture of the redshift distribution of galaxies at $z \simeq 6$.

Unlike conventional narrow-band surveys, we did not require continuum imaging through a broad-band filter. Instead, we applied the drop-out technique to this intermediate-band survey. For example, a valid candidate detected in the $o(919nm)$ band should not be seen in the $m(802nm)$ and $n(848nm)$ (i.e., drop-out from these two bands). Therefore, our search is capable of detecting the Lyman-break signature as well, provided that the search reaches sufficient depth.[2]. This feature, which other on-going narrow-band surveys do not have, is demonstrated in Figure 3.3. The legends are the same as those in Figure 3.2, except that the SED of the model galaxy does not have the Lyα line added.

It should be pointed out that the redshift windows that our filter set corresponds to are different for detecting the Lyα line and for detecting the Lyman-break. In the former case, a given passband is completely blind to the Lyα line if the line lies outside of the passband (i.e., the line lies in the gap between two adjacent filters), and thus its redshift window is set by z_{low} and z_{high}, where $z_{low} = \lambda_b/1216 - 1$ and $z_{high} = \lambda_r/1216 - 1$, and λ_b and λ_r are the blue and the red cut-off wavelengths of this passband, respectively. In the latter case, even if the Lyman-break lies to the blue side of a given passband, this band is still sensitive to the continuum redder than rest-frame 1216Å. Thus its corresponding redshift window is set by $z^{'}_{low}$ and z_{high}, where z_{high} is still the same as before, but $z^{'}_{low} = \lambda^{'}_r/1216 - 1$, and $\lambda^{'}_r$ is the red cut-off wavelength of the passband that is to the *blue* side of this given passband. Table 3.1 also lists all the redshift windows of these filters in the two different cases.

[2]A slight complication here is that the drop-out search in the $m(802nm)$ band cannot be done without the aid of a passband to its blue-side, although the search of emission-line object can still be carried out by using the $n(848nm)$ band as the continuum band.

3.2 Field Selection and Calibration Plan

To maximize the scientific return, we selected the survey fields around the HDF-North and South, which are among the most intensively studied areas on the sky. The designed spatial coverage is 1 deg^2, which can be covered by three MOSAIC pointings. Two pointings, designated as HDFN01 and HDFS01, were chosen to cover the HDF-North and South, and one other pointing, designated as HDFN02, was chosen to be right next to HDFN01 (to its south). The center of HDFS01 was not on any of the HST observations of the HDF-South; it was offset such that a few extremely bright stars did not fall within the FOV. The field center coordinates (J2000.0) are:

- HDFN01: $12^h36^m48^s$ $+62^o13^{'}26^{''}$
- HDFN02: $12^h36^m48^s$ $+61^o38^{'}14^{''}$
- HDFS01: $22^h32^m04^s$ $-60^o47^{'}23^{''}$

Although the selection of high-z candidates by using the drop-out method does not require flux calibration of the targets, such a calibration is needed if we are to derive any meaningful constraint to the LF. To make most out of the limited observing time at the 4m's, we decided to do the calibration observation on smaller telescopes. A clone set of the filters ($2' \times 2'$ in size) used in the BATC Survey was kindly loaned to us, courtesy of Prof. Wei-Hsin Sun at National Central University in Taiwan.

Using these BATC filters means that the final photometric results are in the BATC photometric system (Fan et al. 1996, Yan et al. 2000), which is very close to the AB system of Oke & Gunn (1983). The magnitude in the BATC system is related to the flux in the following way:

$$m_{batc} = -2.5 \cdot log\widetilde{F_\nu} - 48.60,$$

where $\widetilde{F_\nu}$ is the appropriately averaged monochromatic flux (measured in $erg \cdot s^{-1} \cdot cm^{-2} \cdot Hz^{-1}$) at the effective wavelength of the specific passband. For a photon-count detector such as a CCD, $\widetilde{F_\nu}$ can be more naturally written as

$$\widetilde{F_\nu} = \frac{\int d(log\nu) f_\nu R_\nu}{\int d(log\nu) R_\nu},$$

where R_ν is the overall system response. This formalism makes the magnitude tied to the numbers of photons detected by the CCD rather than to the input flux (Fukugita et al. 1996). This definition is equivalent to one in which the flux is weighted by wavelength within a specific passband, and is the convention adopted by the BATC Survey (see Yan et al. 2000). The system response $R(\lambda)$ actually used to relate f_ν and $\widetilde{F_\nu}$ includes *only* the filter transmissions. Other effects such as the quantum efficiency of the CCD, the response of the telescope's optics, etc., are ignored. This makes the BATC photometric system defined only by filter. We can do this because the bandwidths are intermediate in size and all the other responses are essentially flat within a specified passband.

CHAPTER 4

Observations

4.1 Survey Field Observations

4.1.1 CTIO 4m Observations

The observations of the HDFS01 field were done on June 5–7, 2000 at the CTIO 4m. The transparency was good throughout the run, but it turned out to be non-photometric. The seeing was $1''$–$1.3''$. This was a dark run.

The telescope time was not optimal for the observation of this field, as it was not up until the second half of the night. The field could be observed for no more than 15 hours in total. Considering the overheads (such as the time that had to be spent on CCD read-out, telescope offset, etc.), the available time was less. To ensure that sufficient depths could be reached, we decided to skip the $m(802nm)$ filter and to observe only the three reddest filters. This decision kept the redshift windows at $z \simeq 6.0$, 6.5 and 7.0, but dropped the window at $z \simeq 5.5$.

For each of the three filters, seven to nine 0.5-hour exposures were taken with $0.5' - 1'$ of positional offsets (known as "dithering"). In total, both the $n(848nm)$ and the $o(919nm)$ bands were observed for 3.5 hours, while the $p(974nm)$ band was observed for 5 hours. All these observations were done in dark hours after the moonset.

At the time of the observation, it was not known if the calibration plan could be successfully carried out. Therefore, a minimum amount of calibration observation was also done during the run. Three fields that have BATC secondary standard stars[1], SA104, SA107 and SA113, were observed for at least once (but not through every filter).

[1]These secondary stars have not yet been published by the time when this thesis was written; however it was known to the author that the observations on these fields had been done long time ago by the BATC Survey under photometric condition for at least once through each of these filters.

4.1.2 KPNO 4m Observations

Five nights were awarded to observe the HDFN fields in the 2002A semester at the KPNO 4m. The observations were done on March 20 – 24, 2002. The night of March 21 was largely lost due to the bad weather and only three hours of useful data were obtained. The transparency of the other four nights was good, however none of these four nights was photometric. The seeing was at around $1.2''$–$1.5''$ and was larger than usual. This run was a grey–bright run, and most of the images were obtained during bright hours with larger than quarter moon on the sky. The moon, when it was up, was 50^o–70^o away from the target fields.

The original plan was to observe both the HDFN01 and HDFN02 fields in all the four reddest filters, with six hours of exposure in the $p(974nm)$ band and four hours each in the other three bands. A change had to be made, however, due to the loss of time in the second night, and it was decided to skip the $p(974nm)$ observation of the HDFN02 field. All the other observations were carried out as planned. With only a few exceptions due to instrumentation glitches, each of the exposures was 0.5-hour and they were taken with $0.5'$–$1'$ of dithering. Unfortunately, a few images were later found unusable (see the reduction part below) and had to be discarded. The total of the useful deep exposure time was about 27.5 hours.

For quality control purpose, a few images in the $i(606nm)$ filter, the widest filter in the BATC system, were also taken throughout the run for both fields. The total time spent on this filter is less than two hours.

The associated calibration observations in the BATC photometric system were finished in 2001 (see below) and several comparison stars have been set up in the HDFN01 field. Thus no calibration observation was done during this KPNO 4m run. However, the HDFN02 field did not have comparison star. Therefore, a field, called "HDFN-tran", that covers half of the HDFN01 and half of the HDFN02 was also taken in all the filters with 5-minute of exposure each. With these observations, the calibration of the HDFN02 field can be tied to the comparison stars in the HDFN01 field. As

Table 4.1: The details of the long-exposure observations at the KPNO 4m

HDFN01	Date	Dithering	Total Exp. (hours)
$m(802nm)$	3/21-22	8×0.5hr	4.00
$n(848nm)$	3/23-24	4×0.5hr+1412sec+1217sec	2.73
$o(919nm)$	3/23-24	8×0.5hr[a]	3.00
$p(974nm)$	3/21-22; 3/22-23	6×0.5hr+10×0.5hr[b]	6.24

HDFN02	Date	Dithering	Total Exp. (hours)
$m(802nm)$	3/25-26	7×0.5hr[c]+728sec	2.70
$n(848nm)$	3/24-25; 3/25-26	1×0.5hr[d]+7×0.5hr	3.50
$o(919nm)$	3/24-25	8×0.5hr	4.00
$p(974nm)$	—	—	—

a. Two 0.5-hr exposures were discarded.
b. Four 0.5-hr exposures were discarded.
c. Two 0.5-hr exposures were discarded.
d. One 0.5-hr exposures were discarded.

the calibration was done at a 61″ telescope, there was a risk that stars of sufficient S/N in the calibration images might be saturated in the 0.5-hour individual exposure at the 4m. To be safe, a single 5-minute exposure was taken for both the HDFN01 and HDFN02 fields in all the used filters.

Table 4.1 gives the details of the long-exposure observations for these two fields.

4.2 Calibration Observations

The calibration of the HDFN01 field was done during a one-year campaign at the 61″ Kuiper telescope of the Steward Observatory at Mt. Bigelow in AZ. The goal of this campaign was to set up BATC photometric system comparison stars in several fields of high public interest, and the HDF-North field was one of them. The details of this program will be described elsewhere (Yan et al. 2003, in preparation), and only the observations related to the HDFN field are summarized here.

The 2048×2048 CCD camera of the 61″ Kuiper telescope mounted at its f/13.5 Cassegrain focus gives a FOV of 5.1′×5.1′. A field centered on the HDF-North, designated as HDFN-cal, was observed on May 21 and 25, 2001 through the BATC Survey clone filter set. As the HDF-North itself is devoid of bright stars (as it was deliberately chosen to be so), a second field, designated as HDFN-cal3, was chosen at about $5'$ away from it and was observed through the same set of filters on Dec 18 and 21, 2001. There was a huge system change in August, 2001 when the original CCD chip, a thinned, back-illuminated chip known as "ccd24", was dead. It was replaced by a thick, front-illuminated chip in mid-November, 2001. This change did not have significant impact to the program, however, as the BATC photometric system is largely filter-defined (Yan et al. 2000).

All-sky photometry was carried out in both runs. The primary standard stars of the BATC Survey (Fan et al. 1996; Yan et al. 2000) were intensively observed throughout each night to sufficiently sample the airmass range from 1.0 to 2.2 and the hour angles range from -5 hours to $+5$ hours. To closely monitor any slight time-dependent extinction variation, the standard stars were observed at least once every hour even when they were at airmasses close to 1.0 where there was little change in airmass in three hours. The target fields, on the other hand, were always observed at airmasses less than 1.5. The HDFN-cal field was observed four times in total, while the HDFN-cal3 field was observed twice in total.

The calibration of the HDF-South field was done at the CTIO 0.9m telescope with the same filter set as used in the Mt. Bigelow calibration campaign. This project was awarded three nights in the 2001B semester, the last semester when the 0.9m telescope was operated by the CTIO. The observations were done on September 8–10, 2001.

The SITe 2048×2048 CCD camera at the f/13.5 Cassegrain focus of the 0.9m offers a $13.5' \times 13.5'$ FOV. Our 2-inch square filters are smaller than the 3-inch square filter slot, and filter adapters had to be used. The resulting images were vignetted, and the effective FOV was about $10' \times 10'$.

All-sky photometry was carried out throughout the run. The four primary standard stars of the BATC Survey are all in the northern sky and are not accessible from CTIO. The observing mode was the same as that of the Mt. Bigelow calibration observation: the standard stars were observed frequently at different airmasses, and the target fields [2] were observed at airmasses less than 1.4.

[2] Besides the HDF-South field, several other field of high public interests, such as the Chandra Deep Field South (CDF-S), were also calibrated in this run.

Table 4.2: The number of calibration observations done in 2001

	HDFN-cal 5/21-22	HDFN-cal 5/25-26	HDFN-cal3 12/18-19	HDFN-cal3 12/21-22	HDFS 9/7-8	HDFS 9/8-9
$m(802nm)$	1	3	1	1	3	—
$n(848nm)$	1	3	1	1	3	—
$o(919nm)$	1	3	1	1	3	—
$p(974nm)$	1	3	1	1	3	4

The standard stars used in this run were the secondary standards of the BATC Survey, which have been calibrated and tied to the primary standards. Theses stars are in the following three SA fields: SA92, SA107 and SA113. To ensure accurate calibration, two of the standard star fields, SA92 and SA113, were observed again in the 2001 December run (December 18 and 21) of the Mt. Bigelow calibration campaign for at least twice.

The calibration observations of the survey fields are summarized in Table 4.2.

CHAPTER 5

Data Reduction

5.1 Survey Data Reduction

5.1.1 Overview

The raw data produced by the NOAO MOSAIC cameras are in the multi-extension FITS (MEF) format. A raw image consists of nine FITS extensions, with the first extension (0^{th} extension) recording the primary header information and the remaining eight extensions (1^{st}–8^{st}) recording the imaging data produced by each of the eight CCD chips. The 0^{th} extension is essentially only a FITS header, while the other eight extensions are single FITS images that have both headers and pixel files. The data structure is described in details by Valdes & Tody (1998).

Conventionally, a reduction scheme of CCD imaging data consists of the following general steps: overscan subtraction and trimming, zero subtraction [1], dark-current subtraction, bad pixel fixing, dome-flat-fielding, fringing pattern removal (if the fringing is severe), and illumination correction (or called "sky-flat-fielding"; this is only needed if the dome-flat-fielding does not achieve satisfactory results). A lot of these steps are the same in the MOSAIC data reduction and the only major difference is that these steps need to be run on all the eight data extensions. However, there are also some distinctly differences in the MOSAIC data reduction.

The biggest one is that the images from each of the individual CCD chips eventually should be put onto a common astrometric grid and produce one large mosaic-ed image in the single-extension FITS format at some point of the reduction. This step is necessary for data obtained at any multi-chip CCD camera, and is a vital step if a number of dithered images are to be combined into a deeper image. Although there is an alternative that each data extension of the raw MEF images

[1] This step is also called "bias subtraction"; however this terminology is sometimes confusing and is not used here.

in a dithered series can be extracted as images in the single-FITS format and then processed and combined in the usual way, such an alternative is much less efficient and has the drawback of wasting a significant fraction of the border area around each chips. One other additional step in the MOSAIC data reduction is that the MOSAIC data have the image of the 4m telescope pupil superposed and this pupil image needs to be removed.

Frank Valdes at NOAO (Tucson) developed a MOSAIC data reduction package called the MSCRED (Valdes 1998), which was used to reduce all our survey data. This package consists of a suite of tasks that were specifically written for the data obtained with the MOSAIC I & II cameras, but can also be used to reduce other data that are in the standard MEF format. It was released as an external package of the Image Reduction and Analysis Facility (IRAF[2]), which has distributions for a large variety of platforms. Most of the reduction described here was done with the PC IRAF distribution that works under the RedHat LINUX operating system.

The reduction of the CTIO 4m data was finished by the end of June, 2000. At that time, the version of MSCRED was V3.2.3, which worked under PC IRAF V2.11.3. The KPNO 4m data were reduced with MSCRED V4.7 (released in May 2002), which is the latest version that works under the latest version of PC IRAF (V2.12.1). While this latest MSCRED release was added a lot of auxiliary tasks that can significantly facilitate the reduction process, its basic function is still the same as that of the older version. Therefore, no attempt has been made to reduce the CTIO data again with the new MSCRED release.

While there are indeed some notable differences, the reduction procedures that will be described below make nearly no distinction between the reduction of the KPNO data and that of the CTIO data. There are a few exceptions, however, when such differences could possibly slightly improve the quality of the CTIO data if they were to be reduced again; these cases will be explicitly noted.

[2]IRAF is distributed by the National Optical Astronomy Observatories, which are operated by the Association of Universities for Research in Astronomy, Inc., under cooperative agreement with the National Science Foundation.

5.1.2 Procedures

Below is a full account of what have been done in the reduction process. The steps that are the same to the conventional procedures will not be detailed, and only the steps that are unique to the MOSAIC data will be fully described.

Stage 1: Before Pupil-removing The reduction of this stage consists of cross-talk correction, overscan subtraction, fixing bad pixels, zero subtraction, and dome-flat-fielding. All these operations were trivially done by using the task CCDPROC.

One unique step in this stage is the cross-talk correction, which is necessary for the MOSAIC data because the multi-amplifiers have some slight cross-talking behavior (see the manual of the MOSAIC cameras for detail).

The dark current subtraction was omitted in the reduction for two reasons. First of all, the dark current of both MOSAIC cameras is only $\sim 5e^{-}$/pixel/hour. At the gain of $\sim 3e^{-}$/ADU, it is at a level of 1.67 ADU for a one-hour integration, clearly negligible compared to the sky, which was a couple of thousand ADU per hour. Secondly, the dark current can only be measured after the zero subtraction is done on the raw dark current images. It was found that the zero level was comparable to the level of an half-hour dark current, and it was slightly varying throughout both runs [3]. After subtracting the averaged zero image from the dark images, inconsistent measurements were obtained — sometimes the measurements were even negative. This indicated that the dark current correction was meaningless in our case, where the variation of the zero level could not be precisely monitored. However, omitting this step had negligible impact to the final data product.

The dome-flat-fielding part is somehow complicated. The dome-flat exposures, like the target exposures, also have the pupil image superposed. Although the general pattern of the pupil image is fixed, its fine structure is filter dependent. As the pupil image is an additive component that

[3] Varying zero level is hardly anything new, although to my best knowledge this topic has never been formally discussed in the literature and the course of such variation is not clearly known. For example, this phenomenon was well known in the BATC Survey.

has nothing to do with the intrinsic Q.E. of CCD pixels, it should first be removed from the dome-flats before they can be divided into the target images. The task MSCPUPIL was used to do this. Individual dome-flats were first combined into master dome-flats, one for each filter (in both runs only one group of dome-flats, eight frames in each group, were obtained for each filter). The pupil images were removed by setting the "type" parameter of the task MSCPUPIL to "residual". The resulting outputs then were used by the task CCDPROC.

Stage 2: Object Detecting and Masking As the MOSAIC cameras have a large FOV, and the 4m telescopes have open structures (i.e., do not have sealed telescope tubes), it is certain that the dome-flat-fielding will introduce illumination patterns into the target images, and thus an illumination correction at a later stage is necessary. An illumination correction image, usually loosely referred to as a "sky-flat", is constructed by combining a series of dithered target images. The celestial objects in the dithered target frames can be rejected by applying some clipping schemes. However, no matter which clipping algorithm to be used, it is always extremely difficult to completely eliminate the effect of very bright objects, such as saturated stars. A better way is to identify all the sources in the target frames and create source masks accordingly. These masks will then be used during combining, and the masked regions are not used as the inputs.

The task OBJMASKS was used in this step. Note that this task is not in the MSCRED package, but in the NPROTO, a special package of IRAF where the experimental tasks are put. Also note that before running this task, some associated parameters need to be set by invoking another task OBJMASKS1, which is also in the NPROTO package but is not listed.

If the object masks were only used for preparing sky-flats, this step could be postponed to a later time. However, the target frames also need to have the pupil image removed and this cannot be achieved by using the pupil images based on dome-flats. Instead, the removal of the pupil image from the target frames has to use a series of dithered target frames (see Stage 3 below). In this case the object masks are also needed. Thus it is necessary to go through this step right after the first stage. Note that both OBJMASKS and OBJMASKS1 are new tasks that are not available in earlier versions of IRAF. The object detecting and masking in the CTIO data reduction were done manually in a painstaking way. This is one of the places where the quality of the CTIO data could possibly be improved if they were to be reprocessed.

Stage 3: Pupil Removal In principle, a pupil template can be obtained by using the dome-flats if the parameter "type" of MSCPUPIL is set to "data". After proper scaling, the resulting pupil template can then be used by the task RMPUPIL to remove the pupil images from the target frames. However, it was found that this approach did not give satisfactory results. The fine structure and the precise position of the pupil image depend not only on the passbands, but also on the telescope pointings and sometimes even on the background brightness. Also, while the positional dependence was not strong, it was not repeatable. This is particularly true for the KPNO data.

After intensive testing, it was realized that the best results could only be achieved by using the target frames to derive the pupil templates. The templates should be derived not only for different passbands, but also for different telescope pointings. The latter consideration is not as daunting as it first looks, because each night the telescope was pointed to only one or two general directions.

The steps are the following. A group of dithered target images were combined without registering. The object masks obtained in Stage 2 were used. For some reasons, the combined image usually has a lot of pixels that have no actual data value and are assigned a value of "1". The precise reasons are not known, but it seems to be caused by the imperfect object masks. If the object masks (derived at Stage 2) mask out not only the real objects but also some fixed features on the CCD chips, the same pixels in every frame on the location of these fixed features will all be rejected and there is no pixel going into the combining. These no-value pixels cause problem in deriving the pupil template and should be fixed first.

Since they are all assigned a value of "1", these pixels were easily identified by using the MSKEXPR task in the PROTO package. Only CCD chip 2, 3, 6, and 7 (extension 2, 3, 6, and 7) need to go through this step, because the pupil image occupies only these four chips. The MSKEXPR task generates a bad-pixel-mask (BPM) based on the given expression that identifies the no-value pixels. It was run for four times and derived four BPM's, one for each extension. These BPM's were used by the task FIXPIX (also in the PROTO package) to fix the no-value pixels of the four chips, one chip at a time. Note that the keyword BPM should be added to the FITS header of each extension (using the HEDIT task) before FIXPIX can be used.

MSCPUPIL was then run on the combined image, with "type" set to "data", to get the pupil template. Before the pupil removal, however, there is one more extra, though quick, step. A pupil mask needs to be derived from the pupil template. This pupil mask is to let the next step know the general location of the pupil image. It was obtained by running MSCPUPIL on the pupil template just derived, with "type" set to "mask".

The task RMPUPIL was then used to remove the pupil image from the target frames. This task fits the pupil template to the region on a target frame marked by the pupil mask, and calculates an optimal scaling factor. After applying this scaling to the template, a model pupil image is obtained. This pupil model is then subtracted from the target frame. Although this process is complicated, it is now (in MSCRED V4.2) completely transparent to the user.

Note that the CTIO data reduction was slightly different from the procedures outlined above. At that time, the objects in the pupil image region were manually identified (looking at the screen display) and were removed interactively by using the task IMEDIT (in the TV package). This step was done for all the target images that were used to derive the pupil templates, and was done on an extension-by-extension basis. And the removal of the pupil image was also done by interactively running RMPUPIL. The old version of this task could not properly calculate the scale and the removal had to be slowly done by trial-and-error.

Stage 4: Fringing Removal Since the intermediate-band filters used in this survey are devoid of the strongest night-sky emission lines, the fringe amplitude was not as strong as one would see with broad-band filters. In the CTIO data, fringing was essentially absent from the $n(848nm)$ images and was very weak in the $o(919nm)$ images. Only the $p(945nm)$ images have prominent fringing patterns. As a comparison, the fringing in the KPNO data was stronger in general. It was weak in the $m(802nm)$ and the $n(848nm)$ bands, but was notably stronger in both the $o(919nm)$ and the $p(974nm)$ bands.

As the fringing is an additive component, its removal should be done by subtraction. Generally speaking, a fringing template can be derived from a series of dithered target frames. This template can then be scaled to individual target frames and subtracted.

This de-fringe process was done for the KPNO data on a filter-by-filter and night-by-night basis. A series of dithered target images were combined without registering, and the object masks derived in Stage 2 were used again. As in the case of creating pupil templates, the no-value pixels were identified with MSKEXPR and fixed by FIXPIX (for all the eight data extensions). The resulting image was median-filtered by the task MSCMEDIAN, with a median filter of the size 129×129, to get a highly smoothed substrate. The fringing template was obtained by subtracting this smooth substrate from the combined image, using the task MSCARITH. This template was then fed to the task RMFRINGE to remove the fringing patterns from the target frames.

While the fringing patterns are largely fixed for a given passband, it was found that their amplitudes at different positions varied with respect to each other over time. For this reason, the fringe template derived based on the combined target frames only represented the averaged fringing pattern during the time span when the series individual target images were taken, but could not accurately represent the fringing pattern in real time for each of the individual target images. As a result, the fringe removal was not perfect. Nevertheless, the error introduced in this step is likely small, given the already small amplitude of the fringing patterns in our intermediate-band data. It was also found that this step made only marginal differences to the $m(802nm)$ and the $n(848nm)$ images.

Note that in the CTIO data reduction this step was skipped completely. The first reason was because at that time the two essential tasks, MSCMEDIAN and RMFRINGE, were not available. The second reason was because the CTIO data showed rather weak fringing to begin with. Although mathematically the fringe removal should be done by subtraction rather than division, when this additive component is small enough as compared to the background it can be largely removed by division. Thus this step was incorporated into the sky-flat-fielding step (see Stage 5 below) for the CTIO data. The result was not bad: even in the $p(974nm)$ images the fringe pattern was largely gone.

Stage 5: Sky-flat-fielding After the removal of the pupil images and the fringing patterns, the target frames can be used to construct sky-flats. Again, the object masks derived in Stage 2 were used, and the no-value pixels were identified and fixed. The sky-flats were displayed and examined visually. Any residuals from celestial objects, such as the halos of saturated stars, were manually edited by using IMEDIT on an extension-by-extension basis.

After the sky-flats were ready, they were fed to the task CCDPROC to perform the illumination correction for the target frames.

Stage 6: Creating single-FITS mosaics The target images processed so far were ready to be put onto a common astrometric grid. Although the relative astrometry recorded in the FITS header is sufficient for this purpose alone, it is better to get the absolute astrometric zeropoints right at the beginning.

Both the CTIO and KPNO data were tied to the USNO A2.0 astrometry. The task MSCCMATCH was used to perform the astrometric zeropoint calibration. For the CTIO data, the USNO A2.0 catalog around the rough target field positions were fetched manually, and the task MSCZERO was used interactively to provide a first guess of the plate solution. The MSCCMATCH task in MSCRED V4.2 has the function to fetch the USNO A2.0 catalog automatically over the Internet, and the function of the MSCZERO task has been integrated into it. This improvement greatly reduced the workload of reducing the KPNO data. However, MSCCMATCH still needs to be run interactively to get rid of deviant points to obtain satisfactory astrometry. For all the images, the final fitting rms values are about $0.2''$–$0.3''$, or about one physical pixel, in both the RA and the DEC directions.

The task MSCIMAGE was used to create single-FITS mosaics. The interpolation function was set to "sinc17" and the fitting geometry was set to "general". Note that the "fluxcon" parameter should be set to "no" (see the manual of MSCIMAGE). Also, very importantly, the reference image should be the same for all the target images of a same field regardless of passband. This is because the actual output coordinate grid is defined by the reference image, and if the reference images are different, the single-FITS mosaics created will have their coordinate grids different in either the scale or the orientation. Such differences can make the final stacking or matched-aperture photometry impossible. This point has been explained in the manual of MSCIMAGE and will not be repeated here. For both the CTIO and the KPNO data, the reference images were chosen to be the first $n(848nm)$ images of each pointing.

Stage 7: Before Stacking The reduction procedures outlined above, especially the sky-flat-fielding part, were not perfect, and inevitably the target images still have some large scale background gradients. If such gradiances were allowed to go into the stacking process, it would be difficult to properly derive scaling factors that are needed for the stacking. Therefore, the task MSCSKYSUB was run on the target images to remove such gradients. The fitting function was chosen as a second-order Legendre function in both x and y directions (thus a plane-fitting was performed). The parameter "type_out" was set to "residual". Note that the MSCSKYSUB task in MSCRED V4.2 only subtracts the gradients, and its older version subtracted the entire background.

The last step before stacking was to calculate the scaling factor and the background offset factor for each of the dithered target images. The target images were taken at different background illumination conditions (such as different lunar phases), and this affected the background offset factor. Furthermore, the observations were done at different airmasses and different transparency conditions, and these affected the scaling factor. The task MSCIMATCH was used to derive both factors (see the manual of this task for its methodology). The results were recorded into the FITS headers, with the keywords "mscscale" for the scaling factor and "msczero" for the background offset factor.

Stage 8: Final Stacking After going through all these processes, the target images are ready for the final stacking. Although this can be done with other conventional combining tasks, there is a task in the MSCRED package, MSCSTACK, to perform this step. All the data in our survey were stacked by using this task. The type of combine operation was "average", and the rejecting algorithm was set to "ccdclip". Although the noise of the target frames at this stage was no longer simply the read-out noise because of noise propagation, this algorithm was still found to give the best result. The lower sigma clipping factor was set to 5, while the upper sigma clipping factor was set to 3. The neighbor rejection switch was turned off by setting the "grow" parameter to 0.

The MOSAIC survey data reduction was done at this point. For illustration purpose, Figure 5.1 and Figure 5.2 compare a raw image of the HDFN01 field taken in the $m(802nm)$ band, and the final stack of this band.

5.2 Calibration Data Reduction

The CCD cameras at the Steward Observatory 61$''$ telescope and the CTIO 0.9m telescope are single-chip cameras, and the data reduction were rather straightforward. All those data were reduced within one month after the observations.

The only complication was that the data taken at the CTIO 0.9m were read out by four amplifiers simultaneously (i.e., its QUAD mode). The software package specifically developed for reducing the multi-amplifier data at the CTIO was called QUAD, which is now integrated into the standard IRAF release and is renamed as QUADRED. In September 2001 when the CTIO 0.9m data were reduced,

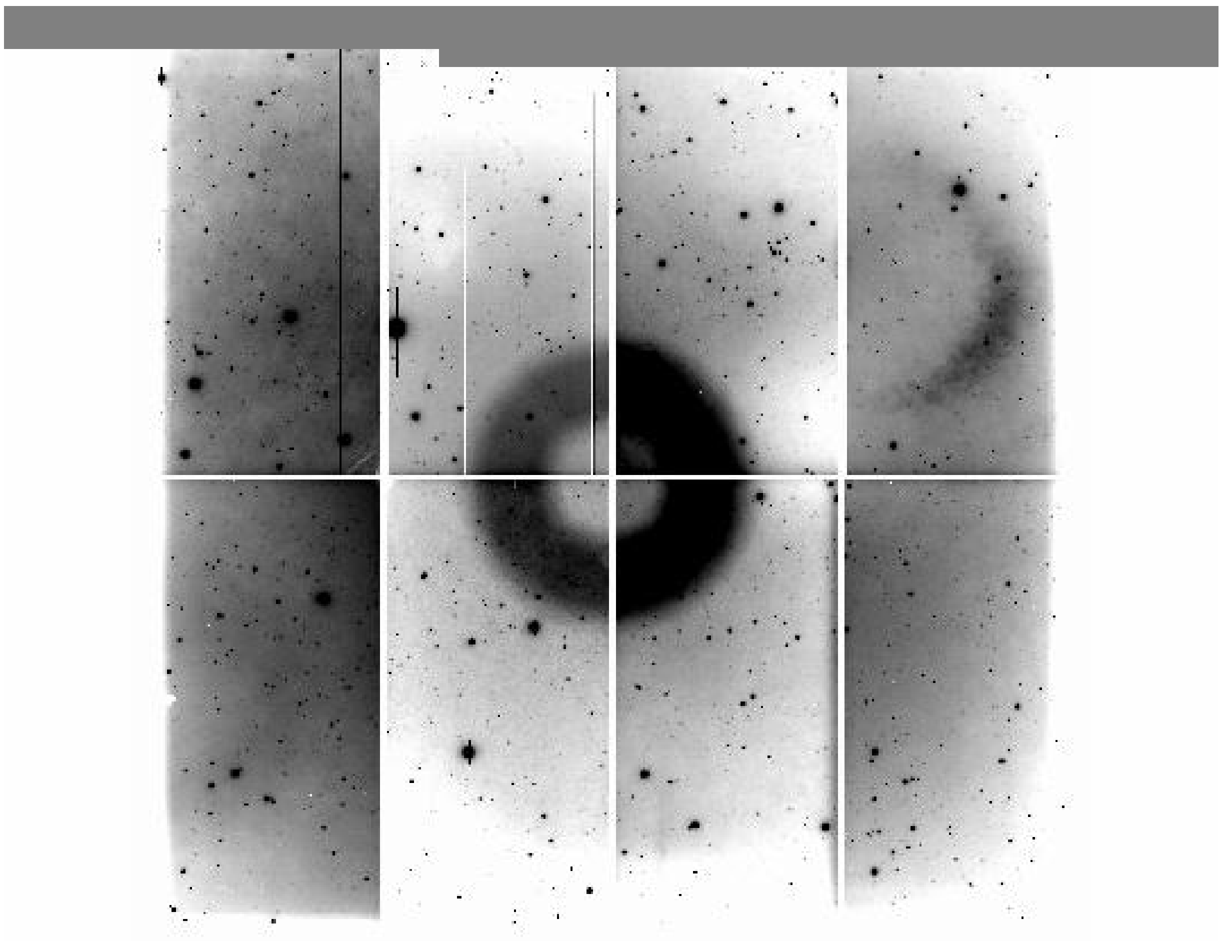

Figure 5.1: A raw image of the HDFN01 field taken in the $m(802nm)$ band. The patterns due to flat-field can be clearly seen. The central ring structure is the pupil image, which is an additive component that should be removed by subtraction.

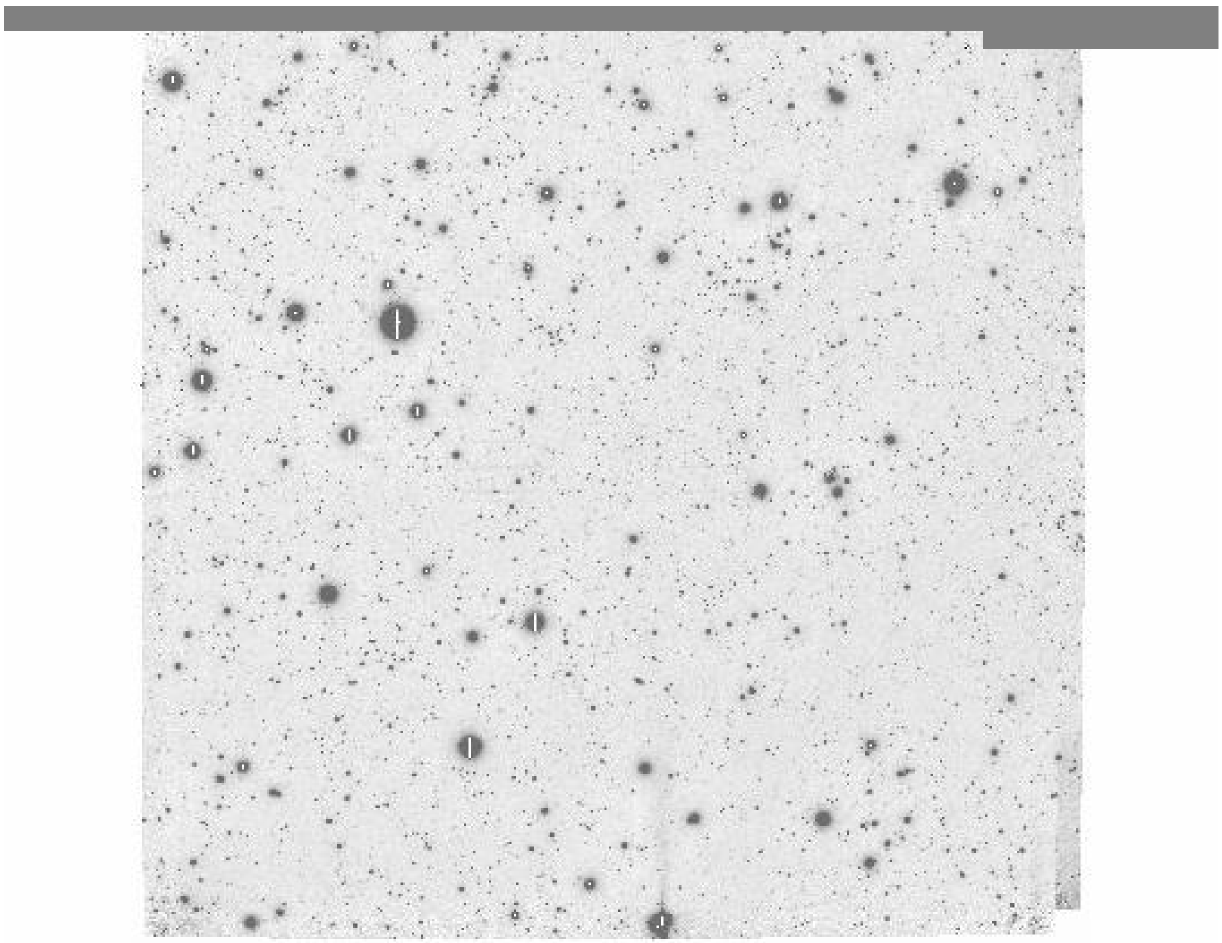

Figure 5.2: For illustration purpose, the final stack of the HDFN01 field in the $m(802nm)$ band is shown here.

however, this package was only available as one of the external packages to IRAF and needed to be fetched and installed. Unfortunately, for some unknown reasons the installation of this package failed. Therefore, the reduction of the CTIO 0.9m data were done by using a set of homegrown IRAF scripts that utilize the basic CCD image reduction tasks of IRAF. This was not as complicated as it sounded, because after all only the overscan subtraction and trimming were not straightforward. After this step was done, the remaining steps could be trivially carried out by those standard tasks in IRAF.

For all these data, no dark current subtraction was performed. The dark currents for all these CCD's were at a few electron/pixel/hour level, and the target exposures were all short, from as short as one second to ten minutes as the longest. Therefore the dark currents were negligible.

The de-fringing step was also skipped. None of the data taken at the 61$''$ in December, 2001 has any fringing pattern because the CCD used was a thick chip. For other data, only the $p(974nm)$ images have significant fringe patterns. It was very difficult to derive a reliable fringe template based on those short exposure data. Since all the fields were observed for several times with slight positional offsets and therefore a given object was not at the same position of the CCD in different exposures, the effect of fringing could be minimized after averaging the photometric results.

CHAPTER 6

Photometry, Magnitude Calibration and Survey Depth

6.1 Setting up Comparison Stars

Again, the detailed results of the calibration programs at both the Steward 61″ telescope and the CTIO 0.9m telescope will be described elsewhere. This section will only summarize the parts that are relevant to the magnitude calibration of the survey fields.

As summarized in Table 4.2, the HDFN-cal field was calibrated in two photometric nights of May, 2001, while the HDFN-cal3 field was calibrated in two photometric nights of December, 2001. All these four photometric nights are of very high quality, as shown in Table 6.1. The extinction equation used is in this form:

$$m_{inst.} = m_{batc} + K \cdot X + C,$$

where $m_{inst.}$ is the instrumental magnitude, m_{batc} is the standard magnitude in the BATC system, K is the extinction coefficient, and C is the zeropoint. No color-term is involved in the extinction equation. The extinction solutions given in Table 6.1 were derived in a way that is very similar to that described in Yan et al. (2000).

A total of seven stars from these two fields, one from HDFN-cal and the other six from HDFN-

Table 6.1: Relevant photometric nights from the Mt. Bigelow calibration campaign

	m			n			o			p		
Date	K	C	rms	K	C	rms	K	C	rms	K	C	rms
5/21-22	0.073	3.819	0.008	0.059	4.660	0.010	0.122	4.879	0.013	0.138	5.656	0.015
5/25-26	0.073	3.825	0.017	0.067	4.653	0.015	0.125	4.896	0.026	0.134	5.682	0.029
12/18-19	0.028	4.395	0.009	0.016	5.208	0.009	0.042	5.738	0.016	0.047	6.725	0.018
12/21-22	0.030	4.377	0.012	0.035	5.166	0.014	0.056	5.709	0.038	0.036	6.725	0.057

cal3, have sufficient S/N and they were chosen as the comparison stars of the HDFN01 survey field.

The calibration of the HDF-South field was less straightforward, because the standard stars used in the observations, the stars in the three SA fields, have not yet had their BATC magnitudes precisely determined. The archival data from the BATC Survey, as well as the data obtained at the Mt. Bigelow, have been used to tie their magnitudes to the BATC system. While the photometric nights during which these data were taken are all of high quality, the derived BATC magnitudes of those stars in different nights agree to each other to only 0.05–0.1 mag level. At the time of writing, this problem is still under investigation. Four to five comparison stars have been established in the HDF-South field in a similar manner as in the HDF-North fields, but their magnitudes, and thus the calibration of the HDF-South survey field, were only accurate to about 0.1 mag level at this stage. However, this accuracy is still sufficient for the purpose of this thesis.

6.2 Photometry of the Survey Fields

For the convenience of the analysis that will be carried out later, the final stacks of each field have been registered to a common astrometrical grid by shifting in integer pixels. The photometry of the survey fields was done by using SExtractor (V2.1.6) of Bertin & Arnouts (1996).

To ensure accurate color information, the double-input mode of SExtractor was used to perform matched-aperture photometry. In this mode, SExtractor operates on two properly registered images. The source detection is done in the first image (detection image) and the locations of the detected sources are derived. Furthermore, the photometric apertures (their centers, shapes and sizes) of the sources are also defined based on their appearances on the detection image. The photometry of the sources is done in the second image (target image), using the apertures that already defined. If several images, say, images obtained in different passbands, are used in turn as the target images to a same detection image, the resulting photometric results in different passbands for a given detected source are obtained with a given aperture, i.e., this is matched-aperture photometry. The photometry on the detection images themselves, of course, was done by using the single-input mode of SExtractor.

For a given survey field, the stacks in different passbands were used in turn as the detection images. For example, if we are interested in picking up $z = 6.5$ objects, we should expect that they have a strong feature, either the Lyα emission line or the Lyman-break, in the $o(919nm)$ band. Therefore, the stack in the $o(919nm)$ band should be used as the detection image. Similarly, using the stack in the $n(848nm)$ band as the detection image is to find objects that have a feature in the $z = 6.0$ window, and so on.

Objects were detected on the detection images by applying a 9×9 Gaussian smoothing kernel with a FWHM of 5.0 pixels, which is approximately the FWHM of a point source (i.e., the PSF) on all the stacks. The detection hreshold was set to 1.5 σ, and at least 5 connected pixels above this threshold were required for a source to be a positive detection. Note that the objects were detected on the *convolved* images, and therefore the detection threshold here is the threshold on the *convolved* images but not on the original detection images. The total magnitude (corresponding to the *mag-auto* option in SExtractor) was used for the photometry. The resulting catalogs were grouped based on their detection images. For example, the HDFN01 field has four final stacks, one in each passband. These four stacks were used in turn as the detection images, and therefore there are four groups of catalogs and each group has four catalogs. The catalogs in each group were then merged into one master catalog. We refer to these master catalogs as the "matched catalogs", and most of the subsequent analysis was done on these matched catalogs.

The catalogs obtained on the detection images themselves were still useful; the depth assessment in each passband was done by using these catalogs (see below).

6.3 Transferring Magnitudes to the Standard BATC System

With the comparison stars in the fields, the instrumental magnitudes obtained as mentioned above were then transfered to the standard BATC system. However, there were still several intermediate steps to go through, which will be detailed below. To summarize, the calibration of the HDFN01 and HDFN02 fields is accurate to within ~ 0.02 mag, while that of the HDFS01 field is accurate to 0.1–0.2 mag[1].

6.3.1 HDFN01 Field

For the HDF-North fields, the transformation started from the HDFN01 field. As it turned out, two to four of the comparison stars were not saturated in the half-hour individual deep exposures[2]. Therefore, all these individual deep exposures (at least seven images per passband), as well as the 5-minute short exposures (one per passband), were used in the transformation to reduce the random error. No weighting has been applied to either the deep exposures or the short exposures. These images will be referred to as "individual images" below.

SExtractor was run on these images to get the instrumental magnitudes of the objects in the individual images. A high detecting threshold, 10 σ, was used, because only the objects with high S/N should be used in the transformation. The catalogs thus derived will be referred to as "individual catalogs". For each of these catalogs, the compassion stars were identified, and the differences between their instrumental magnitudes and their BATC magnitudes were calculated (saturated comparison stars were excluded). These values were then averaged to get the mean magnitude offset that should be applied to all the objects in this individual catalog to transfer to the standard BATC system. After all the individual catalogs of a given passband have been corrected with the appropriate magnitude shifts, they were cross-matched to generate a new catalog. The mean magnitude and the corresponding *rms* value were calculated for each object in this catalog. It was

[1]These figures refer to the systematic accuracy.

[2]The exceptions are the $o(919nm)$ band deep exposures of the HDFN01 field, where all the comparison stars are saturated and the calibration has to rely on the 5-minute exposure alone.

found that the individual measurements agreed to each other to within 0.02–0.03 mag. Therefore, the objects with *rms* values larger than 0.03 mag were rejected, and a cleaned catalog, hereafter the "calibrated catalog", was obtained. The magnitudes of the objects in the calibrated catalogs in all passbands were mostly in the range of 16–18 mag. Each calibrated catalog has more than 100 objects left.

The magnitudes in a given matched catalog were transferred to the BATC system in the following way. For each passband, the objects in the calibrated catalog were identified in the matched catalog, and the differences between their instrumental magnitudes and their BATC magnitudes were calculated. The appropriate magnitude offset was obtained by taking the mean of the differences, and it was subsequently applied to the matched catalog.

To access the survey depths of each passband, the catalogs obtained by running SExtractor on the detection images (see §6.2 above) were also calibrated in the same way.

6.3.2 HDFN02 Field

Since there is no comparison star in the HDFN02 field, the magnitude transformation for this field had to be done through the overlapping field, HDFN-tran.

The individual catalogs of the HDFN-tran field were calibrated by using the calibrated catalogs of the HDFN01 (see above section). The resulting catalogs were then used to calibrate the individual catalogs of the HDFN02 field in the same way as that was done for the HDFN01 field. All the subsequent steps were also the same and will not be detailed here.

6.3.3 HDFS01 Field

This field did not go through the meticulous steps as mentioned above, because the comparison stars in this field have not been calibrated to an accuracy of a few percent of a magnitude. Instead, the comparison stars were identified in the master catalogs and the mean magnitude offsets of each passband were calculated. After applying these offsets, the master catalogs were transfered to the

BATC system.

6.4 Survey Depth

There is no universal way of quoting survey depth in the literature. In this thesis, the survey depth in a given passband is defined as the magnitude at which the source count drops to half of its maximum value in the count histogram. As an example, the source count histograms of the HDFN01 field, which were constructed based on the calibrated catalogs of the detection images, are shown in Figure 6.1. Only the sources that have S/N $> 3\sigma$ were included in the histograms. The S/N was obtained for a given source by using the simple relation $S/N = 1.0857/err(m)$, where $err(m)$ is the photometric error reported by SExtractor for this source. The depths of the HDFN02 field are similar to those of the HDFN01 field, while those of the HDFS01 field are about 0.2 mag deeper. The smaller seeing and the darker background of the latter can explain the differences.

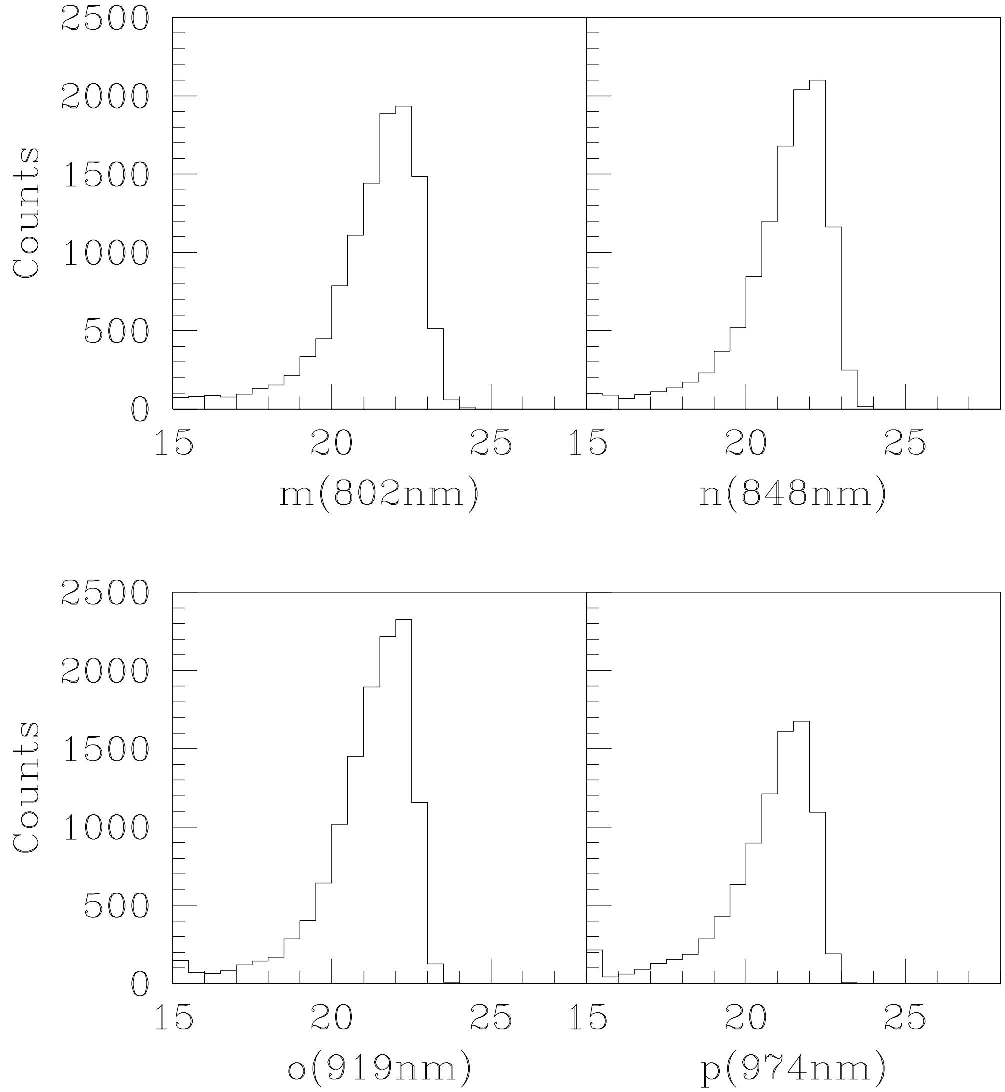

Figure 6.1: The source counts in the HDFN01 field. Only the ojbects with $S/N > 3\sigma$ were included. The depths of the HDFN02 field are similar to those of the HDFN01 field, while the depths of the HDFS01 field are 0.2 mag deeper in general.

CHAPTER 7

Candidate Search

The "matched catalogs" (see §6.2) were used in the candidate search. The objective was to detect the characteristic signature of a $z \simeq 6$ object, either the Lyman-break or the Lyα emission line, in each of the passbands. As discussed in §3.1, if the continuum level of a $z \simeq 6$ object falls within the survey limits, it can be detected through its Lyman-break signature. If its continuum is not bright enough, it still has a chance to be selected if it has a strong Lyα emission line. We will refer to these two cases as "Lyman-break candidates" and "Lyα candidates", respectively.

The search was done on a passband-by-passband basis. For a band that is not the bluest band, the drop-out technique was used, i.e., a candidate was defined as an object that was detected in this band but was invisible in the bluer band(s). In this case the search technique itself does not discriminate if an object selected is a Lyman-break candidate or a Lyα candidate. If the characteristic signature occurs in the bluest band (for the HDFN01 field it is the $n(848nm)$ band, and for the HDFN01 and HDFN02 fields it is the $m(802nm)$ band), it can only be detected if it is a strong Lyα emission line because the Lyman-break cannot be detected without a bluer band. Therefore, in this latter case a candidate was selected as an object that was detected in this bluest band but was *not* detected in the redder band next to it, which served as the continuum band. Of course, in this case lower redshift emission line objects can also be selected as candidates, and with our data alone we cannot distinguish them.

7.1 HDFN01 Field

This field has four bands of observation, namely, $m(802nm)$, $n(848nm)$, $o(919nm)$, and $p(974nm)$. The first three bands reached comparable depths, but the depth in the $p(974nm)$ band was about one magnitude shallower.

The drop-out technique was used to search for candidates in the $n(848nm)$, $o(919nm)$ and $p(974nm)$ bands. The most important criterion is that a valid candidate should not be visible in the bluer band(s). Generally speaking, the net count within an aperture (defined on the detection image; see §6.2) would be zero if there is no source presents, and SExtractor would assign a value of 99.0 to it as its magnitude. If the background is overestimated, the net count would be negative, where SExtractor would still set its magnitude to 99.0. However, if the background is underestimated, the net count would then be larger than zero, and SExtractor would then calculate the magnitude in the normal way. Thus we need to decide on the threshold above which a source should be technically taken as not detected in a given bluer passband. Note that there is a subtle difference between this threshold and the survey depth of this band, which will be shown below. Another important criterion is that a valid candidate should be significantly detected in the target band. Assuming a simply relation between the reported photometric error and the corresponding S/N associated to a source, we took any sources with reported photometric error of less than 0.20 mag (or equivalently, $S/N = 1.0857/0.20$) as reliable detections.

1. $n(848nm)$ *band search*: By looking at the $m(802nm)$ band source count histogram extracted from the matched catalog which was obtained by using the $n(848nm)$ image as the detection image, it was decided that the threshold for the $m(802nm)$ band was 23.5 mag. All the sources that have $n(848nm)$ band photometric errors less than 0.2 mag and $m(802nm)$ band magnitude fainter than 23.5 mag were extracted from the matched catalog. After getting rid of the objects that were on the field edges, the candidate list had 91 objects left.

For each of these 91 candidates, the images in all the four bands were displayed to the screen and were visually examined to make sure that these objects were real detections and their reported faintness in the $m(820nm)$ band was real. Only eight objects survived after this visual check, which we will refer to as the n-band candidates. As it turned out, all these eight candidates have color index $(m - n) > 1.40$ mag, among them three have $(m - n) > 2.0$ mag. Based on their brightness in the next redder band, $o(919nm)$-band, all but one are Lyα candidates. Twenty-five of the original 91 objects turned out to be defects due to reasons such as imperfect overlapping of the gaps between CCD chips, residual of satellite trails, "bleeding spikes " from badly saturated stars, etc. The remaining 58 objects turned out to be actually visible in the $m(802nm)$ band. It was found that only 17 of these 58 objects have $(m - n) > 1.4$ mag, and thus applying a cut at $(m - n) = 1.4$ mag seemed to be a good additional criterion to further narrow down the candidate list. This value implies a factor of 3.63 in flux decrement.

2. $o(919nm)$ *band search*: Similar to the case above, from the matched catalog of the $o(912nm)$ band it was found that the thresholds of $m(802nm)$ and $(n848nm)$ bands were 24.0 mag and 23.7 mag, respectively. Furthermore, two additional criteria based on color indices, $m - o > 1.4$ and $n - o > 1.4$, were also applied based on the investigation above. After trimming off the field edges, 20 candidates were obtained. Visual inspection revealed that 12 of them were defects, and 1 of them was barely visible on both the $m(802nm)$ band and the $n(848nm)$ band. Thus seven candidates finally remained. Among these seven candidates, three of them have $(m-o) > 2.0$ and $(n-o) > 2.0$. It is not possible to judge if these objects are Lyman-break candidates or Lyα candidates, as the redder band next to it, $p(974nm)$-band, does not reach comparable depth.

3. $p(974nm)$ *band search*: The magnitude threshold for all the three bluer bands was 22.0 and the color index threshold was 1.4 for all $(m - p)$, $(n - p)$ and $(o - p)$. However, visual inspection showed that all the objects selected (44 of them in total) were defects.

4. $m(802nm)$ *band search*: The matched catalog that used the $m(802nm)$ band stack as the detection image can only be used to search for Lyα candidates. The criterion used was $m-n < -1.4$. Ten objects were selected after trimming the field edges. Visual inspection rejected three of them as image defects. The final list consists of seven candidates. Among these objects, four of them also have $m - o < -1.4$.

All these candidates are listed in Table 7.1. As a demonstration, Figure 7.1 shows the locations of these candidates on the different color-magnitude diagrams.

7.2 HDFN02 Field

The search on this field was carried out in a similar way, and is summarized below. Note that a source should have photometric error of less than 0.2 mag in the target band to be included in the search.

1. *n(848nm) band search*: With the criteria of $m > 23.5$ mag and $(m-n) > 1.4$, twenty objects were selected after field edge trimming. Five of them were found to be defects, while seven were found to be still visible in the m(802nm) band. The final candidate list consists of eight objects, among which six have $(m-n) > 2.0$. Among them, seven are Lyα candidates while one is Lyman-break candidate.

2. *o(919nm) band search*: The criteria were $m > 24.0$, $n > 23.7$, $(m-o) > 1.4$, and $(n-o) > 1.4$. Twenty objects were selected. However, visual examination found that all of them were false detections and no candidate survived.

3. *m(802nm) band search*: Using the criterion of $(m-n) < 1.4$, 96 objects were selected after field edge trimming. Eighty-eight of them turned out to be defects. In addition, one object is obviously too bright to be a legitimate candidate ($m = 15.3$ mag). The final candidate list consists of seven Lyα candidates. Among them, four also have $(m-o) < 1.4$.

All these candidates are listed in Table 7.2.

7.3 HDFS01 Field

The search in this field was carried out in the similar way as mentioned above, and will not be detailed here again. To summarize, only three candidates were selected, all found in the $o(919nm)$ band. These three objects were shown in Table 7.3. It is not clear if they are Lyα candidates or Lyman-break candidates because the survey limit in the $p(974nm)$-band is not deep enough.

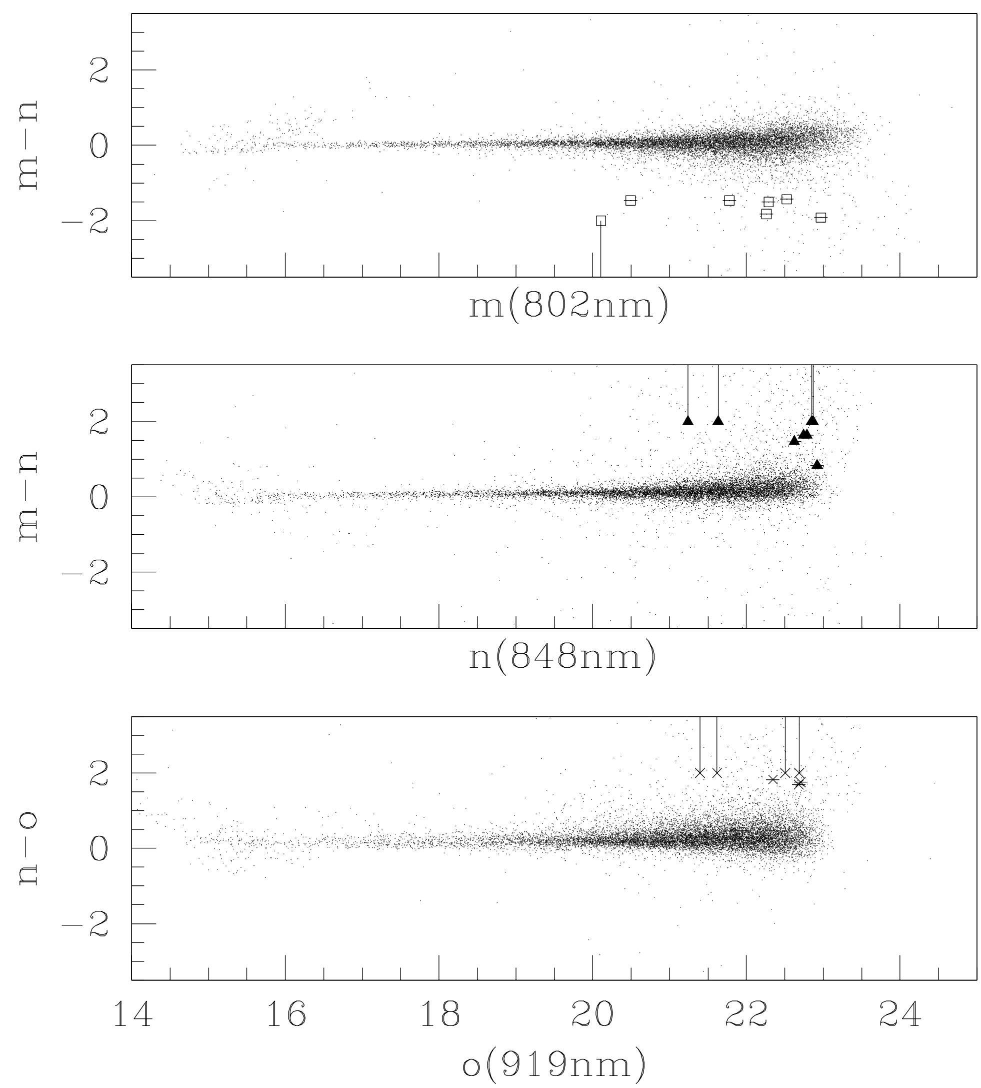

Figure 7.1: The candidates selected from the HDFN01 field are shown on the color-magnitude diagrams. From the top to the bottom, the $m(802nm)$–, $n(848nm)$– and $o(919nm)$–band candidates are plotted in squares, triangles and crosses, respectively, while the field objects are plotted in dots. The candidates whose color indices are larger (smaller) than 2.0 mag are assigned their color indices of 2.0 mag and are plotted with lower (upper) limits. The candidates selected from other fields are similar in nature on the color-magnitude diagrams.

Table 7.1: Candidates found in the HDFN01 field

ID	α	δ	m	err_m	n	err_n	o	err_o	p	err_p
	$m(802nm)$	Candidates								
01	12:38:51.00	62:20:50.79	20.108	0.014	22.285	0.180	21.832	0.126	22.185	0.543
02	12:38:33.30	61:59:58.39	22.524	0.092	23.956	0.617	23.322	0.365	—	—
03	12:38:18.60	62:13:59.00	22.289	0.084	23.793	0.603	23.007	0.310	22.853	0.840
04	12:37:51.60	62:03:02.19	21.779	0.054	23.247	0.370	23.406	0.454	—	—
05	12:37:32.90	62:17:13.59	22.971	0.116	24.889	1.210	23.066	0.241	—	—
06	12:36:44.70	62:09:27.10	20.495	0.033	21.959	0.227	22.416	0.366	20.790	0.256
07	12:35:40.90	62:06:19.70	22.261	0.078	24.080	0.741	26.142	5.238	22.446	0.546
	$n(848nm)$	Candidates								
08	12:37:28.20	62:30:34.90	25.493	0.624	22.866	0.103	27.150	5.508	24.123	1.064
09†	12:37:17.30	62:02:26.10	23.750	0.135	22.922	0.114	22.464	0.081	22.149	0.186
10	12:37:10.30	62:18:12.70	23.699	0.212	21.240	0.041	—	—	23.511	1.065
11	12:36:59.90	62:09:48.10	24.088	0.261	22.624	0.124	23.194	0.221	22.607	0.400
12	12:36:36.50	62:14:19.10	26.665	2.159	22.847	0.119	22.993	0.144	23.073	0.478
13	12:36:33.00	62:15:37.90	23.943	0.230	21.631	0.051	23.476	0.288	—	—
14	12:36:18.10	62:04:54.80	24.422	0.251	22.789	0.102	22.220	0.066	22.775	0.331
15	12:36:13.70	62:14:53.30	24.375	0.296	22.744	0.121	23.740	0.318	23.416	0.735
	$o(919nm)$	Candidates								
16	12:34:26.70	62:14:15.90	—	—	24.469	0.481	22.708	0.104	—	—
17	12:34:27.60	61:59:00.89	24.069	0.252	24.171	0.500	22.345	0.101	25.911	8.200
18	12:34:25.80	62:25:04.80	24.074	0.208	—	—	22.505	0.097	—	—
19*	12:38:30.20	62:31:19.40	—	—	—	—	21.618	0.084	22.478	0.572
20*	12:38:05.90	62:31:21.79	—	—	27.081	12.136	21.396	0.070	23.072	1.003
21	12:37:43.70	62:21:06.60	25.198	0.572	25.976	2.121	22.687	0.112	23.820	0.966
22*	12:37:15.40	62:31:01.70	24.098	0.246	24.376	0.573	22.681	0.130	—	—

1. RA and DEC are in J2000.0.

2. All these candidates, excepted the three that are marked with "*", are visible in at least one of the deep blue band images of the Subaru data (see §8.1), and therefore should be interlopers at lower redshifts. The three objects marked with "*" are outside of the Subaru data coverage, and cannot be verified.

3. This object does not satisify the $(m-n) > 1.4$ mag criterion; however it is included because the author suspects that the photometry in the $m(802nm)$ band underestimates its brightness.

Table 7.2: Candidates found in the HDFN02 field

ID	α	δ	m	err_m	n	err_n	o	err_o
	$m(802nm)$	Candidates						
01	12:36:55.40	61:31:04.30	22.491	0.120	23.924	0.550	24.293	0.685
02	12:36:54.40	61:42:18.50	22.379	0.099	—	—	—	—
03	12:36:30.30	61:35:42.40	22.079	0.075	23.968	0.518	23.856	0.415
04	12:36:13.50	61:37:00.80	22.676	0.115	24.198	0.573	25.721	2.058
05	12:35:53.90	61:25:15.50	21.662	0.069	23.145	0.329	22.855	0.224
06	12:35:18.60	61:39:30.30	22.826	0.108	—	—	—	—
07	12:34:41.90	61:29:40.10	21.840	0.078	23.502	0.441	23.159	0.286
	$n(848nm)$	Candidates						
08	12:38:20.80	61:45:35.60	—	—	22.676	0.125	—	—
09	12:38:12.50	61:38:02.70	24.564	0.670	22.361	0.110	22.970	0.171
10	12:35:52.60	61:37:44.69	23.985	0.496	21.421	0.058	23.219	0.269
11	12:35:52.00	61:35:43.20	24.222	0.354	22.793	0.118	22.631	0.092
12*	12:35:27.20	61:23:20.19	—	—	22.246	0.102	23.357	0.251
13	12:35:01.80	61:35:56.51	23.743	0.375	22.033	0.096	23.486	0.323
14	12:34:30.30	61:39:37.30	26.790	3.580	22.282	0.071	26.900	4.324
15	12:34:43.50	61:25:20.40	24.562	0.588	22.413	0.101	—	—

1. RA and DEC are in J2000.0.
2. No candidate was found in the $o(919nm)$ band.
3. The object marked with "*" has been spectroscopically confirmed to be a strong emission-line galaxy at $z = 0.69$ (H. Spinrad & D. Stern, private communication, April 2003).

Table 7.3: Candidates found in the HDFS01 field

ID	α	δ	n	err_n	o	err_o	p	err_p
	$o(919nm)$	Candidates						
01	22:31:18.89	-60:53:40.37	25.340	1.700	22.100	0.060	24.860	1.400
02	22:30:14.44	-60:38:07.16	24.880	1.590	21.820	0.070	21.890	0.130
03*	22:32:27.55	-60:48:42.62	24.340	0.580	22.280	0.060	23.610	0.380

1. RA and DEC are in J2000.0.
2. The first two candidates are visible in the bluer band images of the BTC (see text) and thus are lower redshift interlopers. No.03 is outside of the BTC coverage and thus cannot be verified.

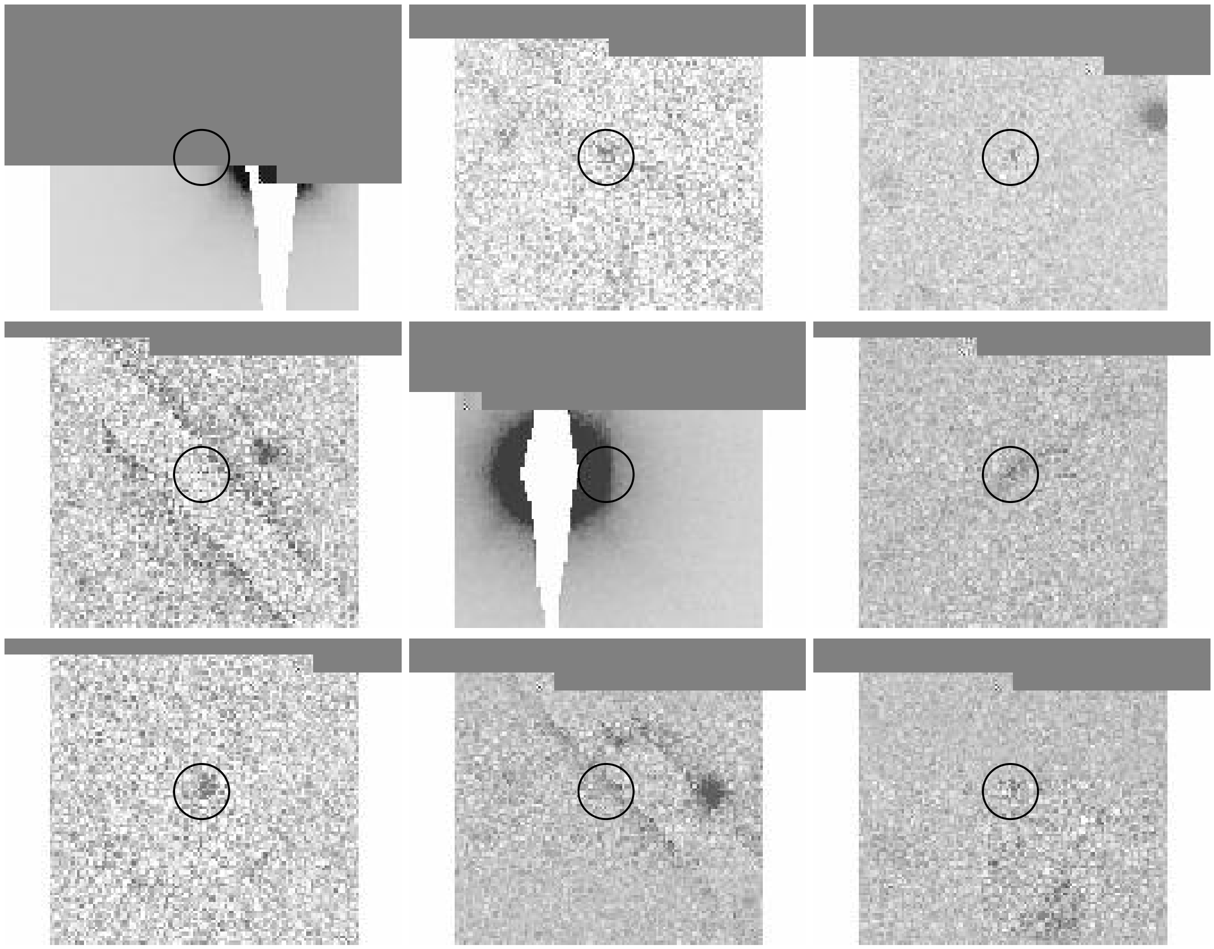

Figure 7.2: Image stamps of 9 rejected "candidates" during visual examing. Most of such rejected objects are bogus detections due defects such as residual of satellite trails, "spikes" of saturated stars, uncleaned pixels at around the region of the gaps in between CCD chips, and so on.

7.4 Examples of candidate selection

As mentioned above, visually examing the candidates selected is a very important step — its importance can never be emphasized enough. As examples, Figure 7.2 shows some image stamps of the candidates that were rejected during this process. Most of the rejected "candidates" are bogus detections due to defects such as residual of satellite trails, "spikes" of saturated stars, uncleaned pixels at around the region of the gaps in between CCD chips, and so on. For comparison, the image stamps of some of the survived candidates are shown in Figure 7.3.

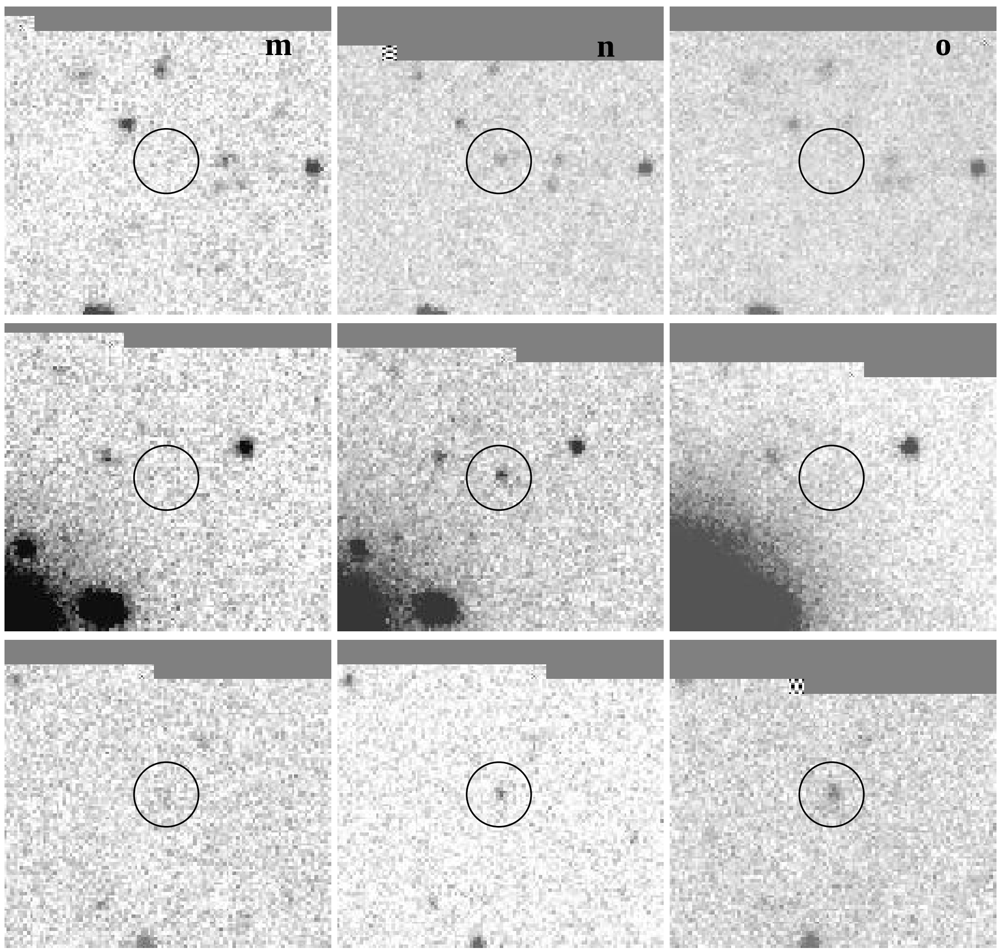

Figure 7.3: Image stamps of 3 candidates that survived the visual examing step. Only the stamps in $m(802nm)$, $n(848nm)$ and $o(919nm)$ are shown. The top two objects are Lyα candidates in the $n(848nm)$ band, while the bottom one is a Lyman-break candidate in the same band.

CHAPTER 8

Conclusion

8.1 Candidate Verification

The candidates of our survey were selected based on photometric results within the spectral range of 8000–9900Å. Preferably, they should be verified on a longer spectral baseline. Fortunately, there are indeed some other data can be used for this purpose.

The HDF-South proper has been imaged at the CTIO 4m in the broad-band UBVRI with the Big Throughput Camera (BTC) before the commission of the MOSAIC II camera (Palunas et al. 2000). These images have about a $15' \times 15'$ overlapping region with the HDFS01 field of ours. Two of the three candidates selected in the HDFS01 field happen to be within this overlapping region. It was found that these two candidates were both clearly visible on the BTC R-band and bluer images, but not on the I-band image. Thus these two objects are most likely lower redshift interlopers, possibly $z = 2.3$ quasars with $MgII$ redshifted to $\sim$ 9100Å. This meant that at best only one positive candidate in this field could be at $z \simeq 6$. As mentioned before, we do not know whether this object is a Lyα candidate or a Lyman-break candidate.

Just a couple of weeks before the previous chapter was written, a new set of data, mostly from the 8m Subaru telescope, became available to the public (hereafter the Subaru data; P. Capak et al. 2003, submitted to AJ). These deep imaging data in the broad-band UBVRI and z' cover ~ 0.2 deg^2 centering the HDF-North proper, and overlap almost the entire HDFN01 field of ours.

As it turns out, all the $m(802nm)$- and $n(848nm)$-band selected candidates in the HDFN01 field are visible in at least one of the UBVR bands of the deep UBVRI Subaru data, and therefore cannot be at $z \simeq 6$. Four of the seven $o(919nm)$-band candidates were also rejected for the same reason. The remaining three $o(919nm)$-band candidates were out of the field of the Subaru data, and thus cannot be verified. Two of these three candidates are quite bright ($o = 21.4$ and 21.6 mag) and thus are less likely to be at $z \simeq 6$. Therefore, similar to the case of the HDFS01 field, it seems that the HDFN01 field has only one object at most that can be at $z \simeq 6$. Similarly, we do not know whether this object is a Lyα candidate or a Lyman-break candidate, either.

The HDFN02 field does not have any other data that can be used to do further verification. Only one candidate is a Lyman-break candidate, and the other fourteen are Lyα candidates. Given the result in the HDFN01 field, we expect that the vast majority of these 15 candidates are also lower redshift interlopers.

8.2 Additional Candidates from the Subaru Data Alone

The Subaru data[1] mentioned above are among the deepest data ever obtained with ground-based telescopes. Their sky coverage, ~ 0.2 deg^2, is undoubtedly the widest among all the data of similar depth. Therefore, these data alone can be used to search for $z \simeq 6$ objects. To get a sense of their survey depths, the number count histograms, constructed in the way as described in §6.4, are shown in Figure 8.1.

The candidate should be selected as I-band drop-out's. Note that the broad-band I filter at the Subaru telescope is significantly different from the one used at NOAO in the sense that it only slightly overlaps with the z' filter, as shown in Figure 8.2. Thus the redshift window corresponds to z' vs. I combination is $6.0 \leq z \leq 6.5$. The lower redshift bound is set by the blue end cutoff of the z'-band system response, while the upper redshift bound is set by the red-end cutoff of its system response. The nominal $(I - z')$ color index for a model galaxy at $z = 6.0$ as shown in Figure 8.2 is 1.9 mag.

Matched aperture photometry was carried out on all the six images, using the double-input mode of SExtractor. The z' stack, of course, was used as the detection image. A 7×7 Gaussian

[1]The images in $BVRI$ and z' were obtained at the 8.2m Subaru telescope with the Suprime-Cam whose FOV is $34' \times 27'$, while the images in U were obtained at the KPNO 4m with the MOSAIC.

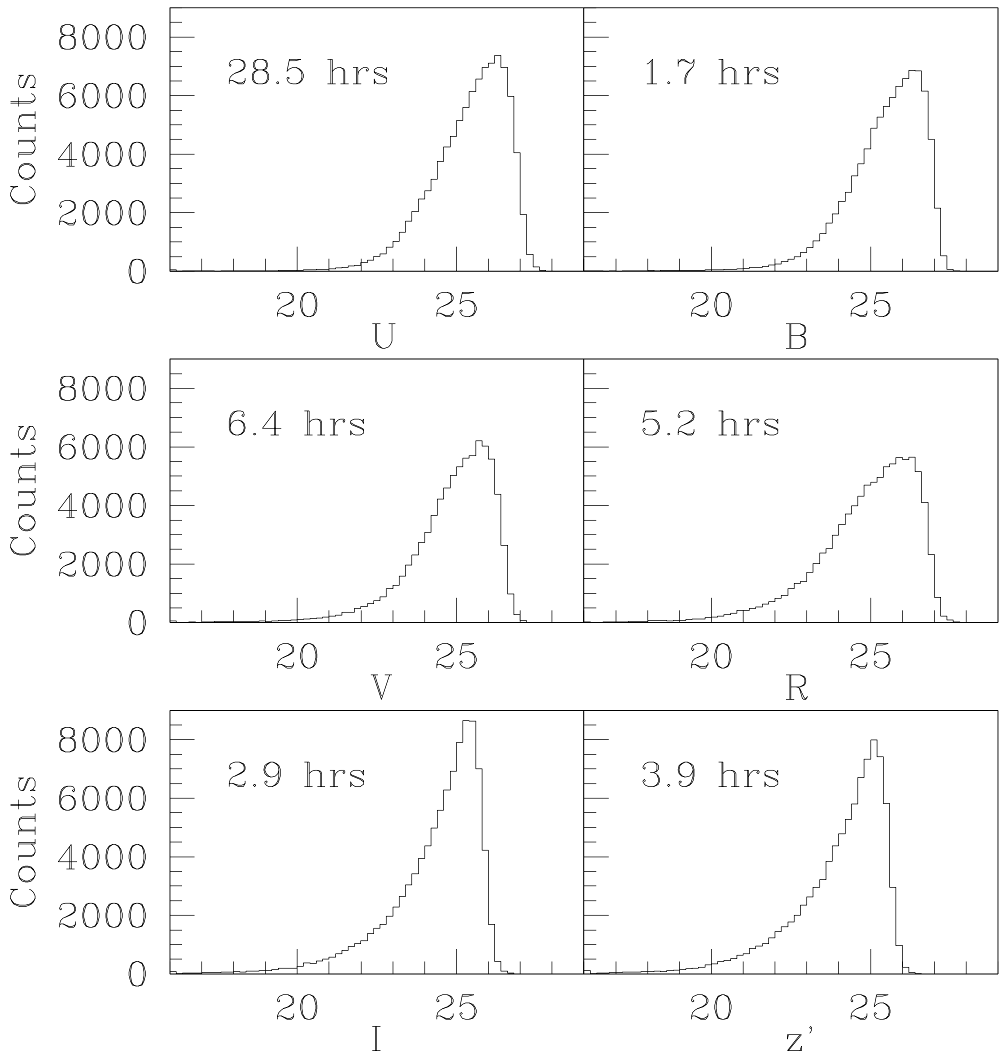

Figure 8.1: Count histograms of the deep Subaru data. Only objects having $S/N > 3\,\sigma$ are included. The total integration time of each passband is also labeled. Note that the U-band images were taken with the MOSAIC-I camera at the KPNO 4m.

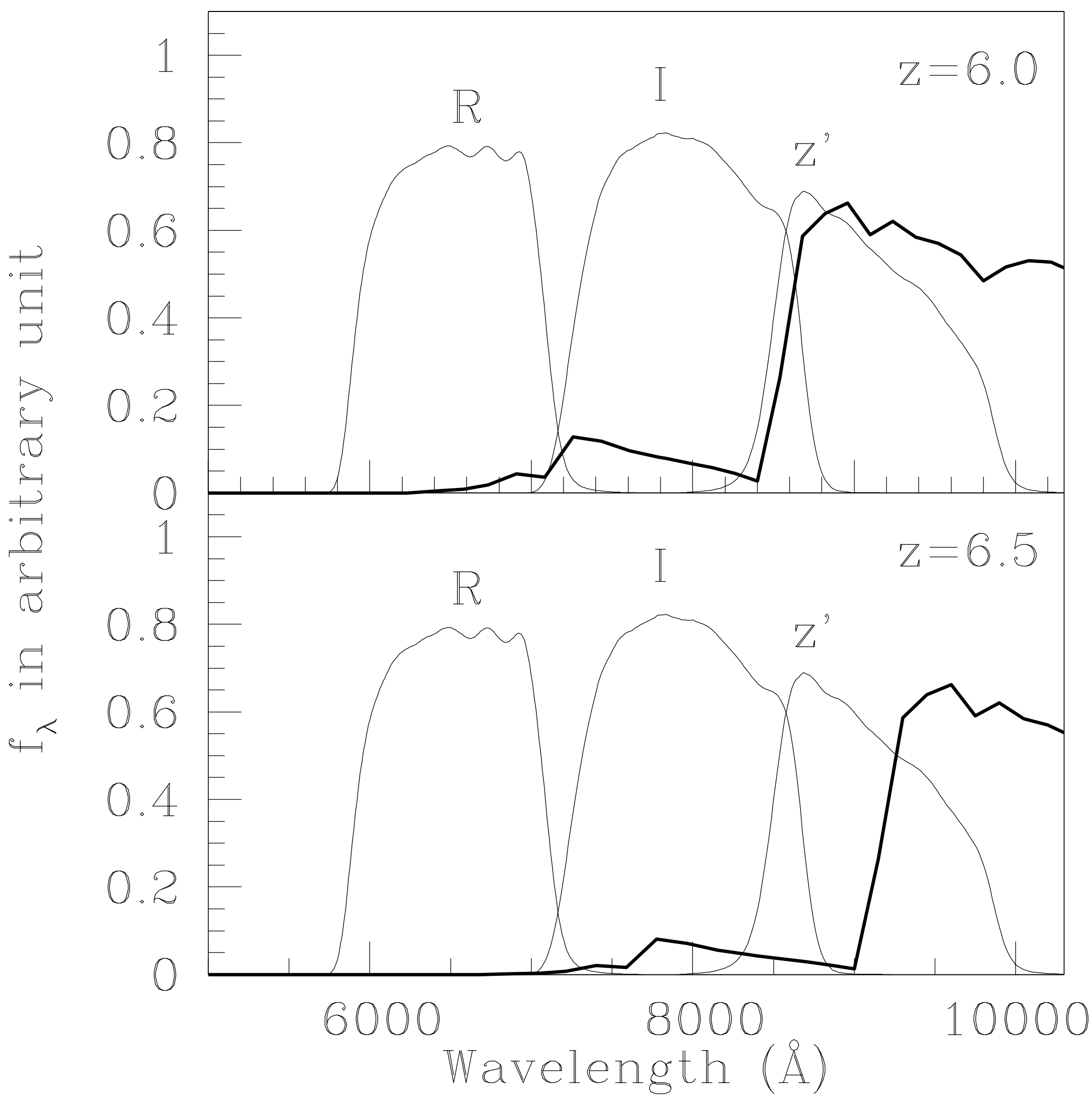

Figure 8.2: The system response curves of the Subaru Suprime-Cam in the R, I and z' bands, obtained by convolving the filter transmission curves the CCD Q.E. curve. The contributions from other components are ignored. The SED of a model galaxy (see Figure 3.3) at $z = 6.0$ and 6.5 are overplotted in thick line.

Table 8.1: Candidates found in the Subaru data

ID	α	δ	I	err_I	z'	err_z	$I - z'$
01	12:38:25.38	62:00:34.58	27.778	1.100	25.320	0.148	> 2.00
02	12:35:01.90	62:00:34.30	26.684	0.604	24.353	0.091	> 2.00
03	12:37:52.91	62:05:56.40	26.921	0.600	25.074	0.141	1.85
04	12:34:45.22	62:05:57.33	27.478	1.536	24.442	0.121	> 2.00
05	12:34:44.74	62:09:44.29	26.969	0.937	24.143	0.090	> 2.00
06	12:39:03.01	62:11:38.55	27.288	0.751	25.396	0.170	1.89
07	12:35:16.59	62:13:56.31	27.048	0.826	24.829	0.138	> 2.00
08	12:34:27.61	62:21:15.49	—	—	25.227	0.103	> 2.00
09	12:38:44.66	62:22:29.68	28.769	3.892	24.960	0.150	> 2.00
10	12:36:27.39	61:53:48.51	27.671	0.756	25.400	0.121	> 2.00
11	12:37:05.39	61:53:56.01	26.910	0.381	25.154	0.098	1.76
12	12:35:52.89	61:54:40.07	27.764	0.645	25.364	0.092	> 2.00
13	12:38:37.56	61:55:06.39	—	—	24.569	0.106	> 2.00
14	12:38:06.03	61:55:32.71	27.245	0.572	25.106	0.103	> 2.00
15	12:37:07.89	61:56:05.80	—	—	24.714	0.104	> 2.00
16	12:37:43.23	61:56:04.92	26.978	1.010	24.085	0.091	> 2.00
17	12:38:44.57	62:25:08.17	28.218	2.020	24.879	0.120	> 2.00
18	12:35:56.87	62:27:04.14	26.751	0.573	24.903	0.135	1.85

RA and DEC are in J2000.0.

smoothing kernel with a FWHM of 4 pixels was used. The detection threshold was set to $1.5\,\sigma$, and the minimum number of connected pixels was set to 5. The magnitude zeropoints from Capak et al. (2003) were used to tie the measurements to the AB system.

The candidate search was done on the matched catalog. The criteria for an object to be selected were 1) its reported photometric error in z'-band (err_z) should be smaller than 0.2 mag, and 2) it should be fainter than 26.6 mag in all the bluer bands. Out of the 62 objects thus selected, 16 are image defects, and 28 are actually visible in at least one of the bluer bands. The final candidate list consists of 18 candidates. Clearly, the contamination rate due to lower redshift interlopers is pretty high: $28/(62-16) \simeq 61\%$. All of these 18 candidates have $(I - z')$ color index limits larger than 1.5 mag, and 14 of them have the limits larger than 2.0 mag.

These 18 candidates are shown in Table 8.1. $None$ of these objects were detected in our NOAO survey data.

8.3 Constraints to the LF

The results presented above can be used to constrain the predicted LF. As discussed in Chapter 2, among all the varients, the high normalization prediction in a (Ω_M,Ω_Λ)=(0.3,0.7) universe seems to be most realistic. From now on only this LF will be considered.

Currently we do not have spectroscopic identification on these candidates, and we can only obtain constraints to the LF in terms of upper limits. Since the magnitude used in the LF that we predicted is continuum magnitude, we also need to refer to the continuum magnitudes of the candidates in order to derive legitimate constraints.

To summarize, in our intermediate-band survey we have one candidate from the HDFS01 field, one from the HDFN01 field, and fifteen from the HDFN02 field. The large number of candidates survived in the latter field is mainly due to the fact that we do not have other verification data for this field. Among all these objects, one is Lyman-break candidate (a $n(848nm)$-band candidate from the HDFN02), fourteen are Lyα candidates (all from the HDFN02; seven $m(848nm)$-band and seven $o(919nm)$-band), and the remaining two are not certain (one each from the HDFN01 and the HDFS01; both are $o(919nm)$-band candidates).

The candidate search in our survey was carried out to a limit of 23.0 mag [2]. This is also the limit of the continuum magnitude for the Lyman-break candidates. As there is only one such candidate for certain, it implies a cumulative surface density of 1 per deg^2. Corrected for the co-moving volume difference (see Table 3.1), this number translates to 3 per deg^2 for the redshift range of $5.5 \leq z \leq 6.5$. Note that we do not include the two objects of uncertain type; the co-moving volume correction has taken them into account. Figure 8.3 shows that this upper limit agrees with our prediction, which gives a cumulative number density of only 7.8×10^{-4} per deg^2. However, if this Lyman-break candidate turns out to be really at $z \simeq 6$, it will imply that we greatly underestimated the L^* value in our prediction.

[2] For simplicity, we do not attempt to correct for photometric incompleteness.

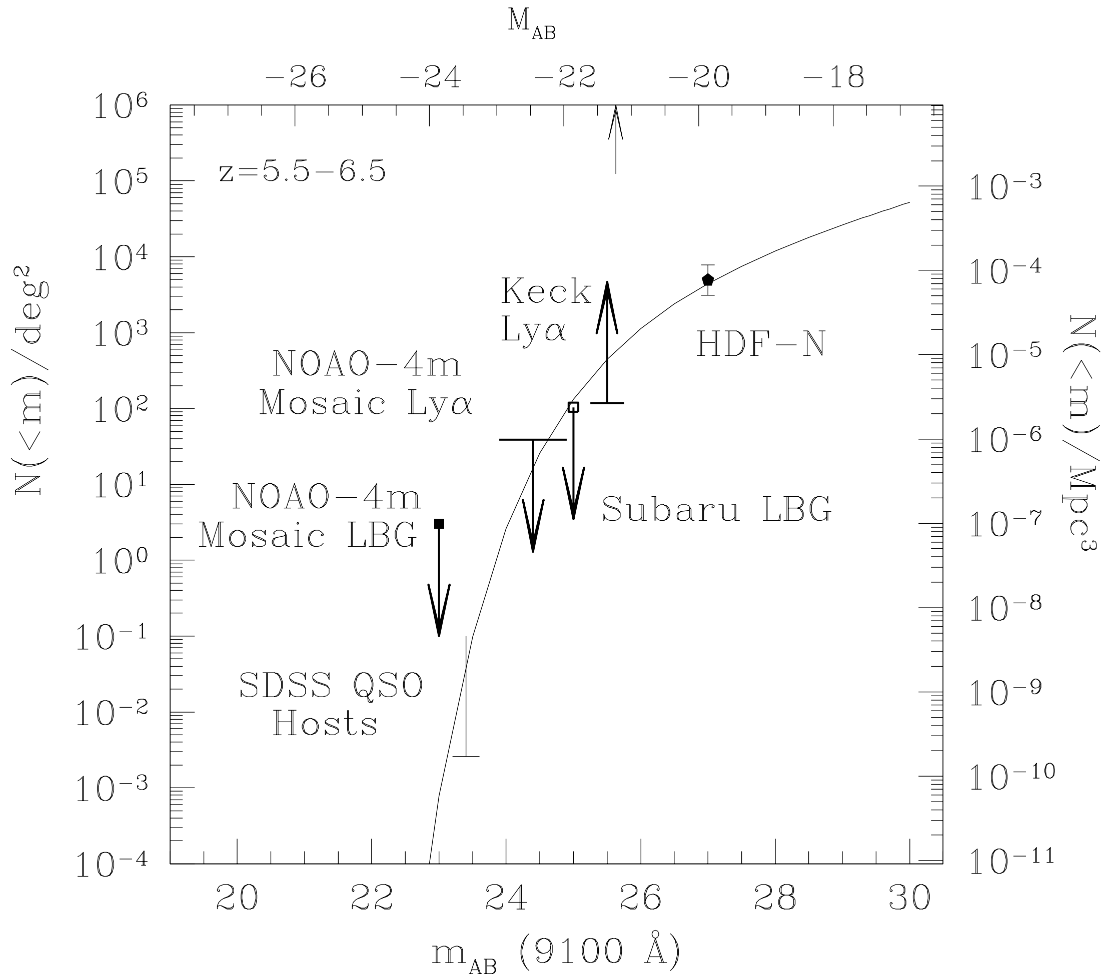

Figure 8.3: The new bright-end constraints are compared against the predicted LF, which is shown as the solid curve. The two upper limits at brighter than 25.0 mag are derived from our NOAO-4m survey, while the upper limit at 25.0 mag is derived from the public Subaru data on the HDF-N. The NOAO-4m limits do not include the correction for the incompleteness of the photometry, which would make the limits up to 50% higher. Furthermore, the NOAO-4m Lyα limit does not include the correction for the fraction of strong Lyα emitters among the entire $z \simeq 6$ population, which is not known. Also, the continuum magnitude that this limit probes has large uncertainty, as indicated by its horizontal bar. Note that our prediction is slightly higher than the upper limit derived from the Subaru data. This could suggest a smaller L^* value than what is adopted in our prediction.

The continuum magnitudes of the Lyα candidates are hard to gauge. However, as we applied a color index difference of 1.4 mag during the selection, we tentatively quote 24.4 mag as the continuum brightness limit that our survey indirectly probed through those emission-line objects. Taking it at face value, the maximum number of Lyα candidates in our survey is 16 (the two candidates of uncertain type are also counted). This implies a cumulative surface density upper limit of 16 per deg^2. The three passbands of our survey, namely, $m(802nm)$, $n(848nm)$ and $o(919nm)$, correspond to the redshift windows of z = 5.55–5.69, 5.94–6.05, and 6.46–6.62, respectively, as summarized in Table 3.1. The total co-moving volume that these three redshift windows sample is about 41% of the co-moving volume of the entire z =5.5–6.5 range. Therefore, scaled to this redshift range, our result suggests a cumulative number density upper limit of 39 per deg^2. This limit is also shown in Figure 8.3, and one can see that it is also in agreement with our prediction, which gives about 8 per deg^2 to the depth of 24.5 mag.

An important point should be made clear here. Those Lyα candidates, if they are really at $z \simeq 6$, should be strong Lyα emitters given our selection criteria. However, we do not know the fraction of strong Lyα emitters among the entire $z \simeq 6$ galaxy population. Although the vast majority of the confirmed galaxies at $z \simeq 6$ are strong Lyα emitters, this can just simply be a selection effect in spectroscopic identification. Therefore, the inferred surface density limit of the entire $z \simeq 6$ population could be higher than what inferred from our Lyα candidates.

An additional constraint comes from the candidates derived from the Subaru data, where we have 18 objects in 0.2 deg^2. All of these candidates are fainter than 24.0 mag in z', and 8 of them are fainter than 25.0 mag. Note that the survey is nearly 90% complete to 25.0 mag in the z'-band, for the sake of simplicity we only discuss the cumulative number density to the depth of 25.0 mag. At this level, the inferred cumulative number density is 50 per deg^2 for the redshift range $6.0 \leq z \leq 6.5$. The co-moving volume in this redshift range is 48% of that in the range of $5.5 \leq z \leq 6.5$. After apply this scaling factor, the inferred cumulative number density upper limit is 104 per deg^2. As the comparison, our prediction gives 131 per deg^2, which is *higher* than this upper limit by 26%. However, since only 10 objects are used to derive this upper limit, the discrepancy can still be explained by the fluctuation in such a small number statistics. More data at a similar depth are needed to further investigate this problem. If the lower surface density at this brightness level were confirmed, it would probably suggest a fainter L^* value than used in our prediction, as pointed out in §2.5.

To summarize, so far our prediction is in resonable agreement with the observations at the bright end.

PART III

FAINT-END CONSTRAINTS — ACS PARALLEL DATA

This part describes the efforts that aimed at constraining the faint-end of the LF. As our prediction suggests, pencil-beam surveys with a few arcmin^2 of sky coverage should go to a depth of AB=27.0 mag or fainter to be able to discover a significant number of $z \simeq 6$ objects. In the spectral range of 8000–10000Å, which is the range of interest in the search of $z \simeq 6$ objects, such a depth seems to be achievable only from the space. The *Advanced Camera for Surveys* (ACS) recently installed to the *Hubble Space Telescope* (HST) provides an unique opportunity to constrain the behavior of the LF at an unprecedentedly faint level. The pure parallel mode implemented for the *Wide Field Camera* (WFC) has greatly enhanced this ability. We present our preliminary analysis of a deep ACS/WFC parallel field at $|b| = 74.4^o$. We find 30 plausible $z \simeq 6$ candidates, all of which have $S/N > 7$ in the F850LP-band. The major source of contamination could be faint cool Galactic dwarfs, and we estimated that they would contribute at most 4 objects to our candidate list. We derived the cumulative number density of galaxies at $6.0 \leq z \leq 6.5$ as 2.3 arcmin^{-2} to a limit of 28.0 mag in the F850LP-band, which is slightly higher than our prediction. If this is not due to an underestimated contamination rate, it could possibly imply that the faint-end slope of the $z \simeq 6$ luminosity function is steeper than $\alpha = -1.6$. At the very least, our result suggests that galaxies with $L < L^*$ do exist in significant number at $z \simeq 6$, and that they could be the major sources that contributed the reionizing photons[3].

[3]The study presented in this part has resulted in a published paper (Yan, Windhorst & Cohen 2003b).

CHAPTER 9

Data Analysis

9.1 ACS and Its Pure Parallel Mode

The ACS, a third-generation instrument of the HST, was installed in February, 2002 during the HST servicing mission 3B. It consists of three cameras, namely, the Wide Field Camera (WFC), the High Resolution Camera (HRC), and the Solar Blind Channel (SBC). The camera of interest in this study is the WFC. This camera employs a mosaic of two 2048×4096 SITe CCD chips that are thinned, back-illuminated devices. It has a nominal FOV of 202×202 arcsecond^2 (11.3 arcmin^2) at a scale of $0.05''/pix$, and covers the spectral range of about 3800–10000Å. The entire ACS is off-axis, and thus the images obtained with this instrument need to be corrected for geometric distortion. A special routine called "PyDrizzle", which works under PyRAF[1], has been developed to perform this correction[2].

To maximize its scientific return, a default pure parallel observation mode has been implemented for the WFC (Sparks et al. 2001). This mode utilizes four filters, namely F775W (SDSS-i'), F850LP (SDSS-z'), F475W (SDSS-g'), and F625W (SDSS-r'), in order of preference. Whenever there is at least one orbit of time available for parallel observation, this mode always takes images in the F775W and F850LP bands. Given the high throughput and the wide FOV of the WFC, such a strategy makes its parallel data extremely useful for selecting objects at $z \simeq 6$ by using the drop-out technique. This is demonstrated in Figure 9.1.

Based on the statistics of WFPC2 parallel observations in Cycle 8–9, the pure parallel program is expected to yield at least 300 orbits of high galactic latitude ($|b| > 20^{\circ}$) observation per year,

[1] A Python-based command language for IRAF that can be used in place of the existing IRAF command language. See http://www.stsci.edu/resources/software_hardware/pyraf.

[2] See http://www.stsci.edu/resources/software_hardware/pydrizzle.

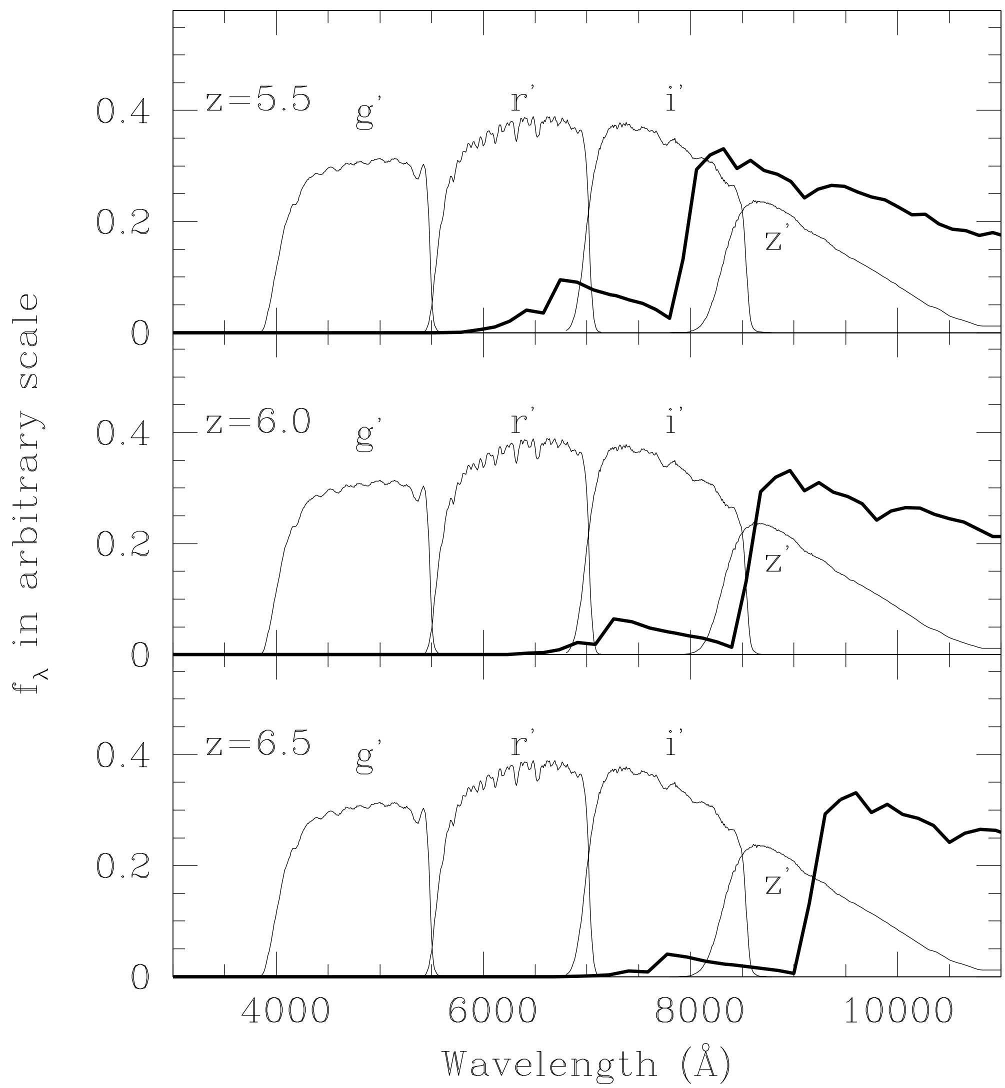

Figure 9.1: The choice of passbands for the ACS/WFC pure parallel mode is suitable for selecting $z \simeq 6$ galaxies. For simplicity, $g'r'i'z'$ is used for the passband notation. The throughput of the entire system in these four passbands are plotted in thin line, while the spectrum of a model galaxy (Bruzual & Charlot 1993), after attenuated for the cosmic H I absorbtion (Madau 1995), is shown in thick line at z=5.5, 6.0 and 6.5, respectively (from the top to the bottom). The i' and z' combination is ideal for selecting galaxies at $6.0 \le z \le 6.5$.

Table 9.1: Default ACS/WFC Parallel Observing Scheme and the S/N=5 limits

		SDSS-g		SDSS-r		SDSS-i		SDSS-z
Orbits	Int.(sec)	Limit	Int.(sec)	Limit	Int.(sec)	Limit	Int.(sec)	Limit
1	–	–	–	–	1200	27.1	1200	26.3
2	–	–	2400	27.9	1200	27.1	1200	26.3
3	2400	27.9	2400	27.9	1200	27.1	1200	26.3
4	2400	27.9	2400	27.9	2400	27.9	2400	27.1

resulting in ~ 0.5 deg^2 covered to a depth of one orbit. Among these fields, ~ 540 arcmin^2 will be covered by 2 orbits, and ~ 250 arcmin^2 will be covered by 3 orbits. The observing scheme for 1–4 orbits and the corresponding limits are summarized in Table 9.1 (see also Sparks et al 2001). The observing pattern will repeat itself if the coverage is more than 4 orbits. The statistics by the end of the year 2002 shows that the above numbers are largely correct. These parallel data provide a rich source for us to investigate the LF at the brightness level of $AB = 25$–28 mag.

9.2 Data from a Deep Parallel Field

In this part, we present our preliminary analysis of a field that is the deepest ACS/WFC parallel observation to date. The center of this field is $RA = 12^h43^m32^s$, $Dec = 11^o40'32''$ (J2000), and it is at a galactic latitude of $|b| = 74.4^o$. Although it is in the direction of the Virgo Cluster, the field contains no known bright galaxies. The primary observation of the visits is the WFPC2 imaging of NGC4647, which has a size of $2.9' \times 2.3'$ and the V-band total magnitude of 11.3 mag. As the border of the WFC is about $5'$ away from that of the WFPC2, the parallel field is not contaminated by the light from either this galaxy or its close neighbor, M60.

The observations spanned from April 28 to June 19, 2002. For some unknown reasons, the filters used in the observations did not exactly follow the convention set by the pure parallel program: only the F775W and F850LP filters were used, and the number of orbits spent on the F775W filter is nearly twice as many as that of the F850LP. In total, 15 images were taken in the F850LP-band and 27 images were taken in the F775W-band. The total exposure time in these two bands is 2.65

hours and 4.28 hours, respectively. The longer exposure and the higher system throughput in the F775W-band made the survey limit in this band much deeper than that in the F850LP-band, and therefore made the subsequent candidate search securer than the conventional equal-depth imaging.

Due to the constraints of parallel observations, planned dithering cannot be done. To make it possible to reject cosmic-ray hits, all the pure parallel data are taken with the so-called "cosmic-ray-split" (CR-split) mode, which divides the total available time of a scheduling unit into multiple exposures, or so-called "associated" exposures. For this parallel field, the smallest scheduling unit was half orbit ($\sim$ 1,000–1,100 seconds) and it was broken into two exposures (each around 500 seconds). The longest scheduling unit was one orbit ($\sim$ 2,000–2,200 seconds) and it was broken into three exposures (each around 700 seconds). The central positions and the positional angles (PA) of the images taken during successive orbits were slightly different. As the observations spanned a long period of time, this in fact provided some sort of dithering.

9.3 Reduction and Photometry

During the time when this study was carried out (August to October, 2002), the standard on-the-fly reduction pipeline for the ACS data was not matured yet. While it meant to "drizzle-combine" the associated CR-split exposures into a cosmic-ray-free stack, it did not properly identify the cosmic-rays in the single exposures. As a result, the final data product of a set of associated images, the drizzle-combined stack, was full of cosmic-rays from all the single images and was not directly usable. In the mean time, the reference files that the pipeline used to calibrate the data were also under rapid revision. The reference files used when fetching over the data were obviously not the latest reference files available at that time.

Given all these, it was decided that we started from the raw data. After fetching the raw data from the HST data archive, the CALACS task built in the latest STSDAS package (V3.0) was used to reduce those data up to the stage of flat-fielding. The reference files that the GOODS[3] team used

[3]GOODS stands for the "Great Observatories Origins Deep Survey"; see http://www.stsci.edu/ftp/science/goods.

to reduce their data (available as soon as the images were taken and put to the public domain) were retrieved and used.

PyRAF was installed to give the task PyDrizzle the working environment. PyDrizzle was run on all the individual images, not to combine them according to their associations, but only to restore them to the correct geometry. It was found that the differences among the positional angles of all these images were negligible, therefore the “ROTATION” parameter was set to “no”. Then the science extensions were extracted from the reduced data (they were in the MEF format). After this step, the individual images were in the single-FITS format and could be combined with the more conventional tasks such as “IMCOMBINE”.

After a few tests, it was found that the positional information recorded in the FITS headers of the images were not accurate enough to be directly used to calculate the positional shifts among the images. Therefore these shifts had to be obtained manually. The images were displayed on screen, and a set of common, unsaturated objects (all are of highly compact morphology; most of them are stars) were identified. The task “IMEXAME” was run interactively to determine their centers, and the positional shifts of the images were subsequently determined. The task “IMCOMBINE” was then used to combine the individual images.

After obtaining the final stacks in both the F775W and the F850LP bands, we used *SExtractor* of Bertin & Arnouts (1996) to perform matched-aperture photometry by invoking its double-input mode. The F850LP stack was used for extracting sources and defining apertures, and the magnitude of each detected source was measured on the F850LP stack and the F775W stack independently, but with a same aperture. For source detection, we used a 5×5 Gaussian smoothing kernel with the FWHM of 2.0 pixels, which is approximately the same as the FWHM of a point source PSF on both stacks. The detection threshold was set to 1.8 σ, and at least 4 connected pixels above this threshold were required for a source to be included. We used total magnitude (corresponding to the *mag-auto* option in SExtractor) for the photometry. The two catalogs were then merged into a master catalog, which we shall refer to as the "matched catalog". We adopted the zeropoints used by the Great Observatories Origins Deep Survey (Dickinson & Giavalisco 2002) team for their HST Treasury program utilizing the same instrument, where they have derived the zeropoints as one electron corresponding to $m_{775W} = 25.656$ mag and $m_{850LP} = 24.916$ mag.

We assessed the F850LP-band survey limit as the following. The representative error (Δm) reported by *SExtractor* was used to calculate the S/N of each extracted source, using the simple relation of $\Delta m = 1.0857/(S/N)$. Only the sources with $S/N \geq 5$ were included in the assessment. From the source count histogram, we estimated that the survey was 100% complete to $m_{850LP} \leq 28.0$ mag. To estimate the faintest level that the F775W-band achieved, we ran *SExtractor* independently on the F775W stack with the detection threshold lowered to $1\,\sigma$. We counted the number of detected objects regardless of their S/N, and found that the number count histogram reaches its peak value at 30.0 mag. Thus, for an object that is not detected in the F775W-band, it must be fainter than 30 mag in this band. This result will be used below.

CHAPTER 10

Candidate Search

We selected $z \geq 6$ objects via the drop-out technique that identifies the Lyman-break signature their spectral energy distributions (SED's). At $z \geq 4$, this signature, which is mainly due to the cosmic intervening H I absorption (Madau 1995), occurs at rest-frame wavelength of 1216 Å. At $z \simeq 6$, this signature moves out of the F775W-band and into the F850LP-band. As the area enclosed by the F850LP-band system response curve drops to half of the total value at around 9200 Å, this passband losses its efficiency at this wavelength. Therefore, the combination of these two filters is effective in identifying the Lyman-break in the redshift range of $6.0 \leq z \leq 6.5$. Note that the candidates found with this filter combination will be slightly less ambiguous than those found with I and z' (see Figure 9.1) because the F775W and F850LP filters hardly overlap.

10.1 Drop-out Selection

We define an object as a "F775W drop-out" if it is significantly detected in the F850LP-band but is not visible in the F775W-band. To be specific, such a source should be flagged as not detected in the F775W-band in the matched catalog, and it should have reported photometric error smaller than 0.15 mag, or equivalently, have S/N larger than 7.2, in the F850LP-band. The later constraint was rather conservative, and it was applied because at this stage we were more concerned with the reliability of the selection than its completeness at the low brightness level. At this S/N level, the survey in the F850LP-band is 100% complete to 27.5 mag.

Such criteria resulted in a candidate list of 114 objects. All these sources were then visually examined in both bands to make sure that 1) it was a real detection in the F850LP-band and 2) it was not seen in the F775W-band. This refining procedure rejected 84 objects from the list and only

30 plausible candidates remained. We found that there were a variety of reasons that gave rise to false candidates. Besides those causes commonly seen in CCD imaging (e.g., background anomaly close to the field edges due to dithering), one other important cause is the correlated background noise that is due to the geometric correction, which accounts for about 40% of the 84 false candidates.

While it maps the off-axis ACS images back to the proper geometry, the geometric correction makes the mapped pixels non-independent. As a result, the background noise in the mapped pixels is spatially correlated, and such a correlation shows up as weak, web-like structures in the background (visible in Figure 10.1). The effect of these structures is two-fold. When the object search is pushed to very faint threshold in the F850LP-band, some of these structures could be picked up as local maximum and result in false detections in this band. On the other hand, if a faint but real object is too close to such structures in the F775W-band, it could be missed by the source detection algorithm. The source detection parameters that we used to generate the matched catalog were optimized to make the detection as complete as possible while keeping the number of false objects manageable. The visual examination serves as a second safeguard procedure to keep the candidate list clean.

To independently check the reliability of these 30 candidates, we performed a simulation to test whether these objects could be recovered if they were at different places on the F850LP stack. For a given candidate, a 13×13 pixel image stamp centered on it was copied from the F850LP stack. After subtracting a constant sky background, the stamp was put at 1,000 random positions on the F850LP stack, and thus generated 1,000 artificial objects that have the same photometric properties of their prototype. *SExtractor* was then run with the same parameter setting and the number of recovered artificial objects was counted. The simulation was done for each of the 30 candidates, and we found that the median recovering rate was 88%. The recovering rate essentially remains at this level for the objects that are brighter than 28.0 mag, and drops slightly to 79% beyond this limit. Thus our candidates are deemed reliable. Table 10.1 gives the coordinates and photometric properties of all these candidates.

Table 10.1: Candidates found in the ACS/WFC deep parallel field

ID	SID	α	δ	z'
1	6	12:43:24.941	+11:41:18.54	27.805
2	8	12:43:23.939	+11:40:50.47	27.367
3	10	12:43:25.497	+11:41:15.71	27.046
4	11	12:43:26.997	+11:41:40.73	28.093
5	16	12:43:28.532	+11:41:41.64	27.485
6	19	12:43:24.588	+11:40:29.04	27.190
7	20	12:43:25.721	+11:40:44.53	27.177
8	21	12:43:29.952	+11:41:49.73	27.404
9	23	12:43:25.792	+11:40:39.37	28.170
10	28	12:43:28.713	+11:41:08.29	26.801
11	39	12:43:29.993	+11:40:50.76	27.410
12	49	12:43:30.841	+11:40:49.12	27.072
13	56	12:43:29.828	+11:40:10.91	27.333
14	57	12:43:30.624	+11:40:23.01	27.841
15	59	12:43:33.026	+11:41:01.18	27.303
16	65	12:43:34.998	+11:41:26.31	27.407
17	69	12:43:36.410	+11:41:40.54	27.771
18	73	12:43:31.636	+11:40:15.05	27.798
19	76	12:43:30.848	+11:39:56.15	28.318
20	79	12:43:32.473	+11:40:17.35	27.104
21	82	12:43:32.103	+11:40:03.53	27.265
22	85	12:43:35.515	+11:40:54.88	27.351
23	93	12:43:33.410	+11:40:03.64	27.636
24	94	12:43:32.392	+11:39:41.08	27.778
25	97	12:43:34.209	+11:39:29.08	27.527
26	98	12:43:36.697	+11:40:42.40	27.535
27	100	12:43:36.045	+11:39:43.22	27.627
28	107	12:43:32.109	+11:39:13.92	27.571
29	108	12:43:37.878	+11:40:55.62	27.471
30	114	12:43:37.278	+11:40:06.87	27.578

RA and DEC in J2000.0.

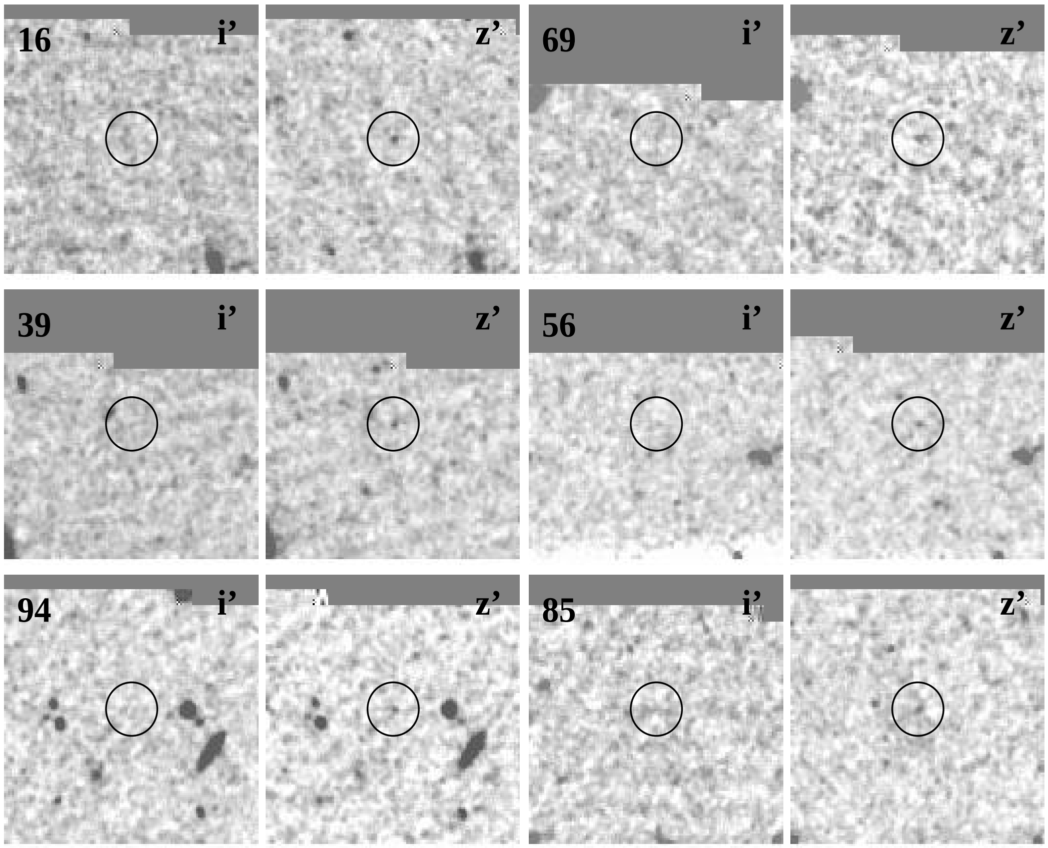

Figure 10.1: The image stamps in the F775W (labeled as i) and F850LP (labeled as z) bands for six objects that are randomly chosen from our candidate list. The images are $7'$ on a side, and have been smoothed by a 5×5 boxcar. The SID's of these candidates are label to the left of the F775W-band images, and the small circles indicate the locations of the candidates. All the 30 candidates have $S/N \geq 7.2$ in the F850LP band, and their median magnitude in this band is 27.4 mag.

Figure 10.1 shows the F775W and the F850LP images of six candidates that are randomly chosen from the 30 sources. The images have been smoothed by a 5×5 boxcar to enhance the detected sources. The F850LP-band magnitude of the 30 sources ranges from 26.8 to 28.3 mag, and only three of these sources are fainter than 28.0 mag. The median magnitude of these candidates is 27.4 mag.

10.2 Possible Sources of Contamination

The observation of this parallel field spanned 50 days, and thus is possible to detect some transient events, which might be errantly picked up as drop-outs. Given the large number of images going into the stacking process, however, any transient event was likely to be rejected during the cosmic-ray filtering process. Even if a transient was of long enough duration (a slowly decaying supernova, for example) such that it was observed on several images and was not rejected by stacking, it still would not be selected as a candidate because there is no reason for it to be observed only in the F850LP-band but not in the F775W-band. Nevertheless, to check against the slight possibility that we might have picked up some transient events as candidates, we visually examined the locations of these 30 candidates on each of the 15 individual F850LP-band images. No transient event was found on these locations. Therefore, any possible source of contamination must be of non-transient nature.

As Figure 10.2 shows, there are three types of sources whose SED could mimic the Lyman-break signature at $z \simeq 6$, namely, strong emission-line galaxies at low redshift, elliptical galaxies, and cool dwarfs in our Galaxy. Given the sharp cut-off of the F775W-band in the red and our stringent selection criteria, we argue that none of these sources is likely to seriously contaminate our candidates:

1. *Low-z emission-line galaxies* — Such galaxies should have very strong emission lines in the F850LP-band to be included by our selection criteria. The observed equivalent width W_{obs} of such an emission line can be estimated by using $W_{obs} \simeq (\widetilde{F_\nu}/f_{\nu c})D$, where D is the width of the F850LP passband, $\widetilde{F_\nu}$ is the average flux measured in the F850LP-band, and $f_{\nu c}$ is the continuum flux estimated from the F775W-band. Since D is about 1390 Å and a conservative lower limit of $\widetilde{F_\nu}/f_{\nu c}$ is 4, we get $W_{obs} > 5000$ Å. Considering that the system response of the F850LP-band drops to half of its peak value at around 8300 Å and 9700 Å in the blue and the red, respectively, the emission lines that are possible to produce the detected flux are $H\alpha$(6563 Å) at $0.26 \leq z \leq 0.48$, $[OIII]$(5007 Å) at

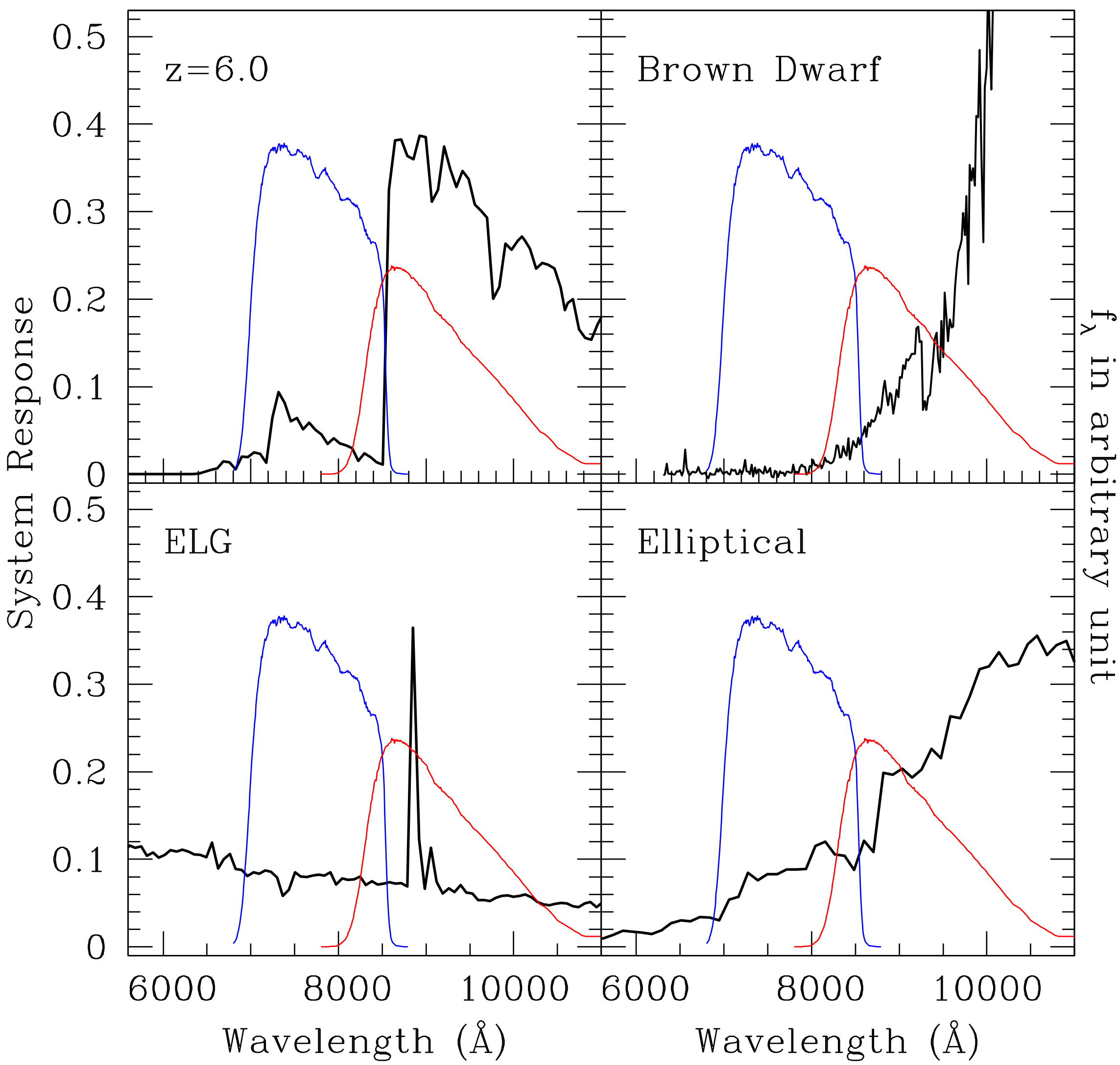

Figure 10.2: There are three types of objects whose SED can possibly mimic the Lyman-break signature of $z \simeq 6$ galaxies. They are emission-line galaxies (ELG) at $z < 2$, elliptical galaxies at $1.0 \leq z \leq 1.5$, and Galactic brown dwarfs. However, none of them is likely to severely contaminate our candidates (see text).

$0.66 \leq z \leq 0.94$ and $[OII](3727\,\text{Å})$ at $1.23 \leq z \leq 1.60$. Therefore, the smallest possible rest-frame equivalent width is still enormously high, $W = W_{obs}/(1+1.60) > 2200\,\text{Å}$. Such emission-line galaxies should be very rare, if there is reason to believe that they exist at all. Hence, it is very unlikely that emission-line galaxies would contaminate our candidates.

2. *Elliptical galaxies* — Although the 4000 Å break in the SED of an elliptical galaxy at $1.0 \leq z \leq 1.5$ occurs in between the F775W and the F850LP bands, this break is not as steep as the Lyman-break at $z \simeq 6$. The sharp cut-off of the F775W system response in the red further helps to discriminate between these two features. Convolving a typical SED of E/S0 galaxies (e.g., Coleman et al. 1984) at $1.0 \leq z \leq 1.5$ with the WFC system responses gives $m_{775W} - m_{850LP} \simeq 1.0$ mag, while the same synthesis for a model $z \simeq 6$ galaxy gives $m_{775W} - m_{850LP} \geq 2.0$ mag. Given that any object with $m_{775W} < 30.0$ mag should be detected in the F775W-band (see §9.3), all of our candidates have $m_{775W} - m_{850LP} > 1.5$ mag, among which 27 objects have $m_{775W} - m_{850LP} > 2.0$ mag. Therefore, we argue that the possible contamination rate due to elliptical galaxies is three objects at most.

3. *Cool dwarfs* — L and T type dwarfs are known to create large color discrepancy in the passbands similar to those used in this study, and it is very difficult to distinguish them without IR photometry (e.g. Fan et al. 2000). Unfortunately, we do not have any knowledge about their spatial distribution, and we have to heavily rely on very rough assumptions to estimate their contamination to our sample. Given the faintness of our candidates, it is implausible for luminous dwarfs to enter our selection, as that would put their distances far beyond the thickness of the Galaxy. The least luminous L dwarfs currently detected have absolute magnitudes at $M_I \sim 20$ mag level (e.g. Dobbie et al. 2002). For such objects to remain undetected in the F775W-band, they would have to be at a distance of 0.6 *kpc* or further. Assuming an outer bound of 1.5 *kpc* from the Sun, the volume that our field-of-view samples is approximately 880 pc^3. If we assume an IMF of the form $dN/dM \propto m^{-\alpha}$ with $\alpha \simeq 1$ and use the model of Haywood & Jordi (2002), the local number density of dwarfs is

approximately of $0.04\,pc^{-3}$. Using a scale height of 0.3 *kpc* for the Galaxy (e.g. Liu et al 2002), the number density extrapolated to a distance of 0.6 *kpc* and beyond will drop by at least a factor of ten. Thus we estimate that the contamination due to cool dwarfs is about 3–4 objects at most.

CHAPTER 11

Faint-end Constraint to the LF

Among the 30 plausible candidates, 27 have $m_{850LP} < 28.0$ mag. The remaining three objects fall in the 28.0–28.5 mag bin where the survey begins to be severely affected by incompleteness, and, as discussed above, they are also the only three objects that could possibly be elliptical galaxies (see §10.2). These three objects are not included in the discussion below.

Taking into account that we discarded the field edges and the gap between the two CCD chips, the effective survey area is approximately 10 arcmin^2. If we assume that cool Galactic dwarfs contribute 4 contaminators (§10.2), the number density at $6.0 \leq z \leq 6.5$ is 2.3 arcmin^{-2}. This result indicates that $L < L^*$ galaxies do exist in large number at $z \simeq 6$ as expected. We have predicted the number density of galaxies at $5.5 \leq z \leq 6.5$ in Yan et al. (2002) by extrapolating the LF measured at $z \simeq 3$ to $z \simeq 6$ and using the observational limits in the HDF-N as the normalization. The high-normalization case of our prediction gives a cumulative number density of 3.67 arcmin^{-2} to 28.0 mag. The co-moving volume at $6.0 \leq z \leq 6.5$ is about 48.7% of that at $5.5 \leq z \leq 6.5$ in our adopted model cosmology. Therefore, the number density that Yan et al. (2002) would predict for the $6.0 \leq z \leq 6.5$ range is 1.8 arcmin^{-2}. Figure 11.1 shows the cumulative number density prediction adapted from Yan et al. (2002), with the result from this study added. Strictly speaking, this constraint inferred from number of candidates should still be treated as an upper limit, therefore it is plotted as a downward arrow. One the other hand, if we do not underestimate the contamination rate due to brown dwarfs, this constraint can be taken as an actual data point rather than merely an upper limit. Note the observed number density thus inferred from our candidates is slightly higher than the predicted value. While the survey in the F850LP-band is complete to 28.0 mag in the matched catalog, the candidate selection is done at a much higher brightness level ($S/N \geq 7.2$) and is complete to 27.5 mag. That means the true number density at 28.0 mag could be even larger, as indicated by the one-sided error-bar.

This discrepancy could be due to the possibility that we underestimated the contamination rate of cool dwarfs, which is not possible to determine until we acquire deep IR data. However, the higher number density could also be real. If this is the case, it implies that the actual LF is slightly different from that in Yan et al. (2002). Indeed, if we increase the normalization in Yan et al. (2002) by 50%, this higher value can be explained without violating any other existing constraints to the LF. Or alternatively, if we change the assumed faint-end slope from $\alpha = -1.6$ to -2, this higher value can also be explained. The later possibility is of particular interest, as a steeper faint-end slope in the LF is what expected from the reionizing photon budget argument if star-forming galaxies are indeed the major sources of the reionizing photons.

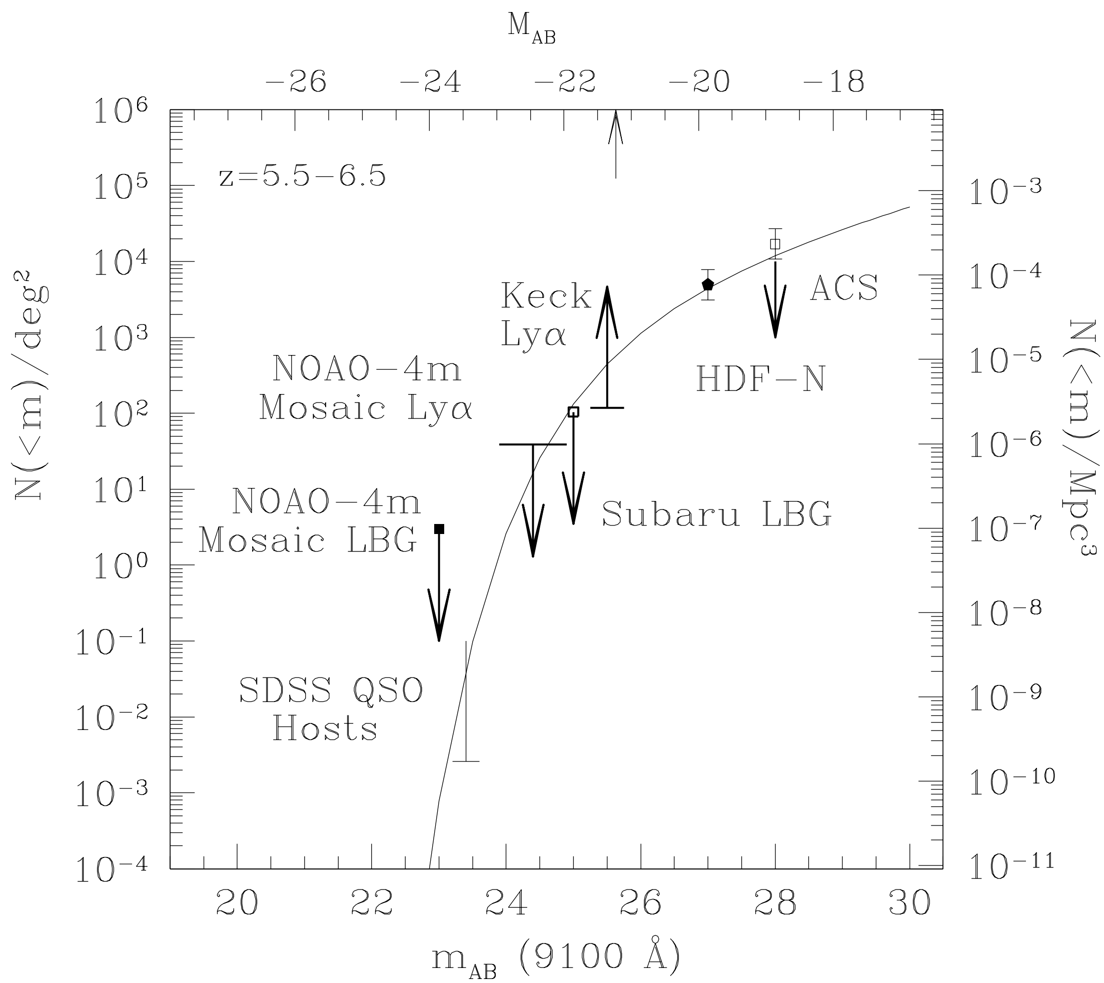

Figure 11.1: The cumulative number density of galaxies at $5.5 \leq z \leq 6.5$ inferred from the number of $6.0 \leq z \leq 6.5$ candidates found in this deep ACS parallel field is slightly higher than our prediction, as this figure indicates. If the high observed value is real, it could suggest that the faint-end slope of the LF is steeper than $\alpha = -1.6$. At present this inferred value should still be taken as an upper limit.

PART IV

A Step Toward Higher Redshift — VLT/ISAAC DATA

While now a consensus has been reached that the reionization ended at around $z = 6$, there is no observational evidence yet regarding when the reionzation *began*. To address this question, of course, requires a search of objects at higher redshifts, $z \simeq 7$ and beyond. The $p(974nm)$-band search of our NOAO 4m survey is among the first attempts toward this goal. The null result from this search is not surprising, given its relatively shallow depth. A search based on broad-band imaging data at the near-infrared (near-IR) wavelengths can reach a much deeper depth and thus is potentially more fruitful. This part presents an effort in this direction.

The major data used in this study are the broad-band JHK_s imaging data covering the central 50 arcmin^2 area of the Chandra Deep Field South (CDF-S). Obtained with the near-IR camera ISAAC at the 8m VLT telescope, these data are the deepest ground-based near-IR imaging data ever taken. Ideally, the search of $z \simeq 7$ data would be done by looking for the drop-outs in the z'-band or alike. Unfortunately, by the time when this study was carried out (August 2002) this area has no imaging data of sufficient depth in the z'-band. However, it was noticed that this field had quite a few Chandra sources that have no optical counterparts. Therefore, we aimed at locating these optically unidentified objects in these deep near-IR images and investigating the possibility of their being high-z objects by studying their near-IR photometric characteristics.

Six out of the twelve such objects that were within the coverage of these IR observations were identified in these JHK_s images, and it was found that they were more consistent with being E/S0 galaxies at $1 \leq z \leq 2.5$. It seems to be reasonable to draw the conclusion that the surface density of galaxies at $z \simeq 7$ cannot be larger than that at $z \simeq 6$, which is not surprising at all [1].

[1]The study presented in this part has resulted in a published paper (Yan et al. 2003a).

CHAPTER 12

Data Analysis

12.1 Introduction

The investigations conducted prior to the launches of Chandra and XMM have speculated that a significant fraction of the X-ray background (XRB) is produced by discrete sources, predominantly AGNs (e.g. Hasinger et al 1998). With its superb spatial resolution, Chandra resolved nearly 100% of the X-ray background in the 0.5–8.0 keV regime into discrete sources (e.g. Mushotzsky et al. 2000), and thus changed the theme of the XRB study into investigating the nature of the discrete X-ray sources and their constraints on galaxy evolution. With the active optical and infrared follow-ups around the two deepest Chandra fields, Chandra Deep Field North (CDF-N; Brandt et al. 2001b) and South (CDF-S; Giacconi et al. 2002), we have gained extensive knowledge about the faint X-ray source population. It is now generally believed that the majority of these sources are dust-obscured type-II AGNs at z=0–2, while a smaller fraction of them are classic type-I AGNs out to $z \simeq 4$ (e.g., Alexander et al. 2001; Tozzi et al. 2001; Norman et al. 2002; Rosati et al. 2002).

However, a significant number of these X-ray sources are still optically unidentified and thus their nature remains uncertain. Within an $8'.6 \times 8'.6$ area at the center of the CDF-N, the multi-wavelength investigation of Alexander et al (2001) indicates that fifteen, or about 10% of the total X-ray sources do not have counterparts to a $2\,\sigma$ limit of $I = 25.3$ mag (all magnitudes quoted are in the Vega system unless otherwise noted). Five out of these fifteen sources, however, have near-IR counterparts on the HK'-band images of Barger et al. (1999). Similarly, Giacconi et al. (2002) concluded that 59, or about 17% of the total X-ray sources in the CDF-S were not optically identified at a limit of R = 26.0–26.7 mag. These facts raise a very natural question: are these optically invisible sources merely the fainter tail of the already identified population, or do they constitute a separate population of their own? In this study, we study the nature of the optically unidentified sources in Giacconi et al. (2002), which we shall refer to as "R-unidentified sources". We utilize the deep VLT/ISAAC JHK_s and VLT/FORS1 I-band data, both of which are now publicly available from the ESO science archive.

12.2 Data

As part of the supporting observations of the *Great Observatories Origins Deep Survey* (GOODS; Dickinson & Giavalisco 2002) fields, the ESO VLT/ISAAC has imaged a large portion of the CDF-S in J, H, and K_s-bands (hereafter JHK_s). The first release of these fully processed and stacked data consists of six continuous fields, and covered about 50 arcmin^2 at the center of the CDF-S. A small portion of the data, covering ~ 6 arcmin^2 and in the J and K_s-bands only, were taken before the campaign formally began (Saracco et al. 2001). To further constrain the optical characteristics of the Chandra sources, we also independently reduced the whole set of CDF-S I-band VLT/FORS1 images (3 hours of exposure, ESO Prog. ID. 64.O-0621(A), PI Gilmozzi) retrieved from the ESO science archive. These I-band data, consisting of four slightly overlapped fields, extend ~ 150 arcmin^2 and fully cover the area that the VLT/ISAAC has imaged in the JHK_s. The photometry on both the JHK_s data and the I-band data was done by using the SExtractor routine of Bertin & Arnouts (1996).

For each ISAAC field, the JHK_s images were combined into a master stack, which was then used for extracting sources and defining apertures. While the photometry was performed on the individual passbands, a same aperture defined from the master stack was used for a given source in each passband (i.e., "matched-aperture photometry"). For source detection, we used a 5×5 Gaussian smoothing kernel with the FWHM of 2.5 pixels, which is approximately the same as the FWHM of a point source PSF ($\sim 0.5''$) on the master stack. We set $1.5\,\sigma$ as the detecting threshold, and required at least 5 connected pixels above the threshold for a source to be detected. As the vast majority of the sources are extended, we used total magnitude (corresponding to the *mag-auto* option in SExtractor) for the photometry on the individual passbands. The zeropoints recorded in the image headers were used to convert counts into Vega magnitudes. The RA and DEC positions of the sources were derived by using the WCStools of Mink (1999) based on the astrometric solutions (tied to the USNO-A.2 catalog) provided in the headers of the individual images.

We assessed the JHK_s limits in the following way. The representative error reported by SExtractor was used to calculate the S/N of each extracted source, assuming the reported magnitude error (Δm) and the S/N follow the simple relation as $\Delta m = 1.0857/(S/N)$. Only the sources with $S/N \geq 3\,\sigma$ were included in the assessment. The source count histogram was constructed for each band, and the magnitudes at which the counts dropped to 50% of the peak values were defined as the survey limits. These numbers are: J=24.2, H=23.4 and K_s=23.2 mag[1].

Source detection and photometry on the I-band stacks were done in the same manner as in analyzing the ISAAC data excepted that the detection threshold was lowered to 1σ to include as faint sources as possible. As the ESO Imaging Survey (EIS; Arnouts et al. 2002) covered the entire CDF-S, we used their I-band source catalog to calibrated our photometry. We first removed the Galactic extinction (A_I=0.02 mag) that they applied to their results, and converted the magnitudes from AB system, which they used, to Vega system by using $I_{vega} = I_{AB} - 0.48$. The survey limits, derived in the same way as in the ISAAC data analysis, are approximately 25.1 – 25.2 mag accounting for field-to-field variation.

12.3 Source Cross-matching

Out of the 346 Chandra sources, 77 have their locations falling within the JHK_s coverage, among which twelve are R-unidentified sources. We found that six of these twelve objects could be matched with the JHK_s sources within a matching radius of 1.5”, all of which were strikingly significant detections (at 3.5–9.0$\,\sigma$ level) in the K_s-band. After visually examining these matched

[1]Translated into the AB system, these numbers are roughly J=24.9, H=24.7 and K_s=25.1 mag.

Table 12.1: The six R-unidentified objects in the CDF-S

ID[a]	RA & DEC (J2000)[b]	I^c	J^d	H^d	K_s^d	P/E [e]	HR[f]
79	3:32:38.04 -27:46:26.2	> 25.1	23.21±0.23	21.88±0.17	20.95±0.12	P	-0.42
593	3:32:14.79 -27:44:02.5	24.86±0.18	22.97±0.21	21.66±0.14	21.18±0.13	E	-1.00
221	3:32:08.91 -27:44:24.8	> 25.1	25.08±0.66	22.41±0.21	21.83±0.17	P	-1.00
515	3:32:32.17 -27:46:51.5	> 25.1	24.68±0.76	22.91±0.27	21.90±0.21	E	0.41
561	3:32:22.44 -27:45:43.8	> 25.1	25.73±0.86	23.49±0.38	22.68±0.29	E	-1.00
201	3:32:39.06 -27:44:39.3	> 25.1	24.79±0.58	22.62±0.21	21.52±0.16	...	-0.06

a. Source ID as in Giacconi et al. (2002; their XID).
b. RA and DEC as measured on the JHK_s images.
c. The "auto" magnitude (Kron magnitude) as derived by SExtractor, in Vega system.
d. Same as c; aperture used for each source is the same in all these three bands.
e. Point (P) or extended (E) source, based on the K_s-band images, on which a point source has a FWHM of only ~ 0.5".
f. X-ray hardness ratio (HR), defined as (H-S)/(H+S), where H and S are the counts in the hard and soft channel, respectively. Values are taken from Giacconi et al. (2002).

sources on screen and comparing against the R-band image stamps given in Giacconi et al. (2002), we concluded that these six IR counterparts were real identifications. One more object might also have been matched, but it is rather uncertain as its image lies exactly at the edge of the field, and thus is not included in this study.

We then cross-matched the R-unidentified sources with our I-band images. While 35 of them have their locations within the I-band coverage, only one counterpart was found. This fact further suggests that most of these objects are indeed optically faint. However, the only counterpart, which is also one of the six JHK_s sources, was detected at above $7\,\sigma$ level.

Table 12.1 lists the positions and the photometric characteristics of the six objects that we identified, together with their X-ray hardness ratios (HR) taken from Giacconi et al. (2002). These six sources are of moderate X-ray fluxes in 0.5–2 kev, with two of them falling toward the faint end ($\sim 8.5 \times 10^{-17}$ erg/s/cm^2). We note that they tend to have negative X-ray hardness ratios. In fact, three of them were detected in the soft channel only ($HR = -1$). Assuming that their underneath X-ray sources are AGNs, it is possible to determine their types based on their HR values. If we use $HR \simeq -0.1$ as the dividing line between low X-ray luminosity (L_X) type-II AGN and high L_X

type-I AGN (e.g. Rosati et al. 2002), three of these six Chandra sources are type-I AGNs while the remaining two are type-II AGNs. However, such a division should be used with caution here, as our case is of small number statistics (cf. Fig. 3 of Rosati et al. 2002). The excellent image quality (point source FWHM $\sim 0.5''$ in both IR and I-band) allowed us to at least determine if these sources are of extended morphology. Based on the K_s-band image, where the S/N of the objects is the highest, we determined that three of them were extended sources, and two of them were point sources. The remaining one is hard to tell because it is close to the K_s-band field edge and its background is much noisier than that of the others.

CHAPTER 13

Nature of the Six IR Counterparts

13.1 Possible Explanations

Although these R-unidentified sources could simply be the fainter tail of the brighter objects that have been optically identified, we should not limit our investigation to only this possibility. For this reason, we should consider a wide variety of candidates when exploring the nature of these X-ray source hosts.

As Alexander et al. (2001) argued, it is very unlikely that the objects in the Galaxy could be a major contribution to optically faint X-ray sources. This possibility is even smaller for the CDF-S because it is at high galactic latitude. Thus we consider four types of extragalactic objects as the primary candidates, namely, elliptical galaxies (E/S0), AGNs/QSOs (AGN), irregular galaxies (Irr), and very young galaxies at high redshift ($z > 5$; High-z). We do not include spiral galaxies for the sake of simplicity, as their photometric properties in the I-band and the near-IR lie in between the ellipticals and the irregulars. We compare the six IR counterparts against these four types of candidate in the $IJHK_s$ color space. We consider the redshift range of $5 \leq z \leq 10.5$ for high redshift young galaxies, and $0 \leq z \leq 5$ for all the other three types of candidates. We also consider the effect of internal dust extinction of A_V=0.1–3 mag, following the standard Milky Way extinction law. For the wavelength range shortward of 2000Å, we use the average values of the LMC, SMC and the Galaxy (e.g. Calzetti, Kinney & Storchi-Bergmann 1994).

13.2 Color-Color Diagram Diagnosis

Because five of these six objects are only visible in the three IR passbands, it is not realistic to perform rigorous photometric redshift analysis based on such limited information. At this stage, we chose to use color-color diagrams as our primary diagnostic tools, which are less quantitative but more robust. The invisibility of these sources in the R-band and blueward was used as a consistency check for each of the four possibilities, and was also used as one of the inputs (detailed below) to constrain the rest-frame luminosity of the sources.

We simulated the colors of the candidate objects by using their representative spectral templates. The templates for E/S0 and Irr were taken from Coleman, Wu & Weedman (1980) with the extension to UV and IR according to Bruzual & Charlot (1993), and the one for AGN was taken from Vanden Berk et al. (2002; using $f_\lambda \propto \lambda^{-0.45}$ to extend its continuum to the near-IR). For young, high redshift galaxies, we used a 0.1 Gyr age, solar metalicity template from Bruzual & Charlot (1993). These rest-frame spectral templates were redshifted in Δz=0.5 step, and attenuated for the cosmic H I absorption according to Madau (1994). The resulting spectra were then convolved with the system responses, mainly the filter transmission and the detector quantum efficiency, to generate colors in the AB magnitude system. When considering dust extinction, the colors were adjusted according to the rest-frame spectral range sampled by the relevant passbands. The colors were finally transfered into the Vega system by adopting the appropriate zeropoints (e.g. Waddington et al. 1999).

Figure 13.1 shows the $(H - K_s)$ vs. $(J - K_s)$ color-color diagrams in four separate panels for the four cases. The field objects with $S/N \geq 3$ in all three bands are shown as the green dots, and the Chandra sources that have been identified in R-band are shown as the blue squares. The six IR counterparts are plotted with different symbols based on their hardness ratios: the three solid triangles are the ones with $HR = -1$, the two open hexagons that have $-1 < HR < 0.1$, and the open square is the source that has $HR > 0.1$. Their error bars indicate the photometric errors in their colors, which are calculated as the square-root of the quadratic sum of their photometric errors in the corresponding passbands. The unreddened and reddened colors of the simulated objects at different redshifts are plotted in black crosses and solid red squares, respectively (in the case of E/S0, only unreddened colors are shown). For clarity, only the optimal results are plotted for the

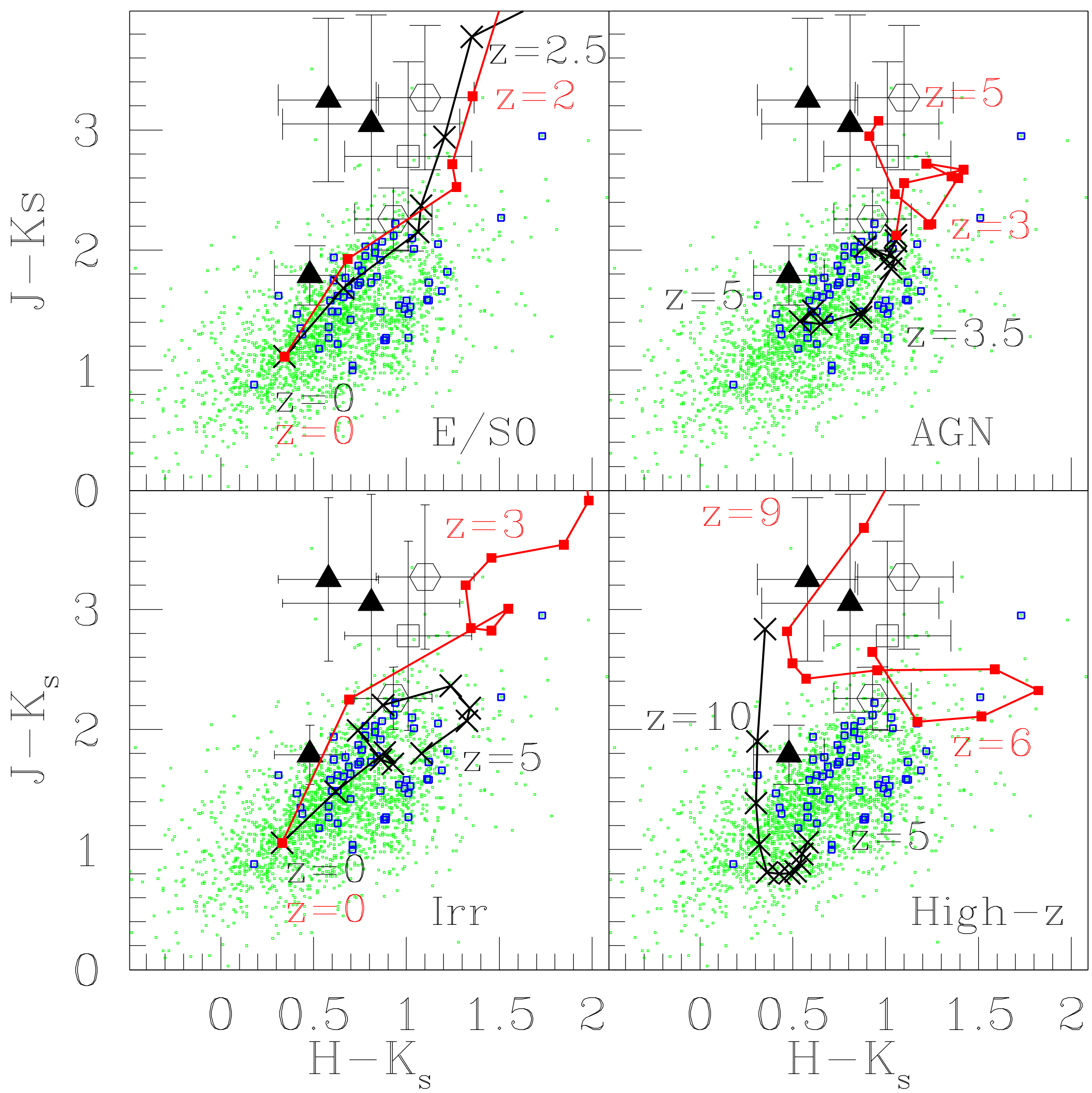

Figure 13.1: $(H - K_s)$ vs. $(J - K_s)$ color-color diagram as the diagnostic tool of the source nature. The green dots are the field objects. The open blue squares are the optically bright Chandra sources, whose locus shows clear bifurcated structure. The large symbols with error bars are the six R-unidentified Chandra sources that were identified in the IR: the three solid triangles are the sources with HR=-1, the two open hexagons are the ones with HR<-0.1, and the open square is the source d with that has HR>-0.1. Their colors are compared against the simulated colors of four types of candidate in separate panels. The redshift ranges considered are $0 \leq z \leq 5$ for E/S0, Irr and AGN/QSO, and $5 \leq z \leq 10.5$ for High-z. Dust extinction ranging from A_V=0.5 to 3.0 mag is also considered. For clarity only the cases with the optimal amount of dust extinction are shown (A_V = 0.5 mag for E/S0, A_V =1.0 mag for AGN/QSO and High-z, and A_V =1.6 mag for Irr). The unreddened colors of these simulated objects are shown as black crosses, while their reddened colors are show as filled red squares. A couple of redshifts are also marked (in both unreddened and reddened situations) to indicate the direction on which the colors change with the redshifts.

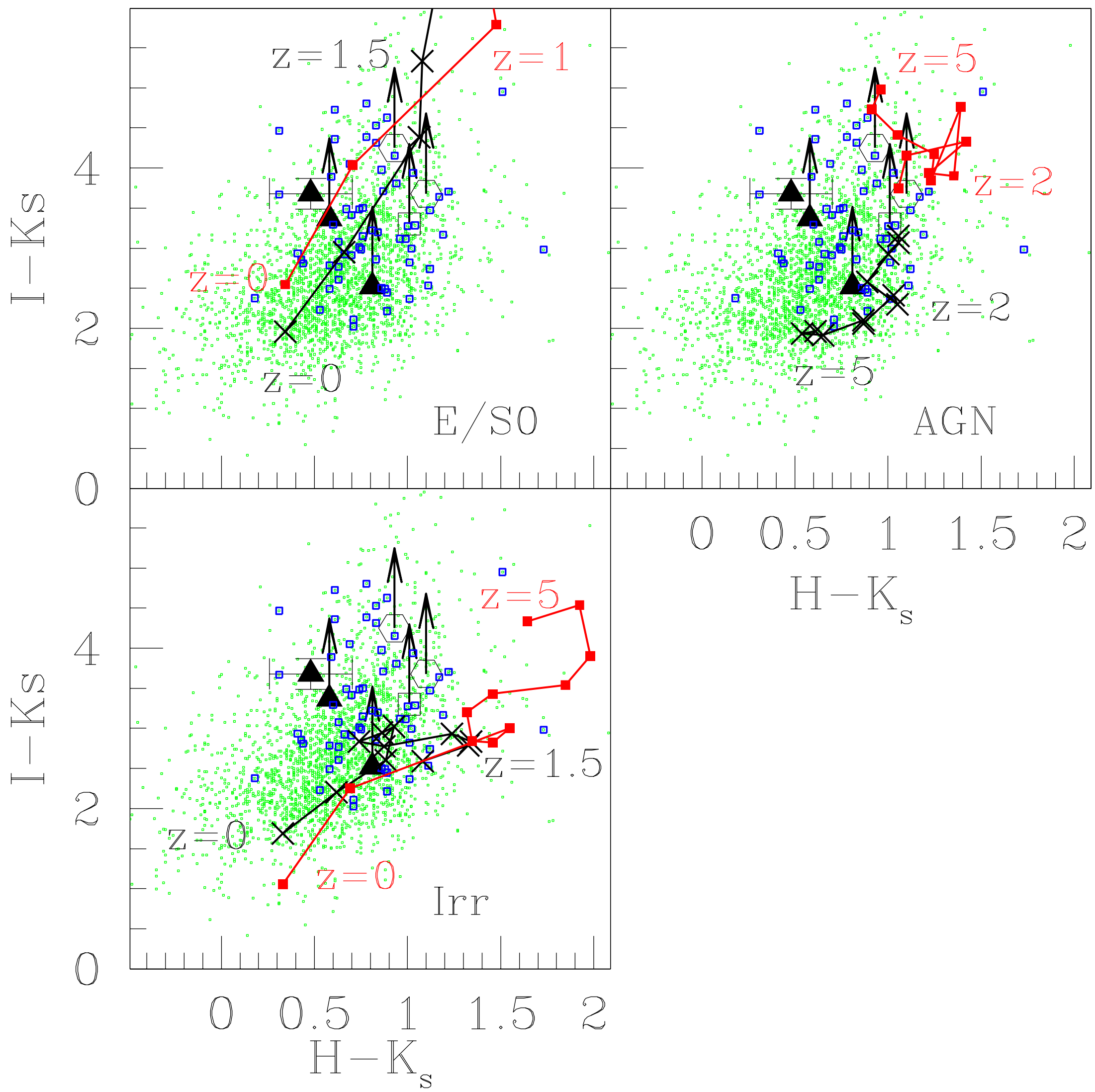

Figure 13.2: Same as previous figure, but for the $(I - K_s)$ vs. $(H - K_s)$ color-color diagram. The High-z case is not shown, as it cannot put further constraint on the $(I-K_s)$ of the six IR counterparts (see text). The arrows indicate the lower limit of the $(I - K_s)$ color for the five objects that were not detected in the I-band. Very importantly, the case of irregular galaxies does not pass this test because the $(I - K_s)$ of such objects are not consistent with the colors of the IR counterparts, even considering the effect of dust extinction.

reddened colors. These optimal reddening values are $A_V = 1.6, 1.0$ and 1.6 mag for Irr, AGN and High-z cases, respectively. A couple of redshifts are marked to indicate the direction along which the color of the simulate objects changes with redshift.

Similarly, Figure 13.2 shows the $(H - K_s)$ vs. $(I - K_s)$ color-color diagrams. The High-z case is not included in this figure, because galaxies at $z > 5$ will *drop-out* from the I-band and thus they cannot put meaningful $(I - K_s)$ constraint on those IR counterparts that are also I-band drop-outs. All the legends are the same as in Figure 13.1, except that the five of the six IR counterparts that were not detected in the I-band are not plotted with error-bars. Instead, we put upward arrows on them to indicate their $(I - K_s)$ color limits.

It is intriguing to note that the location of those optically visible Chandra sources in the IR color space is bifurcated, as can be clearly seen in Figure 13.1. The upper branch coincides with the E/S0 track from $0 \leq z \leq 1.5$ while the lower branch seems to be consistent with the AGN track from $0 \leq z \leq 3.5$. This interpretation does not conflict with the investigation on the brighter sources in Rosati et al. (2002; their Fig. 5.). The six objects that we identified lie on the upper branch and its extension following the E/S0 track up to $z \simeq 2.5$ (see below).

13.3 Comments on Individual Cases

Using the two color-color diagrams and the source brightness, we are able to set stringent constraints on the nature of these six IR counterparts. We comment on the above-mentioned four possibilities individually.

1. $E/S0$ From Figure 13.1 and Figure 13.2 it is obvious that the six sources have colors consistent with unreddened E/S0 galaxies at z=0.5–2.5, and introducing internal extinction does not improve the fit. Considering the brightness of these objects, this interpretation is also consistent with their invisibility in the R-band and blueward. While No. 593 (the lowest triangle in Figure 13.1), which was detected in the I-band as well, is probably at z=0.5, the other five objects are likely at $1.0 \leq$

$z \leq 2.5$. If we use z=2.0 as their representative redshift, their averaged rest-frame V-band absolute magnitude is $\sim M_V$ = –20.1 mag (in AB system), indicating that they are giant ellipticals. In contrast, No. 593 has only $M_V \simeq -16.7$ mag if it is at z=0.5, falling in the dwarf elliptical regime.

2. *AGN* While they can reasonably explain the colors of the optically bright Chandra sources, unreddened AGNs at $0 \leq z \leq 5$ cannot produce colors similar to the six sources (see especially Figure 13.2). If internal reddening is introduced, the matching will be improved. However, this interpretation involves both the extinction and the redshift as free parameters, and requires both of them be adjusted for each source individually. If the extinction is forced to be fixed, the best fit is obtained with $A_V = 1.0mag$, which allows three of the six source (open symbols) to be explained, i.e., at $z \simeq$ 0–1 or $z \simeq$ 4–5. If we take the first interpretation for these *three* objects, their absence from I-band and blueward means they can only be at $z \simeq$ 0.8–1.0 to have a reasonable intrinsic luminosity that still qualified for AGNs (M(3800–4200$\AA$) ~ -18 to -19 mag after de-reddening). If the later interpretation is real, on the other hand, their absolute magnitudes make them fall in the low-luminosity end of QSOs (M(3800–4200$\AA$) ~ -23 to -24 mag after de-reddening). The cumulative QSO surface density inferred from this interpretation (2–3 in 50 $arcmin^2$) is consistent with the QSO luminosity function extrapolated from that is known at lower redshifts (e.g. Boyle et al. 2000). Particularly, we noted that No. 593 did not fit in this interpretation no matter how the extinction and the redshift were adjusted.

3. *Irr* Similar to the AGN case, the colors of unreddened irregular galaxies match the optically bright Chandra sources but cannot match those of the six R-unidentified sources. Introducing internal reddening cannot solve the problem, as Fig. 2 shows. Thus irregular galaxies are not likely a viable explanation to the nature of the six sources.

4. $High - z$ The colors of unreddened high-z galaxies are not consistent with the six sources. Fine-tunning internal reddening value can produce a reasonable fit either at the redshift range $7.5 \leq z \leq 8.5$ or at $5.0 \leq z \leq 5.2$. The reddening value thus required is $A_V \simeq 1.0$ mag. However,

in either case, the cumulative surface density of such galaxies are at least one order of magnitude higher than a reasonable luminosity function would predict (following the same methodology as in Yan et al. 2002). Thus we conclude that this hypothesis is not a viable interpretation either.

PART V

CONCLUSION

CHAPTER 14

Reliability of the Prediction

14.1 Summary on the LF

By extrapolating from the observed Schechter-function-type LF of galaxies at $z \simeq 3$, a simple prediction of the LF at $z \simeq 6$ was made. The major assumption of this prediction is that the characteristic luminosity at $z \simeq 6$ is still the same as that at $z \simeq 3$. Or in other words, the possible evolution of the LF from $z \simeq 3$ to 6 is largely density evolution. The normalization of the LF was fixed by the fact that *so far* there is only one spectroscopically confirmed galaxy at $z > 5.5$ in the entire HDF-N to a depth of AB $\simeq 27$ mag. While this is an observational fact, we still do not know how complete it is. Nevertheless, a lower limit can be obtained by simply take this fact at its face value. The corresponding normalization of the LF is what we refer to as the *low normalization* case. Given the fact that the search based on the deep NIC3 observation covering a smaller portion of the HDF-N resulted in this and only this object, another limit can be obtained, i.e., one $\simeq 6$ galaxy within the entire NIC3 FOV. The corresponding normalization of the LF is what we refer to as the *high normalization* case. The faint-end slope of the LF was fixed by directly taking over the slope at $z \simeq 3$, as there was no strong indication that it was otherwise by the time when the prediction was made.

The limited observations available before this thesis work was carried out suggested that the high normalization case agreed well with all the constraints, while the low normalization case could be rejected. In a $\Omega_M = 0.3$, $\Omega_\Lambda = 0.7$, and $H_0 = 65\, km \cdot s^{-1} \cdot Mpc^{-1}$ universe, the three parameters [1] of our best-guess Schechter LF at $z \simeq 6$ are: $M_{AB} = -21.23$ mag, $\Phi^* = 3.01 \times 10^{-4} Mpc^{-3}$, and $\alpha = -1.6$. Note that the magnitude is defined at the rest-frame spectral range of $\sim$ 1300–1400Å,

[1] As the Φ^* value is derived inversely based on the cumulative number density, it slightly depends on the magnitude bin size used.

and thus is referred to the continuum brightness level at observed frame at around 9100Å at $z \simeq 6$. This LF is broadly consistent with the lower limit derived based on the $z = 5.74$ galaxy found by Hu et al. (1999) in 30.33 arcmin^2 to a limit of m_{AB}=25.5 mag, and the lower limit derived based on the $z \simeq 6$ quasars found in the SDSS (Fan et al. 2000b, 2001) by assuming a reasonable relation between the quasar luminosity and the quasar host galaxy luminosity.

This thesis work put three additional constraints to the LF. Our 1 deg^2 survey with the MOSAIC cameras at the CTIO/KPNO 4m telescopes enabled a search to a depth of m_{AB}=23.0 mag from 8000–9200Å in three intermediate bands. Only one Lyman-break candidate was found, and the inferred cumulative number density upper limit at 23.0 mag is consistent with our prediction. The Lyα candidates probed a continuum magnitude limit of 1.4 mag fainter, and the inferred upper limit is also consistent with the prediction. As the number density at such a bright level is very sensitive to the L^* value, future spectroscopic identification of the candidates found in our survey is important to further narrow down the possible range of the L^* and to investigate the luminosity evolution of the LF.

A constraint at 25.0 mag level was derived based on the deep Subaru data which were recently made publicly available. The inferred upper limit of the cumulative number density at this level is slightly higher than our prediction (but still agrees with it to within 20%). All these candidates are of sufficient brightness that spectroscopic identification, although challenging, is possible with existing instruments.

The strongest constraint to the very faint end came from a deep ACS parallel field, based on which a search to a limit of 28.0 mag was conducted. Since the contamination rates due to all possible contaminators could be rather quantitatively estimated because of the stringent selection criteria, we statically obtained a number density that should be very close to the true value. This inferred number density is broadly consistent with our prediction, and more importantly, it suggests that the number density at this faint level could be slightly higher than our prediction. One possibility could be that the faint-end slope is actually steeper than $\alpha = -1.6$, and one application of this possibility will be discussed in Chapter 15.

14.2 Comparing with the LALA Survey

The Lyα candidate search of our intermediate-band survey is most close in nature to the Large Area Lyman Alpha (LALA) Survey (Rhoads et al. 2000). This narrow-band imaging survey was previously designed to select strong Lyα emitters at $z \simeq 4.5$, and was later added two narrow-band filters targeting two windows at $z \simeq 5.7$ (Rhoads & Malhotra 2001). The survey was carried out with the MOSAIC-I at the KPNO 4m. The two narrow-band filters center on 815nm and 823nm, respectively, and both have a width of 75Å (FWHM). The survey area is one MOSAIC field, but the effective area is $\sim 30'$ in diameter due to the deterioration in bandpass specification outside of this circle. The major selection criterion is narrow-broad color index < -0.75 mag. The broad-band images used are the B_W, R and I images of the NOAO Deep Wild-Field Survey, and their own V-band image. The criterion used to secure the selection against lower redshift interlopers is that the candidates should remain undetected in the B_W and V-band images at 2 σ level or below. In total, 11 candidates were selected in the 815nm filter and 7 were selected in the 823nm filter. Four of these candidates have been taken spectra at the Keck1 telescope, and three of them were confirmed with redshifts of $z \simeq 5.7$ (Rhoads et al. 2003). While some of the photometric properties of these three objects were listed in Rhoads et al. (2003), the photometric information of all the other candidates can only be read off from a "mini-spectrum" figure in Rhoads & Malhotra (2001; their Figure 1).

Compared with our results in the HDFN01 and HDFN02 fields, which were obtained with the same instruments (MOSAIC-I + KPNO 4m), their findings are somewhat surprising.

First of all, their survey limits in the narrow-band filters are surprisingly deep. The total exposure time in the 815nm filter is 9.85 hours, while in the 823nm filter is 9 hours. The quoted 5 σ flux thresholds used to identify candidates at $z \simeq 5.7$ were 0.455 μJy at 815nm and 0.405 μJy at 823nm.

In terms of AB magnitudes, these are 24.75 and 24.88 mag, respectively. For simplicity, we take only our $m(802nm)$-band results in the HDFN01 field for comparison. From the $m(802nm)$-band source count histogram of this field shown in Figure 6.1, one can see that the count drops to almost zero at 23.5 mag.

The FWHM of the $m(802nm)$ filter is about 167Å, which is 2.2 times as wide as the LALA narrow-band filters. The peak transparency of our filter and their filters are all about 90%. The CCD Q.E. of KPNO MOSAIC is 68% and 56% at 800nm and 850nm, therefore slightly favors our filter. Our total integration time is 4 hours. The sky transparency condition during the course of observations was very good. The moon phase (around first quarter) and the seeing condition (around $1.2''$) of our observations were all similar to those of theirs. The gain in our wider bandwidth (a factor of 2.2) should largely compensate the loss in exposure time (a factor of 2.46 for the 800nm filter and a factor of 2.25 for the 850nm filter). Yet their survey depth seems to be at least one magnitude deeper than ours, which is surprising. Our filters, like theirs, are all devoid of bright night-sky emission line. Even the slight difference in this regard, plus the slight difference in the moon illuminating condition, cannot account for the discrepancy in survey depth. The only other possibility is the differences of telescope mirror cleaning condition between the two runs. But even a reduction by a factor of two in throughput in our run (which is not very likely) cannot account for such a discrepancy, either.

Given our stringent calibration procedures for the HDFN01 field, and also the consistent results obtained by the cross-checking on the broad-band images of the deep Subaru data, we are confident that the absolute flux zeropoints of the HDFN01 field are accurate to about 0.02 mag. For further verification, we checked some of the broad-band images of the NDWFS. As mentioned above, the LALA Survey used the broad-band images of the NDWFS as their continuum images. Four of the NDWFS fields (the Boöte region) are now publicly available. Although none of these fields is the LALA field, they are all very close to it. SExtractor was run on the I-band stacks of all these four fields, using the same parameter settings as those used for our NOAO survey images. The source count histogram thus constructed are shown in Figure 14.1. The magnitudes of the NDWFS are tied to the Kron-Cousins system, which can be roughly converted into the AB system by using $I_{AB} = I + 0.43$. Therefore, the source count drops to almost zero at around AB magnitude of 24.4. The FWHM of the total system response in this band is about 1240Å (the FWHM of the filter alone is around 1950Å), which is 7.5 times as width as our filter. Taking both the higher CCD Q.E. in the bluer part of the I-band and the less bright sky-background in our filter into account, our survey limit is consistent with the NDWFS limit, which makes the depth discrepancy between our survey and the LALA Survey even more difficult to understand.

Nevertheless, it is worthwhile to compare the LALA result and our predicted LF. To make such a comparison, we need both their cumulative number density corrected for the survey volume and the 9100–9800Å continuum magnitudes of their objects. Their filters can only pick up Lyα emission from $z = 5.70 - 5.78$. The co-moving volume of their survey is $1.79 \times 10^5\, Mpc^3$ for their 0.20 deg^2 sky coverage. Our model uses $5.5 \leq z \leq 6.5$, giving a co-moving volume of $2.15 \times 10^6\, Mpc^3$ for the same sky coverage. Since their survey volume is only 8% of this, the 18 objects that they detected should only account for 8% of the total galaxies in our prediction.

The continuum magnitudes of these objects were not explicitly given in their paper, therefore we use the equivalent width of the weakest object to estimate their survey limit in terms of continuum magnitude. Using the numbers from Figure 1 of Rhoads & Malhotra (2001), we find that the weakest emitter has $f_\nu(line) = 0.48\ \mu Jy$ in the line, or equivalently $m_{AB}(line) = 24.70$ mag, almost approaching their detection limit. Using the approximation that $f_\nu(line)/f_\nu(continuum) = (W/\Delta\lambda) + 1$, where W is the equivalent width and $\Delta\lambda$ is the bandwidth, we find that $f_\nu(continuum) = 0.23\mu Jy$, or $m_{AB}(continuum) = 25.50$ mag. At this brightness level, our model gives the cumulative surface density of only 0.138 per arcmin^2, or 98 objects within the LALA FOV. Corrected for the co-moving volume, we predict 8 objects for the LALA Survey. If the success rate is actually as high as Rhoads

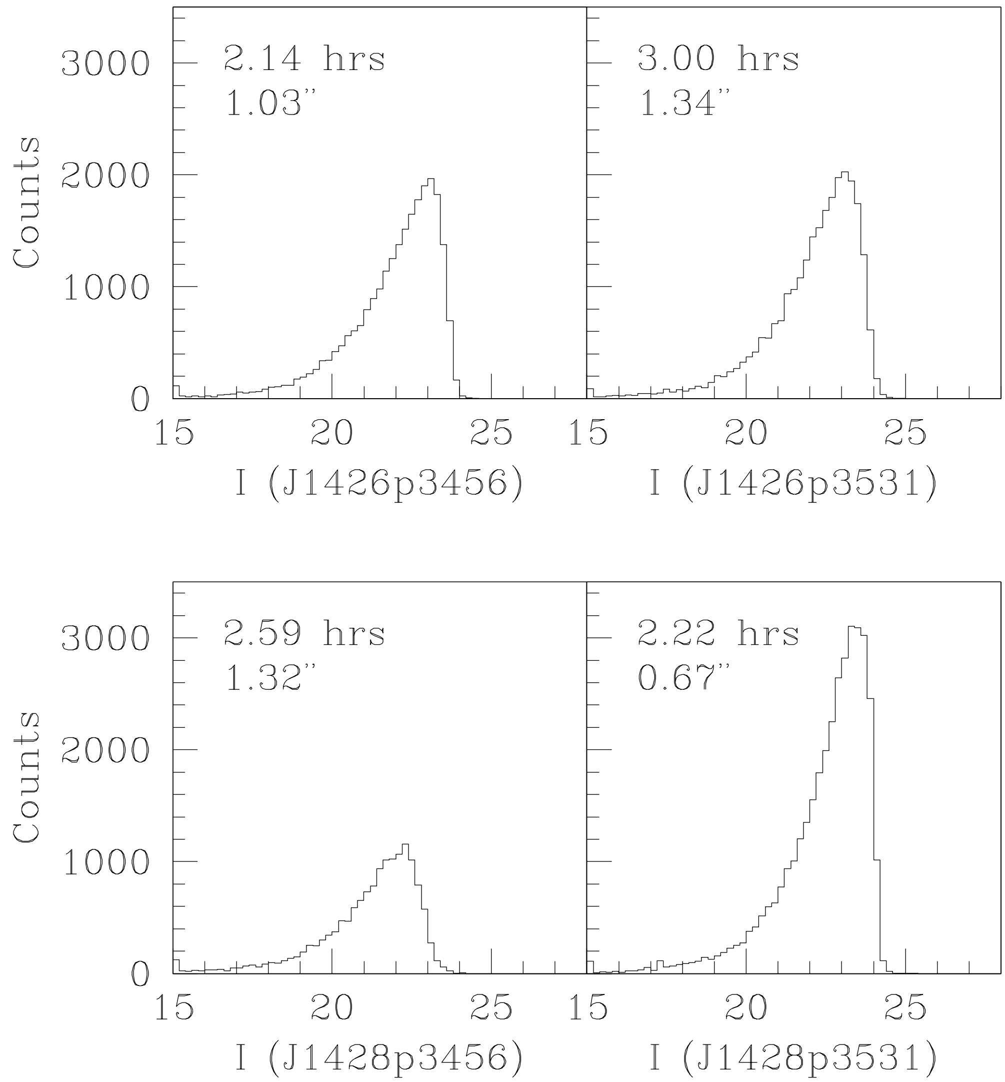

Figure 14.1: The source count histograms of the the *I*-band stacks of the four NDWFS fields whose data are now publically available. Although none of these fields is the one on which the LALA Survey targeted, they are very close to it. The source detection was done in the same way as in Chapter 6 and with similar parameter settings. The total exposure time and the seeing of each field are also marked. Note that the magnitudes are in the Kron-Cousin system, and a correction of 0.43 mag should be added to converet them to the AB system. The bin size of these histograms is 0.5 mag.

et al. (2003) suggested (3 out of 4), 13–14 of their candidates would be actually at $z \simeq 5.7$, which suggests that our prediction underestimates the number density by a factor of 1.6. While this might not seem to be a large enough difference to be alarming, the actual discrepancy is likely much larger because those LALA candidates are all strong emitters, and they are likely only a small fraction of the entire population. If we use the fraction of galaxies showing Lyα emission line (not necessarily strong Lyα emitters) in the Lyman-break galaxies at $z \simeq 3$ (Steidel et al. 1999), which is about 25%, the inferred number density of the total population would give an even higher discrepancy.

Figure 14.2 compares the result from the LALA survey with our prediction. To avoid overlapping of symbols, the LALA data point is plotted as the intersection of the two dotted line shown in the graph. Clearly, this data point is much higher than our prediction. Note that changing the faint-end slope cannot cure this problem. Adjusting either the M^* value or the normalization in our model cannot make the discrepancy disappear without violating other limits. While the nature of this discrepancy is not understood, one possibility is that galaxies at $z \simeq 6$ are highly clustered and the LALA survey happened to observe an over-dense region.

14.3 Comparing with the Subaru Deep Field Survey

One of the most significant discoveries announced since January 2003 is the two Lyα emitters at $z \simeq 6.5$–6.6 found by Kodaira et al. (2003) in the Subaru Deep Field (SDF; note that these data are different from the Subaru data used in this thesis, which were taken centering the HDF-N).

The candidates were pre-selected by using narrow-band imaging at the Subaru telescope with the Suprime-Cam. The images were obtained through a filter with FWHM of 132Å and centered on 9196Å. The total exposure time is 5 hours. The continuum image was the deep (5.8 hours) z'-band image of the SDF, and its i' image (4.7 hours) was also used to check against the lower redshift interlopers. Within an effective area of 814.3 arcmin^2, 73 candidates were selected. In a subsequent spectroscopic identification of 9 of these candidates (with the FOCAS spectrograph at Subaru), two

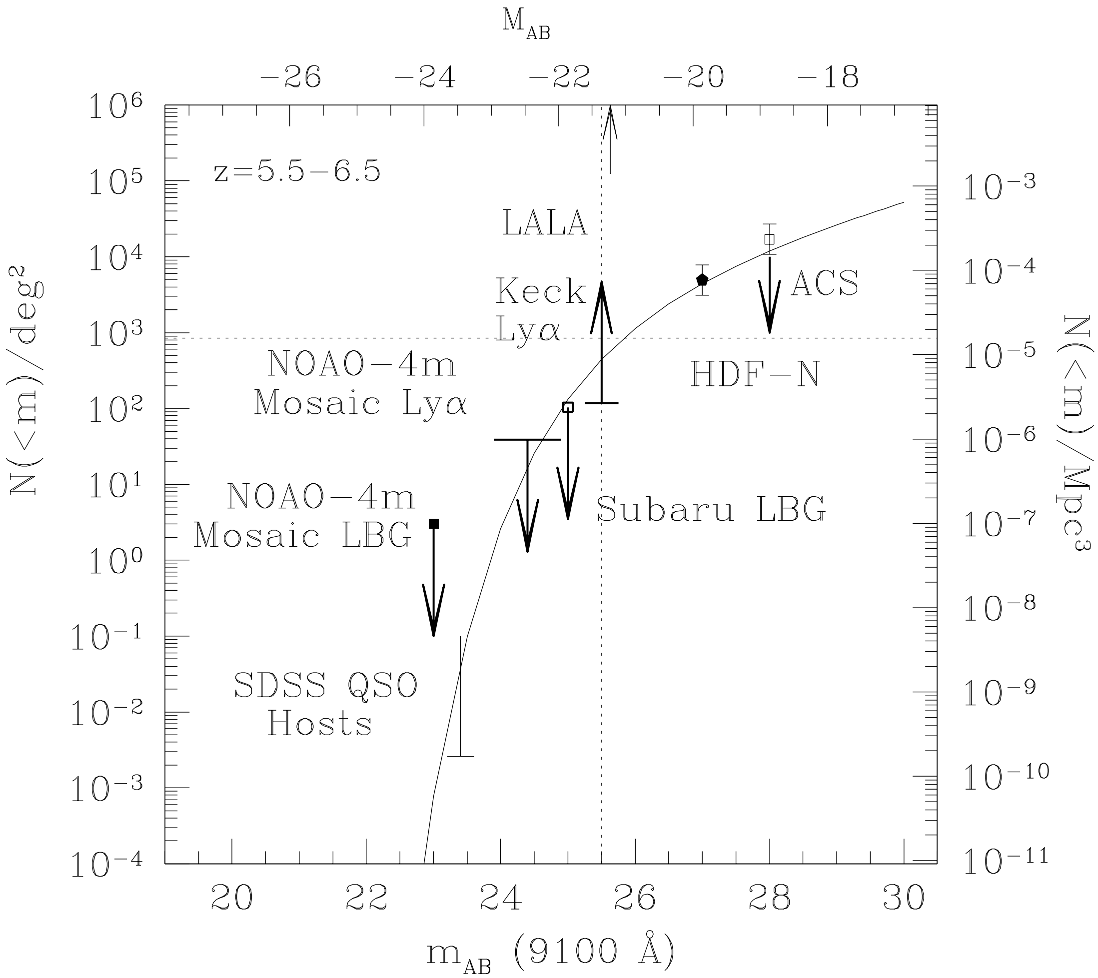

Figure 14.2: The narrow-band search of the LALA survey has resulted in 18 candidates of strong Lyα emitters at $z \simeq 5.7$ in 0.2 deg^2 (Rhoads et al. 2000). Among the four candidates that have been spectroscopically observed, three were confirmed to be at $z \simeq 5.7$ (Rhoads et al. 2003). The surface density of $z \simeq 6$ galaxies inferred from this result, after the correction of continuum magnitude and co-moving volume difference, is about 1.6 times as high as our prediction. This data point is shown as the intersection of the two long, dotted lines. Note strong Lyα emitters are likely only a small fraction of the entire galaxy population, and therefore the actual discrepancy could be even higher. While the nature of this discrepency is currently not understood, one possibility is that the LALA Survey observed an over-dense region.

of them were unambiguously confirmed to be at $z = 6.541$ and $z = 6.578$. The asymmetric line profile and the well measured continuum discontinuities support the high-z interpretation.

Thus it will be interesting to see how these results agree with our predicted LF. Although strictly speaking the redshifts of these two emitters are outside of the $5.5 \leq z \leq 6.5$ range where our prediction is made, they are above this range only by a tiny amount. Unless the LF has an abrupt change at around $z \simeq 6.5$, which is unlikely, a direct comparison is still meaningful.

Although these authors did not give the photometric properties of all these candidates, they did indicate that only a few candidates are brighter than 24.0 mag (quoted magnitudes are all in the AB system) in the narrow-band. The continuum magnitudes in the z'-band were not explicitly given, either, but based on the information provided for the two confirmed objects it seems that the continuum magnitudes of these candidates are approaching 26.6 mag. For simplicity we assume the continuum magnitude cut-off is 26.5 mag. At this brightness level, our prediction gives about 539 objects for their effective searching area. The co-moving volume of their redshift range, $6.508 \leq z \leq 6.617$, is about 10% of that corresponding to $5.50 \leq z \leq 6.50$. Therefore, our LF predicts about 54 objects in their survey. If we take $2/9 \simeq 22\%$ as their success rate, 16 out of their 73 candidates should be really at $z \simeq 6.5$. If Lyα emitters comprise 25% of the total population, the inferred total number of objects at this redshift would be 64, which agrees with our prediction to within 20%.

14.4 Comparing with the Latest Search in the GOODS Field

Very recently, Stanway, Bunker and McMahon (2003; hereafter SBM03) published 8 $z \simeq 6$ candidates using the first three epochs of GOODS data on the CDF-S. These data were taken with the ACS/WFC, and covered about 150 arcmin^2. These candidates were selected as F775W-band drop-outs, just in the way that similar to what we did with the ACS parallel field (Part III). The VLT/ISAAC JHK_s data that we used in Part IV were also used in their search, in the hope that these near-IR data might provide further information about the nature of the candidates.

Although three epochs of data were used, due to the way the GOODS data were taken it is not a trivial issue to stack the images from different epochs. The entire ~ 150 arcmin^2 area was covered by 14–15 "tiles", and the position angles in between epochs has a difference of about 45^o. To make the situation worse, not a single tile can cover more than half of the area that is covered by one tile in any other epoch. Such a choice was made because of the telescope time scheduling that meant to get the highest efficiency. For these reasons, stacking of images obtained in different epochs seems to be only possible after a large mosaic of all the tiles in a given epoch is made (and the stacking can then be performed on those mosaic-ed images).

The source detection and the candidate search, therefore, were actually carried out on the images obtained in each single epoch. This means that the survey cannot reach the depth that would be achievable if the images had been properly stacked. The images of different epochs were largely used only for the purpose of reducing photometric errors for the *detected* sources. Nevertheless, with one full orbit of exposure in the F850LP-band in each epoch, the survey reached a 8 σ limit of $z'_{AB} = 25.6$ mag. However, each epoch has only half-orbit of exposure (1040 seconds) in the F775W-band; the 3 σ limit of this band is $i'_{AB} = 27.3$ mag. For this reason, the major criterion used to select candidates was set to $(i' - z') > 1.5$ mag[2], which means their search were selecting galaxies in the $5.6 \leq z \leq 6.5$ range. The price paid for extending the search into $z < 6$ range is that the contamination due to E/S0 galaxies at $z \simeq$ 1–1.5, which have $(i' - z') \simeq 1.4$ mag, could be significant because of the photometric error.

To the limit of 25.5–25.6 mag, in the redshift range of $5.5 \leq z \leq 6.5$ our LF predicted about 18 objects in ~ 150 arcmin^2, which is more than a factor of two as high as the number of candidates found in SBM03.

The discrepancy seems to be even larger after looking at the detailed photometric properties of these candidates (Table 1 of SBM03). Half of the candidates have additional VLT/ISAAC JHK_s

[2]As a comparison, the vast majority of the candidates found in our ACS parallel field have this color index larger than 2.0 mag; this could be done because our ACS parallel field reached much a deeper depth in the F775W-band than in the F850LP-band.

photometry, and they all seem to be E/S0 galaxies but not high-z objects. These four objects have very large $(J-K_s)$ color index, while a young, star-forming galaxy (presumably the type of objects that a galaxy at such a high redshift should be) should only have a quite flat SED (in f_ν) all the way into the K_s band and thus should have a color index of only about a few tenth of a magnitude. This has been clearly demonstrated in Part IV of this thesis (also see Yan et al. 2003a). As a matter of fact, the $(J-K)$ vs. $(z'-J)$ color-color diagram of SBM03 (their Figure 4) has also made this point to some extend, although the SED templates that they used to compute the "redshift-tracks" seem to be based on local galaxies (for example, the templates of Coleman et al. 1980) and thus may not be applicable at high redshift[3].

In short, all the four candidates that are within the VLT/ISAAC JHK_s coverage do not seem to be at $z > 5.6$, and only the other four that outside of the JKH_s coverage should be kept in the candidate list. As it turned out, the one that was spectroscopically confirmed to be at $z = 5.8$ is indeed outside of the VLT/ISAAC field[4]. Therefore, the result of SBM03 et al. suggests that our prediction is a factor of 4.5 as high as the actual number observed thus far. As the observations of the GOODS will be finished soon, we will be able to further investigate this problem with more reliable data within the current year (2003).

[3]For example, extending such a template for a $z \simeq 0$ elliptical galaxy to $z \simeq 6$ seems not fully justified.

[4]As an aside, the currently available VLT/ISAAC JHK_s data set does not add a strong additional constraint to search for $z \simeq 6$ galaxies, because the survey depths are not sufficiently deep. As pointed out in Part III, the 50% complete limits of these data are J=24.9, H=24.7 and K_s=25.1 mag in AB system. To the limit of 25.0 mag, our prediction gives 1.8 objects for the entire 50 arcmin^2 area. However, the whole data set, which covers all of the GOODS CDF-S field, will be useful after it is all released.

CHAPTER 15

One Application: What Could be the Source of Reionization at $z \simeq 6$?

The intergalactic ionizing background is an important topic that has been under extensive investigation almost right after it was realized that the observed Universe was in a highly ionized state. The understanding of this subject has been in parallel development to the understanding of the background radiation of the Universe, and is closely related to the study of the Lyman-forest seen in quasar spectra. A full account of this subject is obviously beyond the scope of this thesis. As an application of our predicted LF of galaxies at $z \simeq 6$, one aspect of the problem of ionizing background at this redshift (and hence the reionizing background) is discussed here. The following question is addressed: what are the sources that provided the reionizing photons at $z \simeq 6$?

It seems that there are only two kinds of objects for consideration, namely, quasars and *normal* galaxies. It has been long speculated that quasars alone cannot be responsible for all the reionizing photons because the observational evidences suggest that there are simply not enough number of quasars at high redshift. Fan et al. (2002) quantitatively showed that bright quasars cannot be an important source of reionizing photons. However, since the faint-end slope of the quasar/AGN LF has not yet been well constrained at $z > 4$, there is still room for low luminosity quasars/AGN being significant contributors. On the other hand, it has been discussed on several occasions (e.g., Madau, Haardt & Rees 1999; hereafter MHR99) that faint quasars/AGN also seem to be short in number, as the number of red objects in the HDF-N indicates.

Our predicted LF provides a starting point for investigating the alternative that *normal* galaxies were the major reionizing sources. The idea is to find out if the inferred production rate of photons at $\lambda < 912$Å meets the critical value, $\dot{N}_{ion}$, that is required to completely ionize the H I at $z \simeq 6$.

This is a simplified route, but it should give a general picture of what actually happened.

A recipe of calculating $\dot{N}_{ion}$ has been given in MHR99 (their Eqn. 26):

$$\dot{N}_{ion}(z) = 10^{51.2}\,\frac{C}{30} \times \left(\frac{1+z}{6}\right)^3 \left(\frac{\Omega_b h_{100}^2}{0.02}\right)^2 s^{-1}\ Mpc^{-3}, \tag{15.1}$$

where C is the ionized hydrogen clumping factor. Choosing $\Omega_b h_{100}^2 = 0.02$, $C = 30$ and $z = 6$, one finds $\dot{N}_{ion} = 2.51 \times 10^{51}\, s^{-1}\ Mpc^{-3}$.

To calculate the ionizing photon production rate of a galaxy, the shape of the SED of this galaxy is needed. To first order, a simple power law can be used for the $\lambda \leq 912$Å regime: $I(\nu) \propto \nu^{-\alpha}$, where $I(\nu)$ is in unit of $erg \cdot s^{-1} \cdot Hz^{-1}$. Therefore,

$$I(\nu) = I_1 \left(\frac{\nu}{\nu_1}\right)^{-\alpha},$$

where ν_1 is the frequency at $\lambda = 912$Å and $I_1 = I(\nu_1)$. The ionizing photon production rate $\dot{n}_i$ is

$$\begin{aligned} \dot{n}_i &= \int_{\nu_1}^{\infty} \frac{I_1\left(\frac{\nu}{\nu_1}\right)^{-\alpha}}{h\nu}\, d\nu \\ &= \frac{I_1 \nu_1^{\alpha}}{h} \int_{\nu_1}^{\infty} \nu^{-(\alpha+1)}\, d\nu \\ &= \frac{I_1}{h\alpha}, \end{aligned} \tag{15.2}$$

and $\dot{n}_i$ is determined by the flux at 912Å and the slope of the SED in the $\lambda \leq 912$Å regime.

In practice, only the flux at much longer wavelength is directly measurable. Thus I_1 needs to be related to I_0, which is defined at a fiducial wavelength of, say, 1400Å. A power law form is again used to describe the shape of the SED in the range of 912Å$\leq \lambda \leq$ 1400Å : $I(\nu) \propto \nu^{-\beta}$. Assuming a continuum discontinuity of factor of k across the Lyman limit at 912Å, one has

$$kI_1 = I_0 \left(\frac{\nu_1}{\nu_0}\right)^{-\beta},$$

where ν_0 is the frequency at 1400Å. Eqn. (15.2) then becomes

$$\begin{aligned} \dot{n}_i &= (0.65)^{\beta}\, \frac{I_0}{kh\alpha} \\ &= K \cdot I_0, \end{aligned} \tag{15.3}$$

where $K = (0.65)^{\beta}/(kh\alpha)$. The number 0.65 is the ratio ν_1/ν_0.

Now I_0 needs to be related to the observable quantity, f_{0_ν}, which is in the unit of $erg \cdot s^{-1} \cdot cm^{-2} \cdot Hz^{-1}$, by the relation of $I_0 = f_{0_\nu} \cdot 4\pi D_L^2$, where D_L is the luminosity distance from the observer to the object in question. The number $\dot{n}_i$ can be further written as

$$\begin{aligned} \dot{n}_i &= K \cdot 4\pi D_L^2 \cdot f_{0_\nu} \\ &= A \cdot f_{0_\nu}, \end{aligned} \tag{15.4}$$

where $A = K \cdot 4\pi D_L^2$. It is more convenient to use magnitude instead of flux: $f_{0_\nu} = 10^{-0.4(m+48.6)}$, where m is apparent magnitude in the AB system, and the above equation can be written as

$$\begin{aligned} \dot{n}_i &= A \cdot 10^{-19.44} \cdot 10^{-0.4m} \\ &= B \cdot 10^{-0.4m}, \end{aligned} \tag{15.5}$$

where

$$B = 6.886 \times 10^7 \cdot D_L^2 \frac{(0.65)^{\beta}}{k\alpha}. \tag{15.6}$$

The total ionizing photon production rate per unit co-moving volume, $\dot{N}_i$, can be obtained by the following integral:

$$\dot{N}_i = \int_{f_{min}}^{\infty} \dot{n}_i(f)\ \Phi(f) df,$$

where f_{min} is the flux (at 1400Å) of the least luminous object that should be taken into account. Change variable from the flux f to the magnitude m, one gets

$$\dot{N}_i = \int_{-\infty}^{m_{max}} \dot{n}_i(m)\ \Phi(m)\ dm, \tag{15.7}$$

where m_{max} is the magnitude cut-off corresponding to f_{min}, and $\Phi(m)$ is the differential luminosity function in the magnitude domain.

Substituting Eqn. (15.5) into (15.7), and changing apparent magnitudes m and m_{max} into absolute magnitudes M and M_{max}, it follows that

$$\dot{N}_i = B \int_{-\infty}^{M_{max}} 10^{-0.4(M+25+5lgD_L)} \cdot \Phi(M)\ dM, \tag{15.8}$$

where D_L is in Mpc. For the monochromatic flux used in our case [1], $D_L = D\sqrt{1+z}$, where D is the distance measure (or the so-called "transverse co-moving distance"; see, for example, Longair 1998). The calculation of D in an arbitrary cosmology model has been given in many textbooks on cosmology; a very compact summary was given in Hogg (1999).

Once the SED slopes α and β, and the continuum break k are known, the parameter B can be trivially calculated by using Eqn. (15.6). The total ionizing photon production rate $\dot{N}_i$ can be obtained by substituting our predicted LF into Eqn. (15.7).

Eqn. (15.6) is good for arbitrary values of α and β. If the relation between I_1 and I_0 is directly known, the calculation of B can be slightly simplified. Steidel et al. (2000) derived this relation based a composite spectrum that was obtained by combining 29 spectra of Lyman-break galaxies at $z \simeq 3$, and gave I_1=$I_0/4.6$. This is equivalent to taking $(0.65)^\beta/k = 0.217$ in Eqn. (15.6). This value is used hereafter. The index α used in the following analysis was estimated by using a set of model spectra of galaxies with the age of 0.1Gyr (Bruzual & Charlot 1993), and it was found that this SED slope is close to $\alpha \simeq -1.8$.

Two different faint-end slopes were used in the LF, one is -1.6 and the other is -2.0. The latter one was suggested by our result in the ACS parallel field (Chapter 11).

The ionizing photon production rate due to quasars can be calculated similarly. The shape of the SED of a quasar was taken from MHR99:

$$I_\nu(\nu) \propto \begin{cases} \nu^{-0.3} & 2500\text{Å} < \lambda < 4400\text{Å} \\ \nu^{-0.8} & 1050\text{Å} < \lambda < 2500\text{Å} \\ \nu^{-1.8} & \lambda < 1050\text{Å} \end{cases}$$

For the above power law indices, $B = 0.342 \cdot 6.886 \times 10^7 \cdot D_L^2$. Continuity of these three power-law functions is assumed at the listed wavelengths where the slope changes.

The "standard" double power-law quasar LF (e.g., Boyle, Fong & Shanks 1988) was used:

$$\Phi(M) = \frac{\Phi^*}{10^{0.4(\beta_1+1)(M-M^*)} + 10^{0.4(\beta_2+1)(M-M^*)}}.$$

[1] For example, see Weedman (1986), §3.5.

This form has been proved to be a very nice representation for quasars up to at least $z = 2.5$. There are four free parameters involved, namely, the turn-over magnitude M^*, the normalization Φ^*, the bright-end slope β_1, and the faint-end slope β_2. For $z \simeq 6$, the only source of information is from the SDSS results. The Φ^* and β_1 values in a (Ω_M =0.3, Ω_Λ =0.7) universe were taken from Fan et al. (2001): $\Phi^* = 7.2 \times 10^{-8}\,Mpc^{-3}\ mag^{-1}$, and $\beta_1 = -2.58$. Although these fitted values were obtain with $H_0 = 50$, the differences are ignored here. Fan et al. (2001) did not derive the M^* value directly, but for their results to fit reasonably, they found that this value had to be -24.7 mag. Again the slight difference caused by different cosmology models is ignored. The biggest uncertainty is the faint-end slope β_2, which is essentially not known for $z > 4$. Therefore two values were used; one is $\beta_2 = -1.58$ (this is the value obtained at lower redshift) and the other one is $\beta_2 = -2.0$. Based on these parameters, the number density of quasars at $z \simeq 6$ can be calculated. Figure 15.1 compares the predictions for quasars against those for galaxies. At $M_{AB} > -22$ mag, galaxies outnumber quasars by at least two order of magnitude [2].

Thus it is not surprising that *normal* galaxies are more important sources that provided the reionizing background. This is clearly shown in Figure 15.2. Obvisously, quasars cannot be a major source of reionizing photons, even with a steep faint-end slope of -2.0. On the other hand, *normal* galaxies can be a major contributor to the reionizing background, especially if their LF has a steep faint-end slope of -2.0. Of course, this result has an hidden assumption that the ionizing photons escape the galaxies at a high efficiency — by using the $I_1 = I_0/4.6$ relation of Steidel et al. (2000), we implicitly assumed the high (normalized) escaping fraction of 65% (unnormalized value is about 15–20%; see Steidel et al. 2000) that they derived. However, this is not a big issue if the faint-end slope is indeed as steep as -2. As long as some fraction of ionizing photons does escape, no matter how small the escaping fraction is, the *normal* galaxy population will eventually be able to provide sufficient photons when approaching to sufficiently faint brightness level (with $\alpha = -1.6$ the

[2] The discovery of a $z = 5.5$ quasar by Stern et al. (2000) at $M_{AB}(1450\text{Å})\sim$–23.0 mag within an area of 70 arcmin^2 seems to be accidental, as our NOAO-4m upper limit, which is also applicable to quasar search at $z \simeq 6$, is much lower than the value that the discovery of Stern et al. (2000) would suggest.

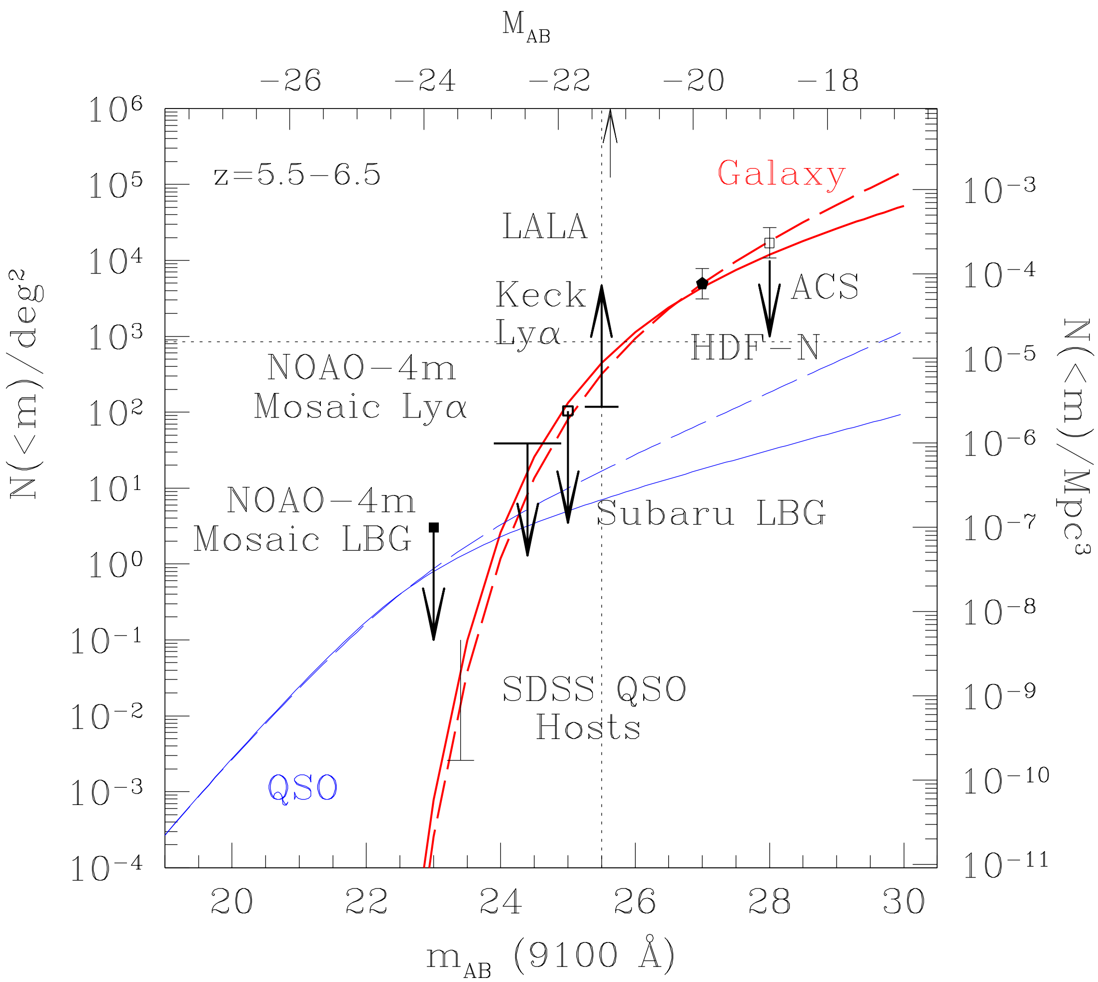

Figure 15.1: The expected number density of quasars at $z \simeq 6$ (blue curves), derived by using a double-power law LF and the normalization based on the SDSS $z \simeq 6$ quasar sample. Two different faint-end slopes are assumed, $\beta_2 = -1.58$ (solid curve) and -2 (dashed curve). The predicted number density of galaxies are superposed (red curves) for comparison. The red solid curve is for a faint-end slope of $\alpha = -1.6$, while the red dashed curve is for a faint-end slope of $\alpha = -2$. The latter is suggested by our ACS parallel field result. At $M_{AB} > -22$ mag, galaxies outnumber quasars by at least two order of magnitude.

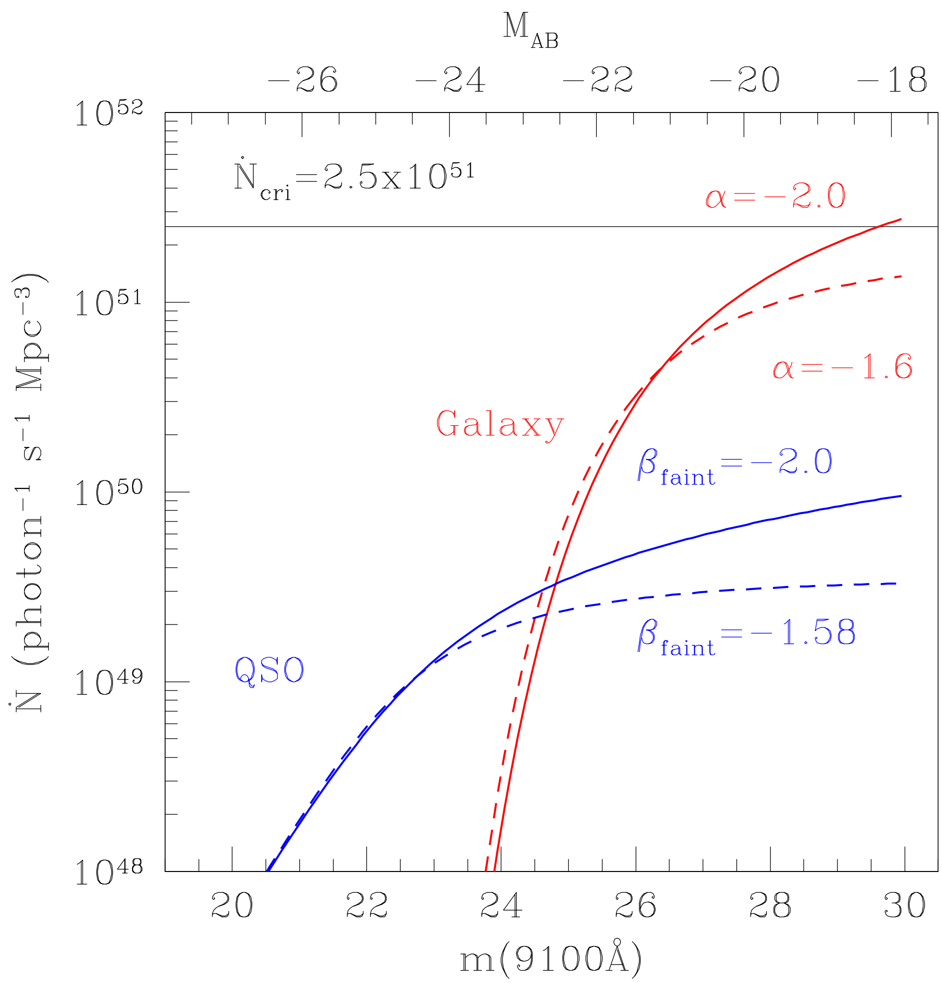

Figure 15.2: The reionizing photon production rates of quasars and *normal* galaxies are plotted in blue and red curves, respectively. They are calculated based on the luminosity functions shown in Figure 15.1. Obviously, quasars are less important reionizing sources. On the other hand, *normal* galaxies could have provided the vast majority of the reionizing photons. If the faint-end slope of the LF of galaxies is indeed as steep as $\alpha = -2$, the less luminous galaxies could provide sufficient photons to keep the Universe ionzied. As most of the star light today comes from the L^* galaxies, this result is a further (indirect) evidence of hierarchical merging.

cumulative contribution from galaxies meets the required critical value at around $M \simeq -12$ mag, the regime of globular clusters today). In other words, it is the dwarf galaxies rather than luminous galaxies that have done most of the reionization at $z \simeq 6$. As most of the star light today comes from galaxies with luminosity close to L^*, this result is a further indication of hierarchical merging.

CHAPTER 16

Future Work

There are a lot of work that can be done in the next few years on the $z \simeq 6$ universe, and they are outlined below.

The part of this thesis that cost the most of the author's time and energy was the intermediate-band NOAO 4m Survey, and yet it seemed to be the least fruitful. However, the by-product of this survey, strong emission-line galaxies in the relatively local universe, could possibly result in some interesting new science. Combined with the Subaru data already at hand, our survey data can result in a complete catalog of such emission-line galaxies within the passbands investigated. A new searching strategy is now being planed.

The idea of using intermediate-band filters to pick up strong Lyα emission lines is still a very promising one; the seemingly fruitless result with current data is just because of the currently insufficient survey depth. If two whole nights of observation at the KPNO 4m can be obtained in one single filter such as the $o(919nm)$, a search that is similar to Kodaira et al. (2003) can be done in conjunction with the Subaru data, and will result in about a dozen genuine Lyα emitters at $z \simeq 6.5$.

The reionization of the Universe likely happened in an inhomogeneous way, given the likely clumpy status of the Universe at that early epoch. Thus investigating different sightlines may provide essential information to this interesting problem. The ACS parallel data are ideal for such an investigation. As the natural extension of what has been done so far, currently a few new parallel fields are under analysis. Together with the GOODS ACS data that will soon be completed, these studies will increase the current sample size by at least one order of magnitude, and result in a significant number of $z \simeq 6$ candidates that are bright enough for spectroscopic follow-up.

Probably the most crucial thing to do is to verify the faint candidates found in the ACS parallel field. Their faint magnitudes are certainly challenging for the spectroscopic capabilities of any existing instrument. However, we do not need to wait for the JWST to do the spectroscopic follow-up to further verify their nature. Deep IR imaging of these candidates with HST/NICMOS should be able to reach a sufficient depth to discriminate both brown dwarf and low redshift E/S0 contaminators from the sample. A HST Cycle 12 proposal aiming at imaging $\sim 40\%$ of the sample has been approved, and the results will soon be obtained. This project will put the most stringent constraint to the faint-end slope of the $z \simeq 6$ LF, and will have a long term impact to a series of important cosmological questions.

Along the same line of research, the HST Ultra-deep Field project that is going to be carried out in Cycle 12 (Fall 2003) will enable us to probe the LF to an extremely faint level that will not be surpass until the launch of the JWST in 2011.

Indeed, this study is likely to be a non-stop quest of looking back in time.

Acknowledgment The author would like to acknowledge the support rom the following STScI grants: AR-8357.01, AR-8768.01 and GO-9174.02. The author also acknowledges funding from NASA JWST Grant NAG5-12460 (to Rogier Windhorst), which supported the reduction and analysis of the NOAO MOSAIC and Subaru data and the subsequent work on the reionizing flux.

REFERENCES

[1] Alexander, D., et al. 2001, AJ, 122, 2156

[2] Alexander, D., et al. 2002, AJ, 123, 1149

[3] Anderson, S. F., et al. 2001, AJ 122, 503

[4] Arnouts, S., et al. 2001, A&Ap, 379, 740

[5] Bahcall, J. N., et al. 1997, ApJ, 479, 642

[6] Barkana, R., & Loeb, A. 2001, Physics Reports, 349, 125

[7] Becker, R. H., et al. 2001, AJ, 122, 2850

[8] Bertin, E. & Arnouts, S. 1996, A&ApS, 117, 393

[9] Boyle, B. J., Fong, R., & Shanks, T. 1988, MNRAS, 231, 897

[10] Boyle, B. J., et al. 2000, MNRAS, 317, 1014

[11] Brandt, W., et al. 2001a, AJ, 122, 1

[12] Brandt, W., et al. 2001b, AJ, 122, 2180

[13] Bruzual, A. G., & Charlot, S. 1993, ApJ, 405, 538

[14] Calzetti, D., Kinney, A. & Storchi-Bergmann, T. 1994, ApJ, 429, 582

[15] Calzetti, D., et al. 2000, ApJ, 533, 682

[16] Capak, P., et al. 2003, submitted to AJ

[17] Cen, R., & McDonald, P. 2002, ApJ, 570, 457

[18] Cen, R. 2002, submitted to ApJ (astro-ph/0210473)

[19] Coleman, G., Wu, C.-C. & Weedman, D. 1980, ApJS, 43, 393

[20] Cowie, L., et al. 2001, ApJ, 551, L9

[21] Dawson, S., et al. 2001, AJ, 122, 598

[22] Dawson, S., et al. 2002, ApJ, 570, 92

[23] Dey, A., et al. 1998, ApJ, 498, L93

[24] Dickinson, M. & Giavalisco, M. 2002, astro-ph/0204213

[25] Djorgovski, S. G. 1985, ApJ, 229, L1

[26] Djorgovski, S. G., et al. 2001, ApJ, 560, L5

[27] Dobbie, P. D., et al. 2002, MNRAS,331, 445

[28] Ellis, R., et al. 2001, ApJ, 560, L119

[29] Fan, X., et al. 1996, AJ, 112, 628

[30] Fan, X., et al. 1999, AJ, 118, 1

[31] Fan, X., et al. 2000a, AJ, 119, 1

[32] Fan, X., et al. 2000b, AJ, 120, 1167

[33] Fan, X., et al. 2001, AJ, 122, 2833

[34] Fan, X., et al. 2002, AJ, 123, 1247

[35] Fernandez-Soto, A., Lanzetta, K. M., & Yahil, A. 1999, ApJ, 513, 34

[36] Fukugita, M., et al. 1996, AJ, 111, 1748

[37] Giacconi, R., et al. 2002, ApJS, 139, 369

[38] Giallongo, E., et al. 1993, ApJ, 416, 137

[39] Giallongo, E., et al. 2002, ApJ, 568, L9

[40] Gnedin, N. Y. 2000, ApJ, 535, 530

[41] Gunn, J. E., & Peterson, B. A. 1965, ApJ, 142, 1633

[42] Franx, M., et al. 1997, ApJ 486 L75

[43] Haiman, Z., & Loeb, A. 1999, ApJ, 521, L9

[44] Haiman, Z. 2002, ApJ, 576, L1

[45] Hasinger, G., et al. 1998, A&Ap, 329, 482

[46] Haywood, M. & Jordi, C. 2002, in EAS Pub. Ser. 2, GAIA: A European Space Project, ed. O. Bienayme & C. Turon, 199.

[47] Hazard, C., et al. 1986, MNRAS, 223, 87

[48] Hogan, C. K., & Rees, M. J. 1979, MNRAS, 188, 791

[49] Hogg, D. W. 1995, astro-ph/9905116

[50] Hu, E. M., & Cowie, L. L. 1987, ApJ, 317, L7

[51] Hu, E. M., et al. 1991, ApJ, 368, 28

[52] Hu, E. M., McMahon, R. G., & Cowie, L. L., 1999, ApJ, 522, L9

[53] Hu, E. M., et al. 2002, ApJ, 568, L75

[54] Hubble, E. P., 1929, ApJ, 69, 103

[55] Humason, M. L., Mayall, N. U., & Sandage, A. R. 1956, AJ, 61, 97

[56] Hurwitz, M., Jelinsky, P., & Dixon, W. 1997, ApJ, 481, L31

[57] Jannuzi, B. T. & Dey, A., 1999, ASP Conference Series, Vol. 191

[58] Kodaira, K., et al. 2003, PASJ (Letters), 55, in press (astro-ph/0301096

[59] Lacy, M., et al. 1994, MNRAS, 271, 504

[60] Longair, M. S. 1998, Galaxy Formation, Springer-Verlag Berlin heidelberg New York

[61] Lanzetta, K. M., Yahil, A., & Fernandez-Soto, A. 1996, Nature, 381, 759

[62] Lanzetta, K. M., et al. 1999, in ASP Conf. Ser. 193, The Hy-Redshift Universe: Galaxy Formation and Evolution at High Redshift, ed. A. J. Bunker & W. J. M. van Breugel (San Francisco: ASP), 544

[63] Leitherer, C., et al. 1995, ApJ, 454, L19

[64] Lilly, S. J. 1988, ApJ, 333, 161

[65] Liu, M. C., et al. 2002, ApJ, 568, L107

[66] Loeb, A., & Barkana, R. 2001, ARAA, 39, 19

[67] Madau, P. 1995, ApJ, 441, 18

[68] Madau, P., Haardt, F., & Rees, M. J. 1999, ApJ, 514, 648

[69] Makino, J. & Hut, P. 1997, ApJ, 481, 83

[70] Manning, C., et al. 2000, ApJ, 537, 65

[71] McLeod, K. K. & Rieke, G. H. 1995, ApJ, 454, L77

[72] Mink, D. 1999, in ASP Conf. Ser. 172, Astronomical Data Analysis Software and Systems VIII, ed. D. Mehringer et al., 498

[73] Minkowski, R. 1960, ApJ, 132, 908

[74] Miralda-Escude, J. 1998, ApJ, 501, 15

[75] Miralda-Escude, J, & Rees, M. J. 1998, ApJ, 497, 21

[76] Nagamine, K., Fukugita, M., Cen, R., & Ostriker, J. 2001, ApJ, 558, 497

[77] Norman, C., et al. 2002, ApJ, 571, 218

[78] Oke, J. B., & Gunn, J. E. 1983, ApJ, 266, 713

[79] Palunas, P., et al. 2000, ApJ, 541, 61

[80] Pascarelle, S. M., Windhorst, R. A., Driver, S. P., Ostrander, E. J., & Keel, W. C. 1996, Nature, 383, 45

[81] Peebles, P. J. E. 1968, ApJ, 153, 891

[82] Pettini, M., et al. 2001, ApJ, 554, 981

[83] Press, W. H., & Schechter, P. 1974, ApJ, 187, 425

[84] Pritchet, C. J. 1994, PASP, 106, 1052

[85] Rhoads, J. E., et al. 2000, ApJ, 545, L85

[86] Rhoads, J. E., & Malhotra, S. 2001, ApJ, 563, L5

[87] Rhoads, J. E., et al. 2003, AJ, 125, 1006

[88] Ricotti, M. 2002, MNRAS, 336, L33

[89] Robinson, J. & Silk, J. 2000, ApJ, 539, 89

[90] Rosati, P., et al. 2002, ApJ, 566, 667

[91] Sandage, A., & Luyten, W. J. 1967, ApJ, 148, 767

[92] Saracco, P., et al. 2001, A&Ap, 375, 1

[93] Sargent, W. L. W., Steidel, C. C., & Boksenberg, A. 1989, ApJS, 69, 703

[94] Schechter, P. 1976, ApJ, 203, 297

[95] Schmidt, M., 1965, ApJ, 141, 1295

[96] Shang, Z., et al. 1998, ApJ, 504, L23

[97] Sharp, R. G., et al. 2001, MNRAS, 326, 45

[98] Songaila, A., et al. 1999, ApJ, 525, L5

[99] Sparks, W. B., et al. 2001, ACS Default (Archival) Pure Parallel Program (ISR01-06)

[100] Spinrad, H. 1982, PASP, 94, 397

[101] Spinrad, H., et al. 1998, AJ, 116, 2617

[102] Stanway, E., Bunker, A. J., & McMahon, R. 2003, Accepted for publication in MNRAS (astro-ph/0302212)

[103] Steidel, C. C., Dickinson, M., & Sargent, W. L. W. 1991, AJ, 101, 1187

[104] Steidel, C. C., & Hamilton, D. 1992, AJ, 104, 941

[105] Steidel, C. C., Pettini, M., & Hamilton, D. 1995, AJ, 110, 2519

[106] Steidel, C. C., et al. 1996a, ApJ, 462, L17

[107] Steidel, C. C., et al. 1996b, AJ, 112, 352

[108] Steidel, C. C., et al. 1999, ApJ, 519, 1

[109] Steidel, C. C., Pettini, M., & Adelberger, K. L. 2000, ApJ, 546, 665

[110] Stern, D., et al. 2000, ApJ 533, L75

[111] Stern, D., & Spinrad, H. 1999, PASP, 111, 1475

[112] Takeuchi,, T. T., Yoshikawa, K., & Ishii, T. T. 2000, ApJS, 129, 1

[113] Thompson, R. I., Storrie-Lombardi, L. J., Weymann, R. J., Rieke, M. J., Schneider, G., Stobie, E., Lytle, D. 1999 AJ, 117, 17

[114] Valdes, F. G. 1998, in ASP Conf. Ser. 145, Astronomical Data Analysis Software and Systems VII, ed. R. Albrecht, R. N. Hook & H. A. Bushouse, 53

[115] Valdes, F. G., & Tody, D. 1998, Proc. SPIE, 3355, 497

[116] van Breugel, W., et al. 1999, ApJ, 518, L61

[117] Vanden Berk, D., et al. 2002, ApJ, 122, 549

[118] Waddington, I., Windhorst, R. A., Cohen, S. H., Partridge, R. B., Spinrad, H., & Stern, D. 1999, ApJ, 526, L77

[119] Weedman, D. W. 1986, Quasar Astronomy, Cambridge University Press

[120] Weinberg, D. H., Hernquist, L., & Katz, N. 2002, ApJ, 571, 15

[121] Weinberg, D. H. et al. 1999, in ASP Conf. Ser. 191, Photometric Redshifts and the Detection of High Redshift Galaxies, ed. R. Weymann et al. (San Francisco: ASP), 341

[122] Weymann, R. J., et al. 1998, ApJ, 505, L95

[123] Yan, H., et al. 2000, PASP, 112, 691

[124] Yan, H., Windhorst, R. A., Odewahn, S. C., Cohen, S. H., Röttgering, H. J. A., & Keel, W. C. 2002, ApJ, 580, 725

[125] Yan, H., Windhorst, R. A., Röttgering, H. J. A., Cohen, S. H., Odewahn, S. C., Chapman, S. C., & Keel, W. C. 2003a, ApJ, 585, 67

[126] Yan, H., Windhorst, R. A., & Cohen, S. H. 2003b, ApJ, 585, L93

[127] York, D. G., et al. 2000, AJ, 120, 1579

[128] Zheng, W., et al. 2000, AJ 120, 1607

[129] Zheng, Z., et al. 1999, AJ, 117, 2757